# Exploring Meteorological and Biomass Burning Aerosol Influences on Marine Stratocumulus in the Southeast Atlantic using WRF-Chem

Eowyn Baughman

A thesis submitted in partial fulfillment of the
requirements for the degree of

Master of Science

University of Washington

2014

Committee:

Rob Wood, Chair

Lyatt Jaegle

Dargan Frierson

Abigail Swann

Program Authorized to Offer Degree:
Atmospheric Sciences

University of Washington

## Abstract

### Exploring Meteorological and Biomass Burning Aerosol Influences on Marine Stratocumulus in the Southeast Atlantic using WRF-Chem

Eowyn Baughman

Chair of the Supervisory Committee:
Dr. Rob Wood
Department of Atmospheric Sciences

Biomass burning in southern Africa exists in a complex series of relationships with its adjacent and remote environments. Gas and aerosol emissions can be lofted into the free troposphere and undergo long-range transport in the prevailing easterlies. The same large-scale subsidence that drives continental fires during the dry season also promotes extensive stratocumulus clouds in the subtropical southeast Atlantic Ocean. Biomass burning aerosols often exist as layers lofted above stratocumulus; where clouds and aerosol layers intersect, the aerosols can influence cloud microphysics and radiative properties. Meteorological patterns also modulate aerosol transport and clouds, but there is ongoing debate in the literature regarding whether this ultimately makes a difference or if aerosol effects are dominant. Few efforts have been made to model this system. In this research, the regional weather-chemistry model WRF-Chem is used to simulate the interaction of biomass burning aerosols with stratocumulus clouds in the Southeast Atlantic to explore how clouds respond to aerosols and to synoptic-scale meteorological variability. At present, absorbing aerosols are excluded; their role will be explored separately in future research. Comparing simulations with biomass burning present or absent, we found increased liquid water path (LWP), reduced lower tropospheric stability(LTS), reduced low cloud, and reduced effective cloud droplet radius. Comparing strong with weak offshore flow indicative of synoptic-scale meteorological variability, we found similarly strong but opposite sign response in LWP, LTS, and low cloud amount. Intriguingly, the offshore flow pattern was associated with greater distance between aerosol and cloud layers, reducing the incidence of cloud-aerosol interactions during peak aerosol loading. We conclude that the meteorological variability driving both clouds and aerosols is an important element in this system that adds interesting complications to the interpretation of observational datasets.

# TABLE OF CONTENTS

# LIST OF FIGURES

# ACKNOWLEDGMENTS

I wish to convey my sincere gratitude to my committee chair, Prof. Robert Wood, who has supported my research since I joined the Dept of Atmospheric Sciences in Fall 2011. I am thankful for his continual guidance and persistent help as this project evolved. He has devoted countless hours to mentorship, encouragement, feedback, editing, conference planning, WRF-Chem travails, and more. Without his help and support, this thesis would not have been possible.

I would like to thank my committee members, Prof. Lyatt Jaegle, Prof. Dargan Frierson, and Prof. Abigail Swan, each of whom offered valuable guidance and constructive commentary. I am thankful that they demonstrated via their own scholarship the ways and means of the scientific endeavor.

I am grateful for the support my peers and colleagues have provided. Rhea George in particular was instrumental in launching my modeling efforts. I appreciate the funding support of the National Science Foundation Graduate Research Fellowship Program. Finally, I would like to thank my wonderful spouse, our unruly friends, and our loving families for helping me remember that not all those who wander are lost.

.

# Chapter 1

# INTRODUCTION

## *1.1 The Southeast Atlantic: a region with strong biomass burning aerosol-cloud interactions*

Open burning of grasses and woodlands represents the largest source of biomass burning emissions globally, two-thirds of which originate from the African continent ([11], Figure 1.1). Biomass burning from Africa constitutes the single largest geographical source of biomass burning emissions. Emissions exhibit strong seasonality with a peak in emissions occurring during the winter dry season: fires in sub-Equatorial Africa typically begin in June and increase to a July maximum before declining in November ([11]). This seasonality follows the pronounced rainy and dry seasons in sub-Saharan Africa ([99]), as the austral spring rains progress southward from the equator ([93]). Figure 1.2 from Wiedinmyer et al ([106]) gives an illustration of the spatial progression of fires in the FINN inventory for 2008.

The savanna fires located between 10 °S and 25 °S are particularly interesting due to their ability to export large quantities of aerosols over the Southeast Atlantic Ocean. The same large-scale subsidence that promotes conflagrations on land during also supports expansive semi-permanent stratocumulus decks off the Namibian and Angolan coasts. The stratocumulus coverage in this region is maximal in the September through November season, broadly coinciding with a seasonal maximum lower tropospheric stability in September ([56]). The permanent subtropical stratocumulus cloud deck in the Southeast Atlantic is one of only three worldwide (fig. 1.4,[111]). Another is located off the western coast of South America, where the VOCALS field campaign collected intensive data 2008. Only the South American continent rivals

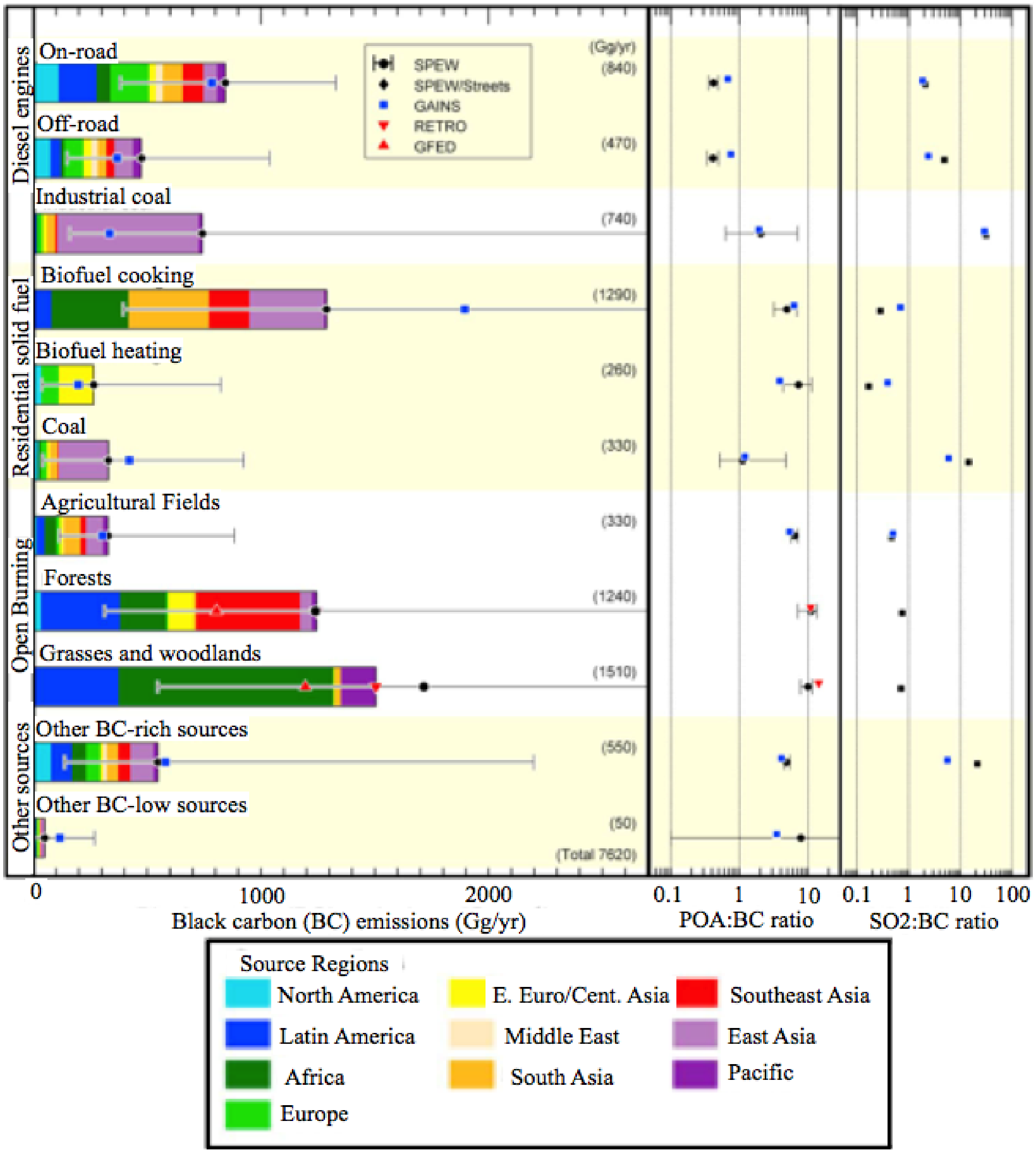

Figure 1.1: Emission rates of black carbon in the year 2000 by source category and ratios of two co-emitted species, primary organic aerosol and SO2.

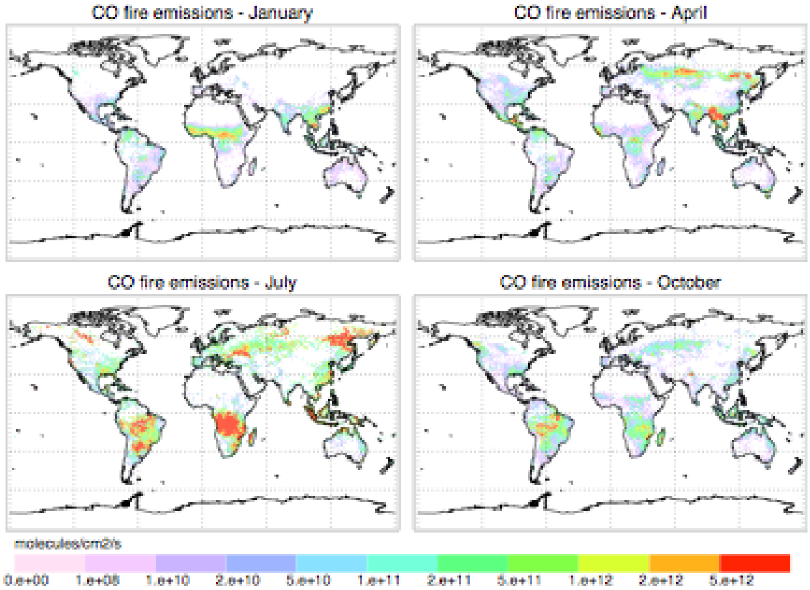

Figure 1.2: Seasonal progression of biomass burning in the NCAR FINN inventory.

sub-Saharan Africa in producing large quantities of biomass emissions near to marine stratocumulus  but there, the Andes Mountains block the efficient export of BB aerosols. There are no such barriers to inhibit plumes of aerosols from transporting BB aerosol off the savanna plateaus towards the stratocumulus clouds over the Southeast Atlantic Ocean. Persistent tropical easterly flow enables long-range transport of biomass burning haze far into the Southeast Atlantic Ocean.

The sheer scale of sub-equatorial African wildfires, easterly offshore aerosol transport and stratocumulus cloud decks in the Southeast Atlantic represent a unique opportunity to study stratocumulus cloud responses to aerosols and large scale meteorology. A multi-agency field campaign, ORACLES (ObseRvations of Aerosols above CLouds and their intEractionS), has been proposed to use a fleet of ships and aircraft to collect a suite of observations to greatly improve the scientific understanding of aerosols, clouds, and radiation in this region. Figure 1.3 from the ORACLES proposal shows cross-sections of aerosol retrievals from the CALIPSO polar orbiting lidar as

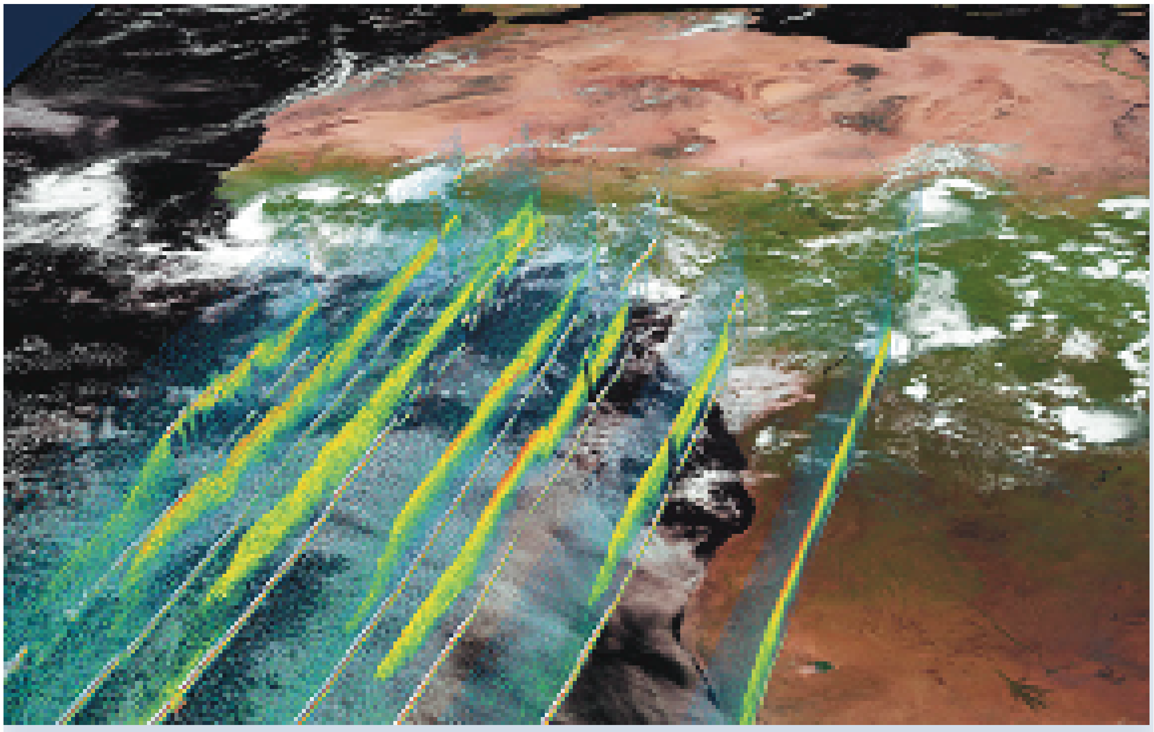

Figure 1.3: Composite of CALIPSO lidar backscatter vertical cross-sections and underlying stratocumulus clouds off the west coast of Africa during the first week of Sept 2008.

these dense aerosol layers migrate offshore over marine stratocumulus during Sept 1-7, 2008. This figure illustrates how the the confluence of biomass burning, synoptic scale circulation, and persistent cloud cover are all important ingredients within this system.

The present study is motivated by the unique confluence of meteorological and aerosol influences on stratocumulus clouds in the Southeast Atlantic. The large scale meteorology that drives biomass burning and aerosol transport also impacts cloud cover and cloud properties, just as it would in the absence of wildfires. If cloud properties are different during an aerosol export event, can we determine the cause? This research seeks to disentangle the confounding influences on clouds. Improved understanding of meteorological and aerosol influences can also inform the collection of

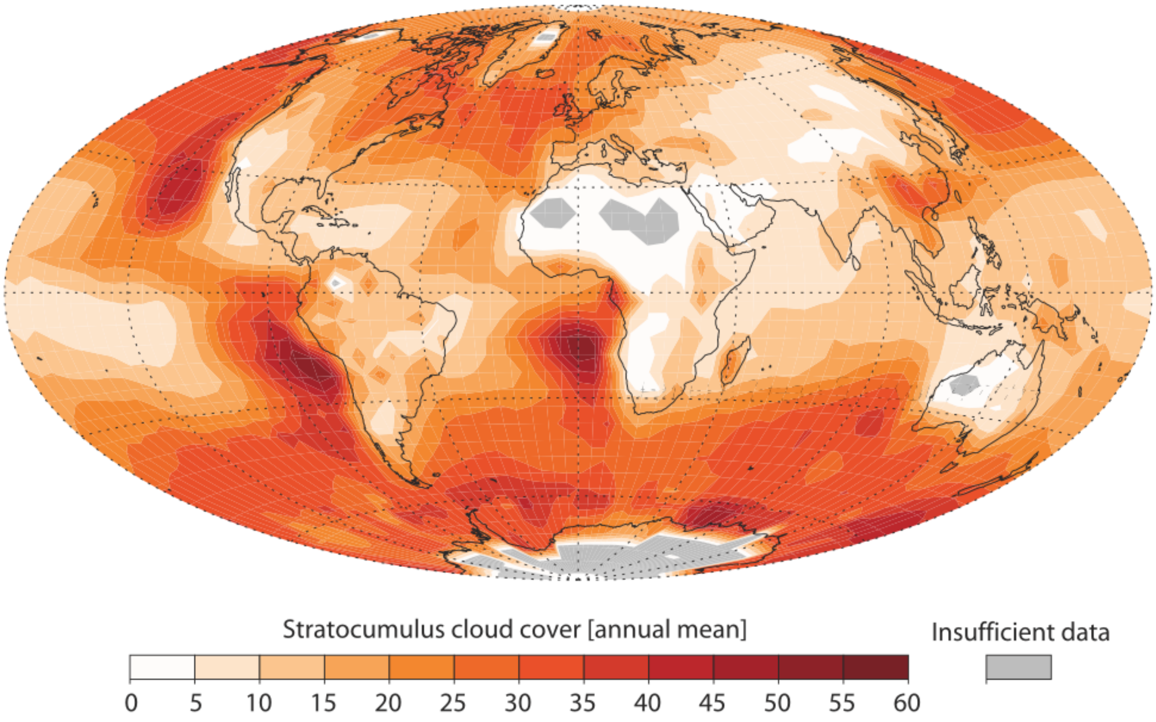

Figure 1.4: Annual mean coverage of stratocumulus clouds, showing the persistent subtropical Sc deck in the SE Atlantic Ocean.

in-situ data during the ORACLES campaign, and preliminary modeling can anticipate data needs.

This chapter will introduce biomass burning aerosols, aerosol radiative and aerosol-cloud interactions, and review the current understanding of cloud responses to aerosols vs meteorology. It will describe the present course of study to advance our understanding of cloud responses in the Southeast Atlantic Ocean.

## *1.2 Biomass burning aerosols*

The open combustion of biomass produces large quantities of both primary and secondary organic aerosol particles that can be transported long distances in the atmosphere. Aerosols from biomass burning consist of a mix of components that both scatter and absorb solar radiation and can impact clouds microphysically and thus are thought to exert significant impacts on regional and global climate ([11]). The combustion of biomass involves multiple stages (ignition, pyrolysis, flaming, smoldering, glowing, extinction), each of which results in different chemical emissions ([8]). Ignition and pyrolysis produce a complex mix of solid and volatile reduced compounds, which are converted during flaming combustion to products such as carbon dioxide, carbon monoxide, methane, nitrogen, water, nitric and nitrous oxides, sulfur dioxide, ethylene, acetylene, various aromatic hydrocarbons, and particulate carbon. Smoldering can generate dozens of additional gaseous volatile and semi-volatile species.

The trace gases in plumes from wildfires quickly undergo chemical aging in the hours after emission. Aircraft observations of Namibian biomass fires during the Southern African Regional Science Initiative 2000 (SAFARI 2000) campaign indicated rapid ozone production via photochemistry, acetone photolysis to produce HO radicals, molar enhancement of volatile organic compounds as they oxidize, and secondary organic aerosols production resulting from these processes ([53]). Dilution and chemical aging in the biomass burning plume continue during long-range transport; by the time plumes reached the ocean during the SAFARI 2000 campaign, Formenti et al ([29]) estimated the sub-micron haze mass was composed of 81% carbonaceous aerosols, 14% secondary inorganic aerosols (such as ammonium, nitrate, and sulfate), and 2% left-over pyrogenic species. Organic and inorganic aerosols primarily scatter shortwave radiation while elemental carbon is the primary light-absorbing species; scattering tends to dominate over absorption in aged plumes such that Formenti et al ([29]) calculated a 550nm mean single scattering albedo of 0.93±0.06. They estimated the mean mass scattering and absorption coefficients to be 4.6±0.6 $\frac{\mathrm{m}^2}{\mathrm{g}}$ and 8±5 $\frac{\mathrm{M}}{\mathrm{m}}$, respectively.

Many of the organic aerosols produced by biomass burning can interact with cloud droplet formation. In order for an aerosol or particle to become involved in cloud microphysical processes, it must be activated and thus become a cloud droplet. The subset of particles that would be activated if subject to a given supersaturation is termed the cloud condensation nuclei (CCN). Activation occurs when the vapor pressure of water in the ambient air is sufficient to form a film of condensate on the particle. Activation occurs more readily on larger droplets with smaller curvature (the Kelvin law) and for hygroscopic solute mixtures (Raoults Law). A particles critical supersaturation denotes the ambient supersaturation at which it will activate. Water-soluble ionic compounds , including sizable fractions of the total calcium, sulfate, and potassium, form the majority of CCN-particles in biomass burning plumes ([29]).

Worldwide, biomass burning generates a significant fraction of total emissions of particulate organics, elemental carbon, carbon monoxide, carbon dioxide, tropospheric ozone, nitric oxide, hydrogen, ammonia, and non-methane hydrocarbons ([8]). Unlike emissions due to industrial activity and energy use, open burning omissions are not tracked or reported by governing agencies. Every day across the globe fires, small and large ignite, smolder, burn, and extinguish. Many are caused by humans or are aided by human influence on land-use, but there is a strong natural component aided by seasonal patterns of temperature, precipitation, drought, and lightning. Global biomass burning emissions are thought to be significantly lower today compared to the 1890s due to fire management and expanded grazing/agriculture ([75]; [79]; [70]). Emissions from biomass burning may increase in the future due to more frequent or more intense burning in regions of increased temperature and or decrease precipitation ([77]; [67]). Emissions from biomass burning depend broadly on region, which determines fire size and intensity, and ecosystem, which determines the fuel characteristics and completeness of combustion. Emissions can be estimated using the equation ([11]):

$$M_{emitted} = \sum BA_i * FL_i * CC_i * EF_i$$

where $BA_i$ is the burned area ($km^2$) $FL_i$ is the fuel load(related to vegetation abundance, kg dry matter per $km^2$), CCi is the combustion completeness fraction (how much of the fuel load is consumed), and $EF_i$ is the emission factor for the chemical species (g of compound emitted per kg dry matter). To calculate total emissions of a species, the summation is taken over i ecosystem classifications.

Satellite measurements are often used to estimate burned area by detecting changes in surface albedo indicative of burned land or by looking for hot-spots in the mid infrared channels ([65]). MODIS/AVHRR uses a hot-spot approach, but retrievals can be complicated by viewing angle, clouds, snow or flooding ([83]; [89]). Perhaps most importantly, the relationship between fire detection and area burnt is highly uncertain, which results in temporally and regionally varying differences between different inventories ([106]). Obtaining more accurate estimates of burned area is the focus of active research, but currently it is the source of potentially large uncertainty. Fuel loads have been estimated from field surveys (eg [88]), satellite classifications of land cover (e.g.[49]), or other land-use/land cover data sets. From the perspective of regional or global modeling, it is challenging to accurately represent the heterogeneity of vegetation types. Field studies are limited in area, while satellite or dynamic vegetation models are limited by resolution.

The extent and manner of combustion (e.g. how much biomass is burned, and whether it smolders or flames) depends on meteorology and ecosystem type. In wooded ecosystems, dry windy conditions are required to ignite most of the fuel load. Grasslands burn more completely when trees are absent. Emissions inventories typically assume relationships to represent these variations, which introduce additional uncertainty.

An emission factor for combustion relates the amount of emissions of a given species that results from burning a given quantity of fuel load. Emission factors are compiled from measurements of the low level airborne smoke samples and some controlled lab measurements. Some species (e.g. carbon monoxide) can be partly constrained using satellite column measurements ([6]). It has been suggested that using aerosol optical properties, may help nudge emission factors, but this approach has not been attempted in any of the widely used data sets ([11]). Emissions estimates from open fires are error-prone, and grassland fires in Africa tend to be under estimated due to their small size ([106]).

## *1.3 Summary of Aerosol Radiative Effects & Aerosol-Cloud Interactions*

Aerosol and cloud processes are large but uncertain terms of the global energy budget. The most recent IPCC report estimates the global aerosol indirect effects ranges from -1.5 to -0.4 $\mathrm{Wm}^{-2}$ ([48], Chp 7). Radiative forcing due to aerosols (roughly, direct and semi-direct effects) are thought to range from -0.95 to +0.05 $\mathrm{Wm}^{-2}$. Model estimates for the Southeast Atlantic suggest direct and semi-direct radiative forcing at top-of-atmosphere are in the range -0.8 to -1.7 $\mathrm{Wm}^{-2}$ ([85]). Global circulation models estimate indirect forcing in the region may lie in the range -1.5 to -3.2 $\mathrm{Wm}^{-2}$ although there is considerable disagreement among models ([45]). The large and uncertain values of aerosol-cloud radiative forcings provides significant motivation to understand the relevant processes.

### *1.3.1 Direct Effect*

The direct radiative forcing (DRF) of an atmospheric aerosol is defined as a perturbation of radiative fluxes is caused by the aerosol. Aerosol particles from biomass burning interact with shortwave radiation, but are too small to have significant effect on longwave radiation ([48], Chp 2). A layer of partially absorbing aerosol will scatter a fraction of incident solar radiation; depending on the phase function, some radiation will escape to space, some will reach the surface, and some will be absorbed elsewhere in the layer (or ambient atmosphere). If the underlying surface has a low albedo (e.g. ocean surface), a partially absorbing aerosol generally exerts a negative radiative forcing because it has a relatively high reflectance and low absorption. If the underlying surface has a high albedo (desert, snow, or clouds), biomass burning aerosols can exert a positive shortwave radiative forcing. The sign of the forcing is dependent primarily on aerosols' absorptivity and the underlying surface albedo ([20]). Moreover the layer can interact with both downwelling and reflected upwelling shortwave radiation, which increases the magnitude of the forcing. In partly-cloudy conditions, clear-sky and cloudy DRFs may offset each other. Using representative estimates of cloud and aerosol optical properties, Chand et al. ([16]) estimated a critical cloud fraction for aged absorbing Southern African BB aerosol, for which the net DRF changes sign from negative to positive, to be 0.4. While absorption is important for direct radiative forcing, in the context of cloud and meteorological responses to aerosols we are primarily concerned with how absorption aloft modifies the thermodynamic profile and possible clouds.

### *1.3.2 Semi-Direct Effect*

The semidirect aerosol effect describes how direct aerosol-radiative interactions affect cloud properties and thereby atmospheric radiation balance by inducing changes in meteorology. Absorbing aerosols induce atmospheric heating and cool the surface below. Aerosols within or adjacent to clouds tend to reduce the relative humidity, causing evaporation and reductions in liquid water and cloud cover. This cloud burnoff is a robust response in models ([44], [2], [47], [57]). Absorbing aerosols located beneath the clouds may enhance convection and cloud cover ([73], [27]) but the enhancement depends on the response of surface fluxes ([27]). Absorbing aerosols above clouds decrease the temperature lapse rate and increase lower tropospheric stability ([57]). In cumulus regimes, enhanced stability tends to suppress low-level convection and thus reduce cloud formation. Over land, surface fluxes of moisture can also decline, depriving nascent clouds of a necessary moisture source ([59]). Aerosols above stratocumulus clouds in subsiding regions present a most interesting and set of cloud responses that remains poorly understood. Marine stratocumuli form in moist boundary layers capped by temperature inversions ([111]). The cool subtropical and tropical eastern oceans are characterized by warm subsiding air above a cooler turbulent boundary layer; stratocumulus is the dominant cloud type in these regions of strong lower-tropospheric stability (LTS, [56]). Absorbing aerosols located above the marine PBL can boost LTS and enhance cloud cover. Reduced entrainment of dry air across a stronger inversion may also increase cloud liquid water path (LWP) ([52]). Diminished cloud top shortwave downwelling by aerosol scattering aloft may decrease cloud-top evaporation (increasing LWP) but could also reduce surface moisture fluxes (decreasing LWP) ([57]). Wilcox ([107],[108]) investigated absorbing aerosol semi-direct effects off the western coast of Africa using aerosol and LWP properties from the Ozone Monitoring Instrument ([46]; [98]) and AMSR-E sensor ([104]; [105]), respectively, and found increasing LWP with aerosol loading, accompanied by thicker clouds. They were unable to determine the precise cause of the LWP response from satellite data. Nor could they control for the influence of meteorological variability, which would complicate a determination of causality.

### *1.3.3 Indirect Effects*

Aerosol indirect effects (AIE) describe the mechanisms by which aerosol particles influence clouds on the microphysical scale. Several AIEs have been observed; their names reflect custom rather than magnitude or prevalence. Each stems from an impact of aerosols on the cloud droplet concentration, but the actual efficiency of aerosol activation is disputed ([60]). This contributes to the uncertainties in quantifying aerosol indirect effects.

#### *1st AIE (Albedo Sensitivity)*

The first aerosol indirect effect (1st AIE, or the Twomey effect) theorizes an increase in cloud albedo (A) with cloud droplet concentration, $\mathrm{N_d}$, assuming that LWP is held constant:

$$\left.\frac{dA}{dN_d}\right| = S = \frac{dA}{d(\tau_c)}\frac{d(\tau_c)}{dN_d}$$

where S is called the albedo susceptibility, $\tau_c$ is the cloud optical depth ([78]).

At a fixed LWP, an increase in CCN should result in smaller droplet radii on average as more numerous nuclei compete for the same moisture:

$${r_v}^3 = \frac{3q_l}{4\pi\rho_v N_d}$$

where $\mathrm{r_v}$ is the volume-averaged cloud droplet radius, $\mathrm{q_l}$ is the liquid water content, and $\rho_v$ is the density of water vapor.

Smaller droplets contribute to larger called optical depth:

$$\tau_c = \int_0^h \frac{3q_l}{2\rho_w r_e}\,\mathrm{d}z = \frac{3}{\rho_w}\frac{LWP}{r_e}$$

where

$$\overline{r_e} = \frac{\int r_e \mathrm{d}z}{\int \mathrm{d}z}$$

where z is the height, $\rho_w$ is the density of liquid water, and $\mathrm{r_e}$ is the cloud droplet effective radius.

Bohren et al ([10]) gives a simplified approximation of cloud albedo calculated by a two-stream radiative transfer model with plane-parallel geometry, isotropic downwelling, and zero surface reflectivity:

$$A \approx \frac{1-g}{2+(1-g)\tau_c}$$

where g is the asymmetry factor (a measure of scattering geometry, $g = 0.85$ for water droplets in visible light).

The first AIE has been estimated from observations, most notably in ship tracks ([80], [78]), that largely confirm the soundness of the hypothesis. However, Ackerman et al ([2]) found that a broadening of the droplet size distribution (rather than a simple shift to smaller sizes) and non-constant LWP can undermine the utility of cloud albedo susceptibility for providing the definitive link between aerosol and cloud albedo.

### *2nd AIE: Precipitation Suppression*

Aerosol-induced precipitation suppression (often termed the Albrect effect) theorizes a decrease in rain rates due to increased CCN concentration. A population of cloud droplets will experience less efficient collision-coalescence when the drops are on average smaller:

A shift in the size distribution towards more numerous but smaller droplets (a response required by the 1st AIE) should, theoretically, reduce the formation of raindrops and hence precipitation. Precipitation suppression can be observed, for example, in ship tracks ([28],[19]). Observations from ship tracks in stratocumulus regions suggest size distributions do favor smaller droplets in the presence of aerosols, but the distribution may broaden or narrow depending on whether the cloud is drizzling ([2]). Data from the VOCALS campaign in the Southeast Pacific are consistent with aerosols suppressing precipitation, particularly in the most weakly-drizzling stratocumulus ([94]).

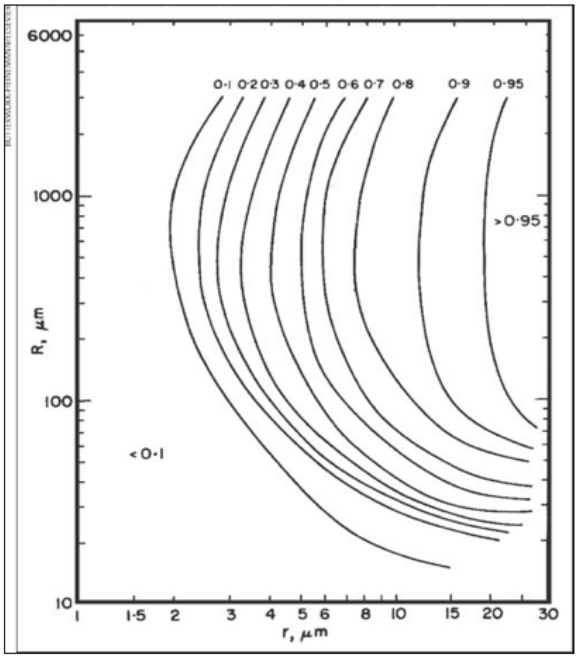

Figure 1.5: Collision-Coalescence Efficiency as a Function of Collector Drop Radius (R) and Collected Droplet Radius (r), microns

The impacts of reduced precipitation on stratocumulli are mixed. Albrecht ([7]) hypothesized that increased cloud lifetime and enhanced liquid water path would result from suppressed precipitation. However, cloud lifetime appears to be only sporadically influenced by aerosols ([51]), and liquid water path responses can be positive or negative, as previously discussed. Consequently, the impact of aerosols on cloud albedo via precipitation suppression is disputed. One recent study shows that large-scale model responses of precipitation to aerosols may be artificially strong ([101]). Additionally, whether LWP increases or decreases with $N_d$ in stratocumulus depends on the rate at which cloud precipitation and droplet sedimentation is affected by aerosols, the subcloud evaporation of precipitation, cloud-top entrainment and the moisture differential across the capping inversion ([3], [110],[14]).

We will be reviewing previous research as it pertains to meteorological-cloud and aerosol-cloud interactions with respect to the Southeast Atlantic and biomass burning aerosols.

## 1.4 Previous Research

Aerosols from Southern Africa have been observed over the Southeast Atlantic since the early 1970s ([93]). The first Southern African Fire-Atmosphere Research Initiative (SAFARI) campaign in 1992 sought to characterize aerosols produced in the region. Based on ECMWF back-trajectory analysis , Swap et al. ([93]) proposed a transport pathway in which biomass burning aerosols, emitted at elevations above sea level and lofted by convection, are transported offshore and subside at a rate of 150 to 400 m per day. Garstang et al ([32]) related Lagrangian in trajectories during the SAFARI-1992 campaign to identify prevailing anticyclonic conditions. Focusing on South Africa, the SAFARI-1992 analysis found only 5% of their calculated trajectories were transported over the Atlantic ([32]). The vast majority recirculated and moved out over the Indian Ocean. The focus of previous field campaigns on southern Africa, whose aerosols primarily export into the Indian Ocean, provides additional motivation to study the easterly transport of aerosols from fires closer to the equator that influence subtropical stratocumulus in the Southeast Atlantic Ocean.

Several studies have used remote sensing data to calculate linear correlations between aerosol loading and cloud properties in the Southeast Atlantic. This formed the basis for arguments that aerosol semi-direct and indirect effects had a dominant effect on cloud cover, liquid water, and droplet size. For example, Breon et al. ([13]) correlated $\mathrm{R_e}$ from AVHRR with aerosol index from POLDER and obtained results consistent with Twomeys aerosol indirect effct. Kaufman et al. ([55]) regressed MODIS cloud cover and $\mathrm{R_e}$, on MODIS aerosol optical thickness, total precipitable water and NCEP meteorology fields (T,u,v,$\omega$,LTS ) and found significant correlations between cloud fraction and meteorological parameters, with a total aerosol loading exerting a strong influence. Wilcox ([107] and [108]) used cloud-aerosol correlations to find that elevated smoke layers warm the atmosphere near 700 hPa by 1 K and this semi-direct effect enhanced cloud LWP by 20 $g/m^2$ relative to clouds under clear skies. Costantino and Breon ([21]) examined the linear dependence of $\mathrm{R_e}$ and other cloud properties on aerosol optical depth when clouds and aerosols were separated or physically mixed. The authors concluded that Twomey and Albrect effects were active in the mixed cases, while cloud fraction was higher in the separated cases. Each of these correlation studies was limited by the natural confounding influences of meteorological variability on aerosol distribution and clouds. Several acknowledged the uncertainty due to meteorology ([55],[108]) or tried to account for it ([21]) but each ultimately attributed most of the causality to aerosol-cloud interactions.

Other studies argued for a larger meteorological influence. Mauger and Norris ([72]) used MODIS cloud and aerosol properties with back trajectories driven by ECMWF meteorology to examine the role of meteorological biases on aerosol-cloud relationships. They focused on the North Atlantic, but their finds called into question the instantaneous correlation approach used previously. They showed that most of the cloud fraction response was explained by the mean LTS 48 hours prior. In fact, the linear dependence of cloud fraction on AOD is 54% weaker when the linear dependence on LTS is removed. Mauger and Norris ([72]) thus argued that meteorology (present and parcel history) are essential and ignoring them grossly overestimates the magnitude of the aerosol indirect effect. George and Wood ([34]) make a similar point that variations in $\mathrm{R_e}$ in the VOCALS region may be $> 50$ explained by meteorological variability. Su et al. ([92]) present a detailed examination of meteorological drivers of aerosol-cloud responses in the Southeast Atlantic. The authors found that cloud fraction, LWP and $\mathrm{R_e}$ depended on the thermodynamic conditions in a way that resembled their dependence on high aerosol loading. They also showed how certain retrieval biases in remotely sensed cloud properties might mimic aerosol indirect effects. These studies suggest that meteorological variability may play a substantial role in determining cloud properties, which may not be apparent from linear correlation methods.

There have been some efforts to model this region. Sakaeda et al. ([85]) used a global atmospheric model (CAM 3.0) coupled to a slab ocean to compute a 20 year simulation of July-October in the Southeast Atlantic. This was the first and only attempt in the literature to perform large scale modeling of this region, but the model was limited by (1) proscribed aerosols and (2) inability to resolve droplet activation, so the research could not consider indirect effects. Sakaeda et al. ([85]) demonstrated the utility of using a model to simulate turning biomass burning off while leaving the meteorological variability intact, an approach we use in the current research to examine the influences of meteorology vs aerosols on stratocumulus in this region.

## *1.5 Present Research*

As described above, previous research on biomass burning aerosols relationship to clouds in the subtropical Southeast Atlantic has explored the contours of uncertainty in this complex system. The present research seeks to quantify some of the same characteristics using a novel approach, while examining hitherto neglected aspects of the system.

The current understanding of lofted aerosols in the Southeast Atlantic is limited by an incomplete characterization of how meteorological conditions influence aerosol-cloud interactions. The net radiative impact of clouds plus aerosols is large; while many influential papers have argued for aerosols of the primary driver of observed cloud variability, studies that attempt to constrain for meteorology find that at least half of the radiative effects implied by correlative studies might actually be meteorologically driven. A primary question of this research asks what the key meteorological controls over clouds and aerosols are, particularly, what role does variability in the large-scale circulation play in driving both cloud variability and aerosol transports/variability. Previous work has focused on controlling for past and present atmospheric conditions, but so far the large-scale patterns influencing both aerosols (transport, distribution) and cloud systems has largely escaped scrutiny. How much of the subseasonal variability in these fields and in correlations between cloud and aerosol fields is driven essentially by weather?

A critical aspect of the meteorological controls relates to the unique vertical distribution of clouds and aerosols over the Southeastern Atlantic. The arrangement of these layers in the troposphere is almost likely to be strongly determined by atmospheric processes independent of aerosol concentration: semi-direct and indirect effects, when they occur, are unlikely to be of a magnitude as large as the weather-related cloud variability. By comparing simulated layer geometry characteristics  height, thickness, separation, number, frequency of occurrence  for model simulations without biomass burning, we can investigate how aerosol layers respond to meteorology. We exclude absorbing aerosols to exclude the influence of ”self-lofting” aerosol layers.

The vertical arrangement of cloud and aerosol layers is also vitally important for determining which aerosol-mediated cloud changes are occurring in the region. Previous studies provide an understanding of what can happen when absorbing aerosols are located above or within a stratocumulus topped boundary layer. The details of these processes are challenging to represent in models, and the magnitude of the net radiative forcing is uncertain. But before we can assess the aerosol effects on clouds, we must understand if and when cloud aerosol layers intersect one another. This determination was impossible to make with passive remote-sensing. With the advent of spaceborne lidar measurements (e.g. CALIPSO, launched in 2006), it became obvious that vertical separations between clouds and aerosols are an important feature in the Southeast Atlantic Ocean. Costantino and Breon ([21]) were the first to use co-located CALIPSO and MODIS observations to segregate samples by vertical separation. They found evidence of indirect aerosol effects when aerosols and clouds intersected. We would like to know how the meteorology influences the likelihood of aerosol-cloud intersection. We would also like to understand how cloud properties may be responding independently to meteorology. These questions can be answered using methods that allow us to minimize aerosol effects while leaving the weather patterns intact.

Regional chemistry-aerosol-climate models, guided and constrained by observations, are appropriate tools to examine the confounding influences of aerosols and meteorology on cloud properties using the layer approach within a synoptic-scale weather pattern framework. Models provide forecasting capabilities and new ways to look at a system. Indeed, to the best of our knowledge the study described in this thesis is one of the first attempts to use regional chemistry-aerosol-cloud modeling to look at aerosol-cloud-weather interactions over the Southeast Atlantic Ocean during Southern Africas biomass burning season.

# Chapter 2

# METHODOLOGY

Building on the work of Sakaeda et al. ([85]), this research uses a modeling approach to examine how biomass burning aerosols impact clouds in the Southeast Atlantic by comparing simulations where biomass burning is either turned ”on” or ”off”. This experimental approach allows us to hold the meteorological parameters to be the same for each simulation such that the the significant differences between them are due to aerosol influences. The simulation without biomass burning also provides a representation of how cloud properties depend on meteorological variability in the absence of wildfires. We are able to determine if these relationships hold for the simulation including fires. Finally, a modeling approach allows us to focus exclusively on indirect aerosol effects. In the future, we can compare indirect and semi-direct aerosol impacts on clouds within the same modeling framework.

The Weather Research and Forecasting (WRF) numerical regional model is coupled to interactive chemistry (WRF-Chem) for the purpose of this research. This model offers the ability of regional scale domains to simulate aerosol transport and synoptic meteorology, while providing better vertical resolution than most global models with fully interactive chemistry-aerosol-clouds. WRF-Chem includes online chemistry with interactions among aerosols, clouds, atmospheric dynamics and thermodynamics that are necessary to investigate the problem. It also features optional routines for biomass burning and aerosol semi-direct radiative effects that can be toggled off separate from other aspects of the code. WRF-Chem has a demonstrated ability to simulate aerosol indirect effects on stratocumulus clouds in the Southeast Pacific ([84],[35], [33]). This section describes the model configuration. We also compare model results to observational fields in an effort to inform later analysis.

## *2.1 WRF-Chem Specifications*

WRF-Chem version 3.4 ([40],[26]) is run over the biomass burning season (July  October) 2007 over the region including sub-Saharan Africa and the Southeast Atlantic Ocean (5 ° N-35 ° S, 20 ° W-40 ° E). A map of the domain is available in Fig. 2.1. The model is run using 1 ° x 1 ° horizontal resolution with 47 vertical terrain-following sigma levels that are more densely packed near the surface (e.g. there are nine levels beneath 2km, 14 beneath 4km). Meteorological boundary conditions are provided at 1 ° x 1 ° horizontal resolution at six hour intervals by ECMWF ERA-Interim reanalysis of winds, pressure, thermal and moisture fields. Chemical boundary conditions are provided every 6 hours for the particular months and years from the Model for OZone and Related Chemical Tracers (MOZART-4, [24]).

### *2.1.1 Physics*

The Advanced Research WRF (ARW) dynamic solver drives the model physics. The dynamical equations are nonhydrostatic, Eulerian and fully compressible. Vertical levels are derived by a terrain-following hydrostatic pressure vertical coordinate. The model uses a third-order Runge-Kutta scheme to integrate forward in time with a three-minute timestep. Longwave radiation is calculated according to the Fu-Liou-Gu schme, new in this version of WRF, which has multiple radiation bands, cloud cover effects, and ozone profiles from climatology. Shortwave radiation is handled by the Goddard scheme, a two-stream multi-band scheme with ozone from climatology and the ability to simulate cloud effects and aerosol-radiation interactions. The Perdue Lin et al. ([66]) microphysics scheme is used: a single-moment bulk scheme with five classes of hydrometeors, including graupel, and the ability to interact with the models chemistry. The Monin-Obukhov surface layer and Noah Land surface ([23]) schemes are utilized. The Grell 3D cumulus paramaterization without shallow convection is

Figure 2.1: Map of the model domain

used to help maintain realistic cloud cover. Planetary boundary layer physics are calculated by the Bretherton and Park ([15]) scheme, an approach based on turbulent kinetic energy closure which is optimized for marine stratocumulus topped boundary layers at coarser spatial resolutions.

### *2.1.2 Chemical Emissions*

Biomass burning is emitted in hot plumes that loft chemical constituents into the troposphere, a process that modifies thermodynamic structure at the source and the efficiency of transport away from the source region. The BEM biomass emissions and plume-rise module ([31], [39]) assimilates remote fire sensing products from MODIS to determine which grid columns have active fires. A land dataset is used to select fire properties, and the parent model supplies the environmental conditions. The height of each plume is derived and used to determine the effective injection height of smoke and gaseous emissions. The plume rise is explicitly simulated using a single dimensional entrainment plume model ([63]) whose governing equations are based on the first law of thermodynamics, the vertical equations of motion, and continuity equation for the water phases ([31]). Inclusion of the plume rise module produces significant improvements simulating wildfires in Alaska ([39]) and aerosol transport in Brazil ([69]).

Wildfire properties were calculated from the Fire INventory from NCAR (FINN) described by Wiedenmyer et al. ([106]). FINN version 1.0 provides daily, 1 km x 1 km, global estimates of area burned, combustion efficiency, land cover, and emissions factors for organic and nonorganic species. Data are available for the years 2002-2013. Fire locations and timing identified from the MODIS thermal anomalies product ([37]). Fire emissions are supplied at hourly intervals throughout the simulations. The relationship between fire presence and area burned is ill-constrained, so a simple assumption is made that each fire is assigned a burned area of 1 $\text{km}^{-}2$ except for savanna/grassland fires which are assigned 0.75 $\text{km}^{-}2$ area burned. Additionally burned area is scaled down if part of the grid square is bare ground. Vegetation density (including bare ground) and land cover designations are determined by the MODIS Vegetation Continuous Fields (VCF) and Land Cover Type (LCT) products, respectively. Emission factors are calculated from published values for LCT classification and vegetation type ([106], Table 1). Uncertainty in these data are thought to represent a factor of two in emissions ([106]).

Anthropogenic emissions of reactive gases and aerosols are taken from Lamarque et al ([62]) for the year 2000 at monthly timescales. This inventory represents a combination of multiple global and regional inventories. Over sub-Saharan Africa: EDGAR-Version 4 is the primary source of methane and ammonia; EDGAR-V4 and RETRO inventories contributed carbon monoxide, nitrous oxides, and non-methane volatile organic compounds; sulfur dioxide emissions came from Smith et al ([90]); organic and black carbon are based on Bond et al. ([12]) and Junker and Liousse ([54]). Emissions from shipping ([25]) and aircraft ([64]) are also included.

Figure 2.2 provides the total emissions for the largest fifteen categories of emissions. BB indicates biomass burning emissions; ANTH indicates anthropogenic emissions. Emissions are often highly localized, especially anthropogenic emissions, so the total is calculated over the whole domain and model simulation period (June - Oct 2007) to facilitate comparison. Carbon monoxide from biomass burning and anthropogenic sources dominate, followed by anthropogenic methane. Anthropogenic and biomass burning sources are comparable in terms of moles emitted; overall input emissions are 52.2% biomass burning and 47.4% anthropogenic in origin. Anthropogenic emissions are mainly confined to population centers while biomass burning emissions occur over vast areas in the continental interior.

### *2.1.3 Chemistry*

Chemical reactions are represented via the Regional Acid Deposition Model version 2 (RADM2, [91],[74]) to resolve quasi-steady state concentrations of 38 predicted, 22

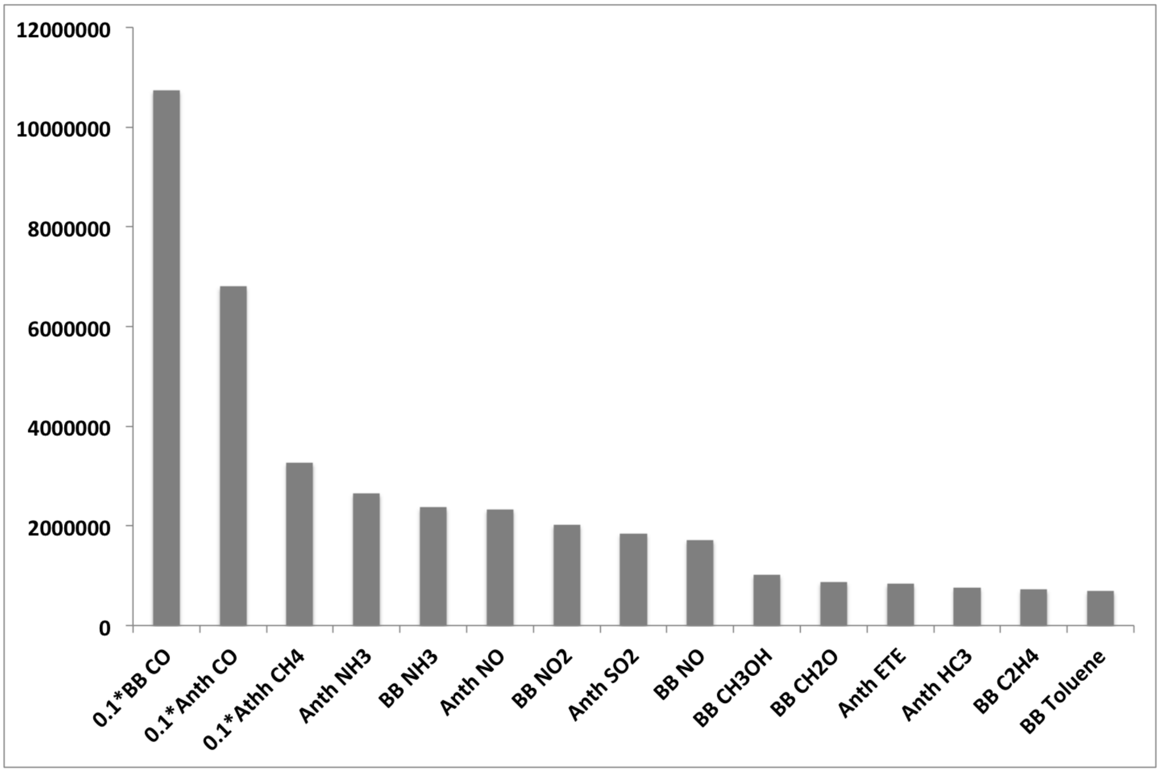

Figure 2.2: Input emissions (moles) of the largest 15 chemical species, total of June - Oct 2007 over the entire domain 34.5S:14.5N, 19.5W:39.5E. BB is biomass burning, ANTH is anthropogenic.

diagnosed, and 3 constant species. This choice of chemical mechanism is one of the only ones that includes aqueous phase chemistry and is also coupled to the microphysical and aerosol modules. The chemical mechanism represents 14 inorganic species, 4 reactive intermediates, 26 stable organic species and 16 peroxy radicals. Species of similar reactivity are treated in bulk. Gas phase and heterogeneous reactions are included. Some aqueous reactions are included and are required for processing sulfur aerosols and their precursors.

In addition to proscribed chemical emissions, the model contains subroutines to estimate additional species online as a function of environmental variables. WRF-Chems online wind-blown dust emissions are excluded from the simulations because it is beyond the scope of this study; dust aerosols should not have a significant impact in our study region ([55]). Biogenic volatile organic compound (VOC) emissions were computed as a function of plant type and environmental conditions based on Guenther et al. ([42],[41]) as functions of temperature and land cover. Sea salt emissions are calculated as a function of 10 m windspeed following the parameterization of Gong et al. ([38]).

### *2.1.4 Aerosols*

The MADE/SORGAM modal aerosol scheme is used ([4],[86]) to define aerosol properties. Three lognormal size modes are considered: Aitken ($\approx 0.1 - 0.1\mu m$), accumulation ($\approx 0.1 - 1\mu m$), and coarse ($> 1\mu m$) modes. For each mode, the mass of each chemical compound and the total number of particles is calculated at each timestep for both cloudy and clear conditions. The aerosol scheme handles gas and heterogeneous chemistry, gas-particle partitioning, coagulation, cloud- and ice-nucleation, dry and wet deposition. Nucleation is calculated following Kulmala et al ([61]), computing homogeneous nucleation in a sulfuric acid water system. The aerosol scheme processes the prognostic chemical species to predict $SO_4$, Na, Cl, $NO_3$, $NH_4$ and several lumped quantities representing primary and secondary organic aerosols.

The MADE/SORGAM module computes the cloud condensation nuclei (CCN, 0.2% supersaturation) diagnostic field. The model uses the Abdul-Razzak ([1]) formulation, but the CCN field is biased low ([112] , [33]). This low bias emerges because WRF-Chem computes the critical supersaturation for a particle with the geometric mean radius of the size distribution by assuming a constant particle radius (for each size mode) rather than deriving this value. A better approach is to calculate the geometric mean radius for each aerosol mode from the total model number and an aggregate of the individual aerosol mass concentrations with particle density of each species already assumed by the code. R. George ([33]) found that this corrected CCN activation improved the agreement of simulated and observed CCN in the VOCALS region of the Southeast Pacific. The same correction was implemented in WRF-Chem for this study, although we lack the observational evidence to test its efficacy in the Southeast Atlantic.

### *2.1.5 Aerosol Effects*

The first and second indirect aerosol effects on warm clouds, as well as the direct and semi-direct effects, are represented through interactions among aerosols, radiation, and cloud properties ([26], [43],[17]). These interactions are set by the choice of physics, chemistry, aerosol and microphysics schemes already described. The first AIE is represented as a direct dependence of the Goddard shortwave radiation scheme on droplet concentration. The Perdue-Lin microphysics code includes prognostic cloud droplet number exchanged with the aerosol processing scheme; cloud droplet in turn influences the autoconversion rate and hence precipitation and other cloud processes (i.e. 2nd AIEs). The direct and semi-direct aerosol effects are implemented in the radiation codes dependence on the bulk optical properties of the aerosol fields. At this time, elemental carbon is excluded from the model to minimize semi-direct effects; later simulations will include elemental carbon.

### *2.1.6 Simulations*

Three main simulations were performed for the period July - October 2007. Absorbing aerosols (and hence, semi-direct effects) are explicitly excluded from the present study with the intention of focusing on cloud microphysical responses to both aerosols and meteorological variability. The simulation BBon has all the aforementioned emissions, processes, and interactions. BBon is designed to mimic the real environment as much as possible, excluding absorbing aerosols, using currently available modules with minor code modifications. A second simulation, BBoff, is identical to BBon except without biomass burning emissions or a plume rise mechanism. Clouds and aerosols are still present in layers and can interact via chemistry and microphysical interactions. In the future, we intend to repeat the simulations with absorbing aerosols (essentially, including semi-direct effects) while using the same chemistry. This will facilitate direct comparisons between model results to quantify the relative impacts of indirect and semi-direct aerosol effects.

## 2.2 Model Evaluation

### *2.2.1 Meteorology*

These figures represent comparisons between ECMWF ERA- Interim reanalysis fields and WRF-Chem output. Since WRF-Chem is forced at the boundaries with ERA-Interim, the degree of agreement can be interpreted as a measure of how well the model simulates the interior of the domain relative to the reanalysis. The models representation of meteorology is its strength.

Figure 2.3 indicates the model captures the 500hPa geopotential height fairly well. The fields are similar in pattern and magnitude, although the model has a slightly stronger height gradient near the southern edge of the domain. The mean WRF-Chem height field also has an elevated contour in the Gulf of Guinea. Examining the standard deviations for model and reanalysis (2.4), the areas of disagreement

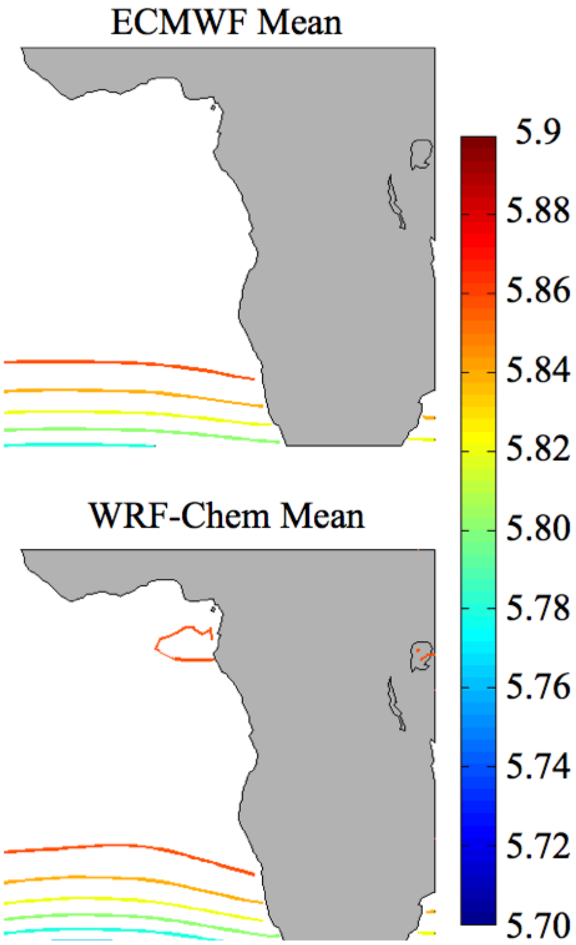

Figure 2.3: Comparison of mean reanalysis geopotential height at 500 hPa (km) with modeled.

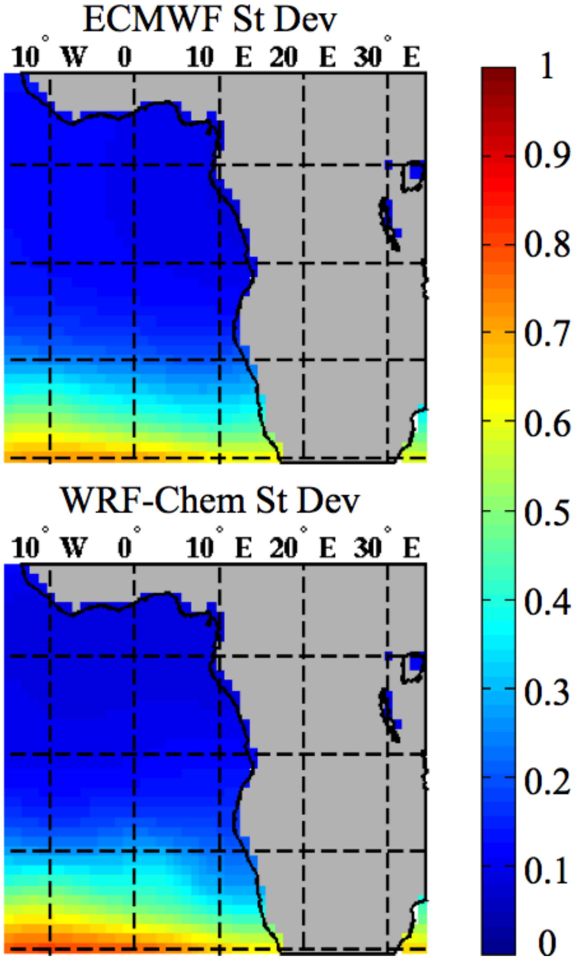

Figure 2.4: Comparison of standard deviation of reanalysis geopotential height at 500 hPa (km) with modeled.

also display more variability in the model, suggesting the influence of short-term fluctuations on the mean state.

At 1000hPa, the agreement in zonal mean wind between the model and reanalysis is very good (2.5). The reanalysis stronger coastal winds extended further off the Angolan coast, likely due to the models trouble producing proper coastal boundary layers. Surface zonal winds in the western oceanic portion of the domain are 1-3 m/s weaker in the model than in the analysis but the overall patterns are consistent. The standard deviations in the 1000hPa zonal winds are similar between the model and reanalysis (2.6).

The model produces 850hPa zonal winds that show good agreement with the reanalysis (2.7). The mean flow at 850hPa the subtropics is easterly. Westerly flow exists in the mid-latitudes, and in Gulf of Guinea where cloud regimes are more cumulus. The difference in this Gulf between the model and reanalysis likely reflects differences in stratocumulus-cumulus transitions. The reanalysis and model capture similar scales of variability (2.8) with the model producing 2-3 more standard deviations of variability in the sub-tropical ocean.

At 700hPa, both the reanalysis and the model produce easterly (westerly) winds equatorwards (polewards) of 15° S, with the reanalysis producing stronger easterlies and a more consistent divide (fig. 2.9). The region of easterly 700hPa flow off the Angolan coast is more pronounced and stronger by several m/s in the reanalysis, which could give a mean transport at this level that is too weak at times in the WRF-Chem model. However, the WRF-Chem model 700hPa zonal flow is more variable throughout much of the domain (fig. 2.10), suggesting a mix of stronger and weaker transport episodes.

The model produces very realistic meridional surface (1000hPa) winds (fig. 2.11). The region is characterized by southerly flow at the oceans surface, which helps advect cooler temperatures northward (e.g. fig. 2.19). A small region of northerly flow in the far south-west corner of the domain is not captured by WRF-Chem, but is not

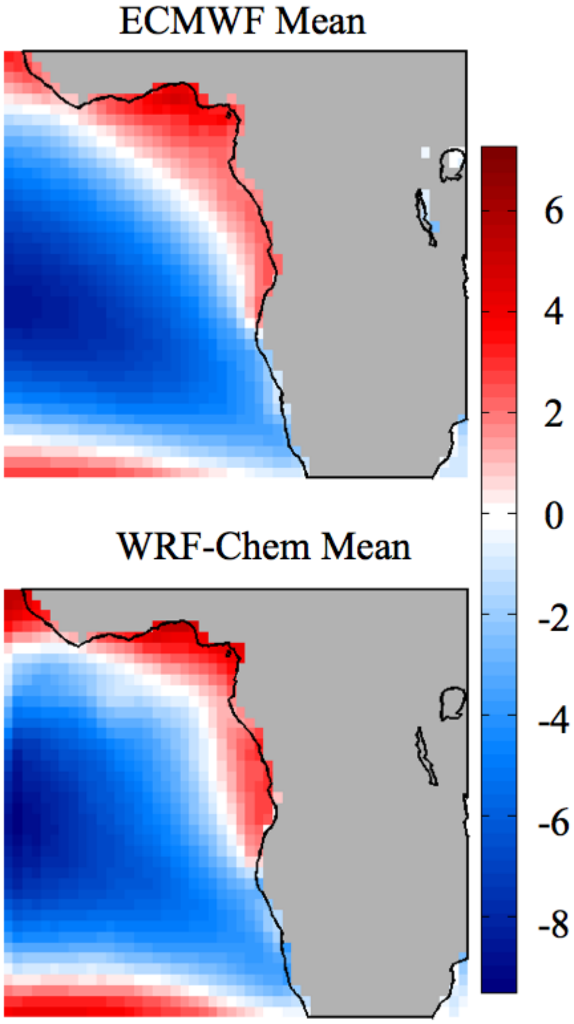

Figure 2.5: Comparison of mean reanalysis zonal wind at 1000 hPa (m/s) with modeled.

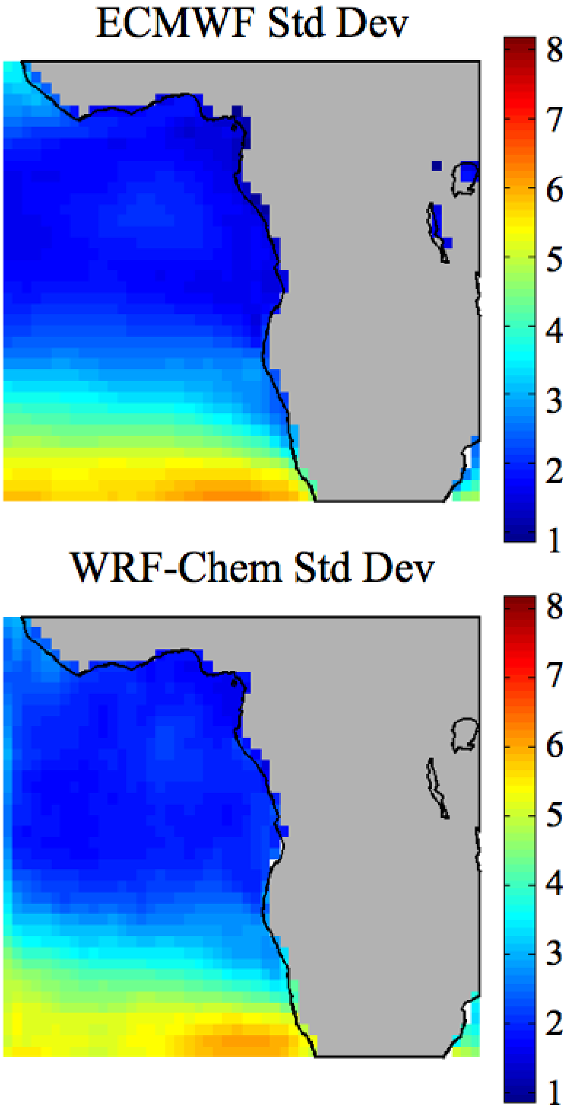

Figure 2.6: Comparison of standard deviation of reanalysis zonal wind at 1000 hPa (m/s) with modeled.

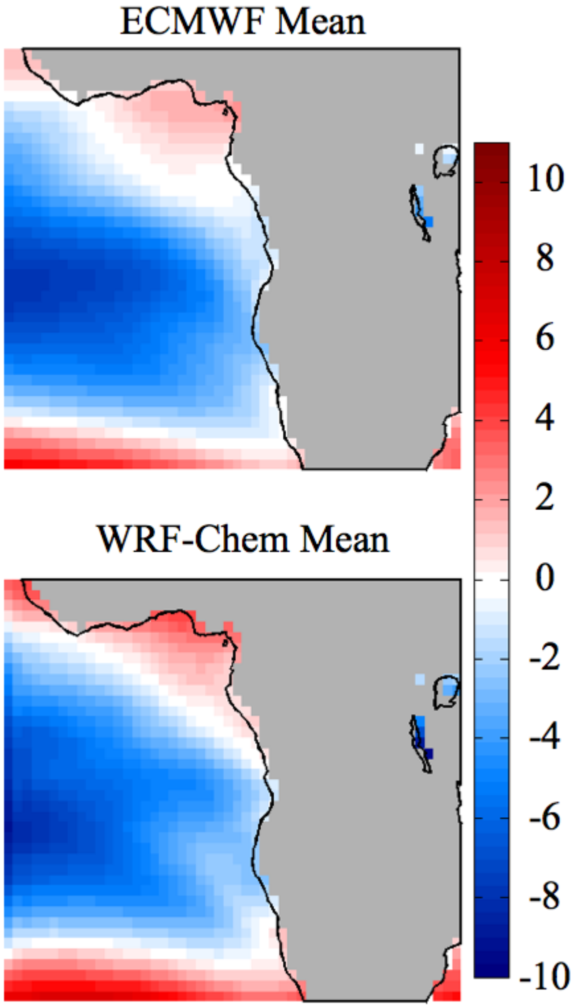

Figure 2.7: Comparison of mean reanalysis zonal wind at 850 hPa (m/s) with modeled.

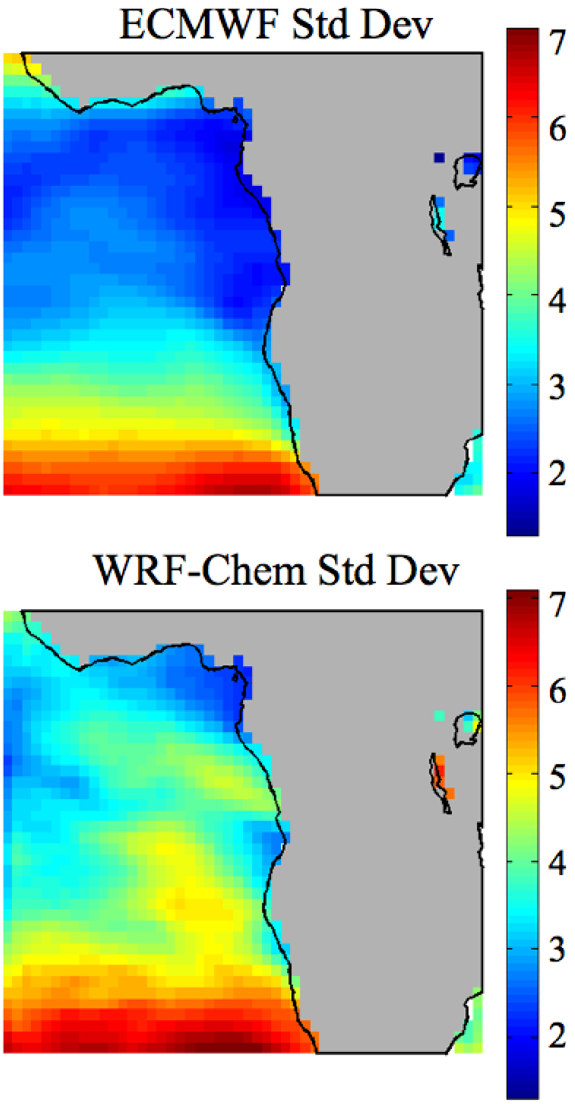
ECMWF Std Dev

WRF-Chem Std Dev

Figure 2.8: Comparison of standard deviation of reanalysis zonal wind at 850 hPa (m/s) with modeled.

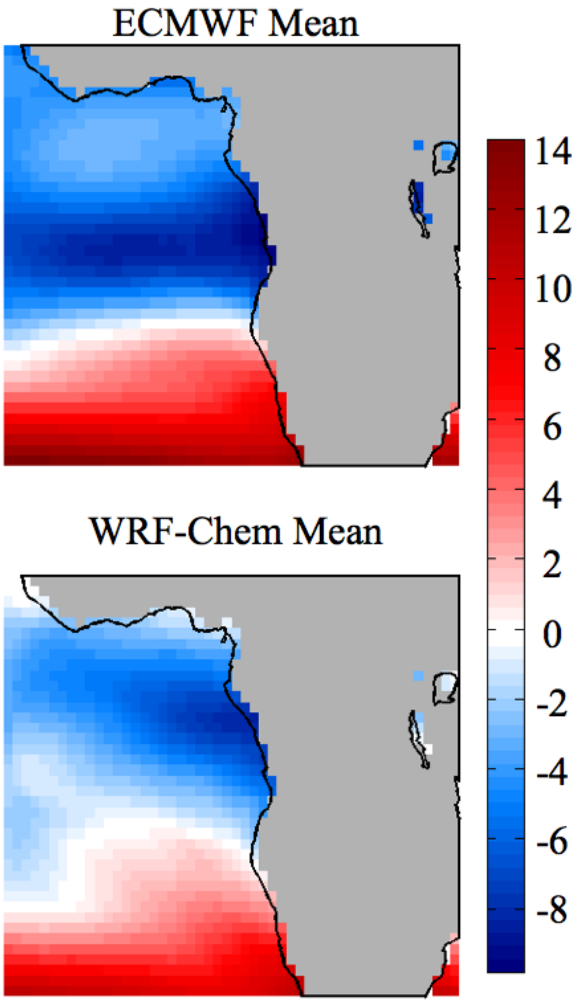

Figure 2.9: Comparison of mean reanalysis zonal wind at 700 hPa (m/s) with modeled.

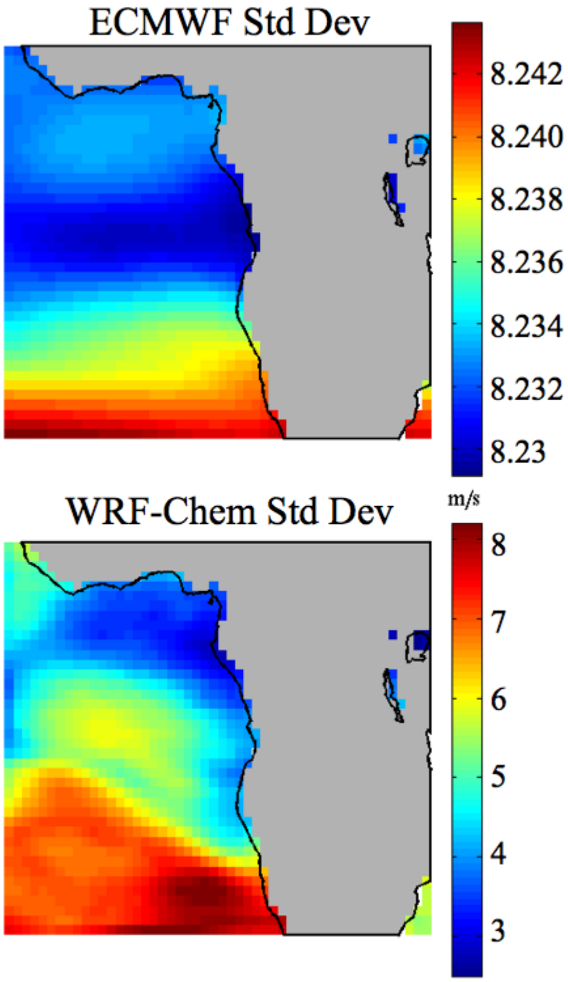

Figure 2.10: Comparison of standard deviation of reanalysis zonal wind at 700 hPa (m/s) with modeled.

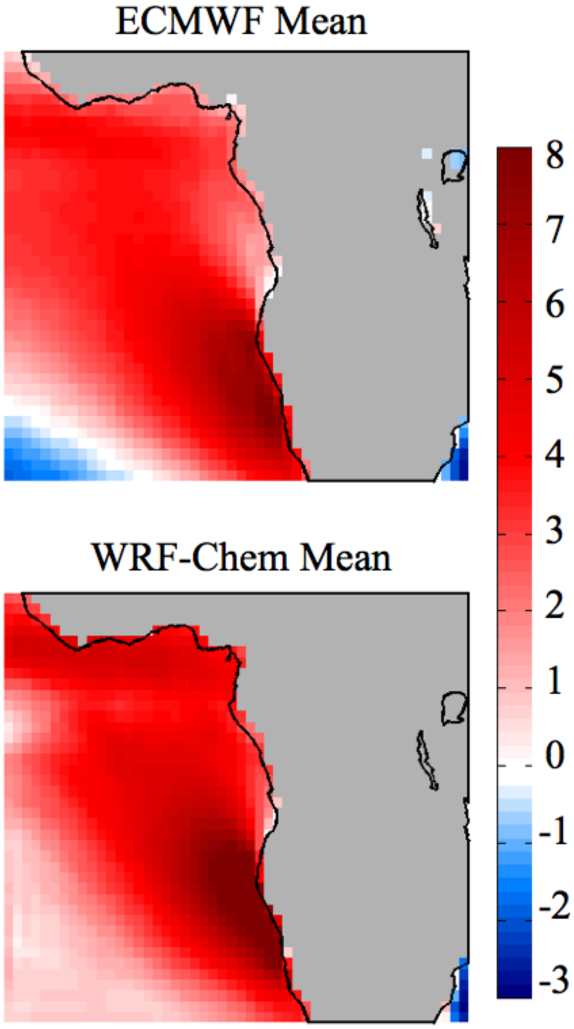

Figure 2.11: Comparison of mean reanalysis meridional wind at 1000 hPa (m/s) with modeled.

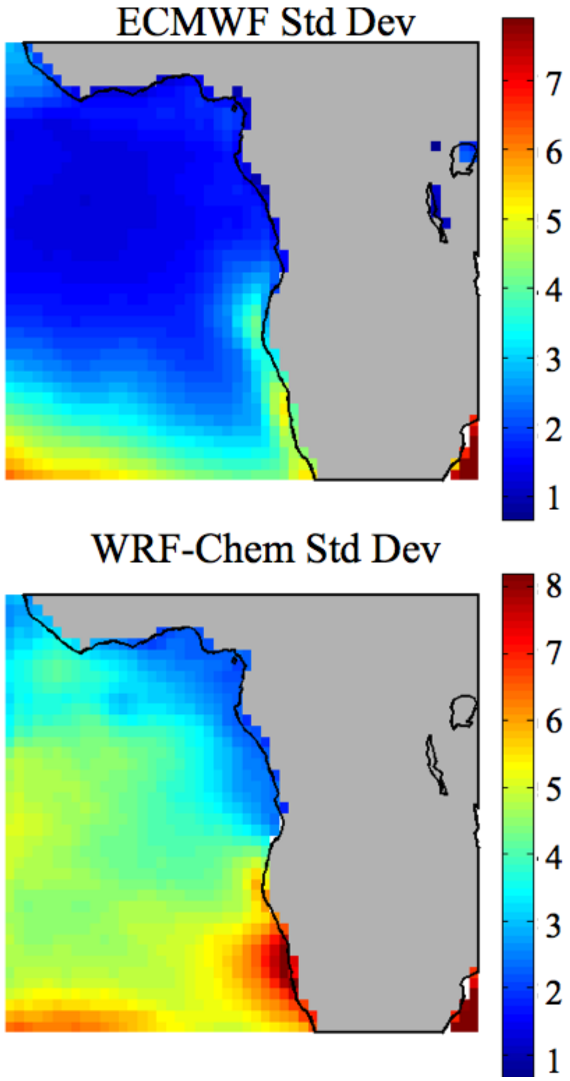

Figure 2.12: Comparison of standard deviation of reanalysis meridional wind at 1000 hPa (m/s) with modeled.

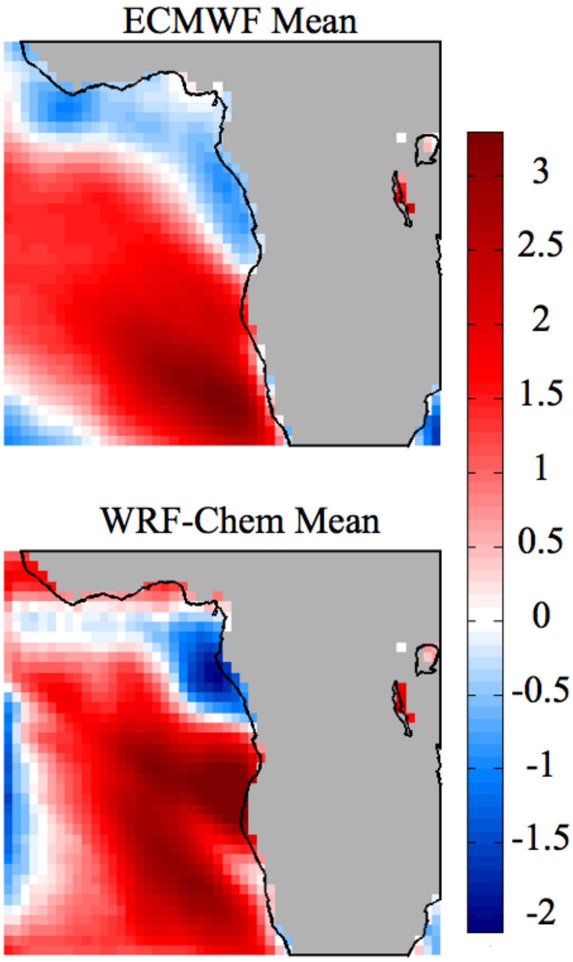

Figure 2.13: Comparison of mean reanalysis meridional wind at 850 hPa (m/s) with modeled.

relevant to this study. The model produces overall more variability in the surface meridional wind field than the reanalysis, particularly in the stratocumulus areas and near the coastline (2.12).

The agreement between model and reanalysis of the meridional winds at 850hPa is less consistent but still fairly good(fig. 2.13). The model and reanalysis produce very similar patterns, but the model has stronger southerly winds near Gabon (at the equator) and stronger coastal northerly winds at 15° S. This may be related to

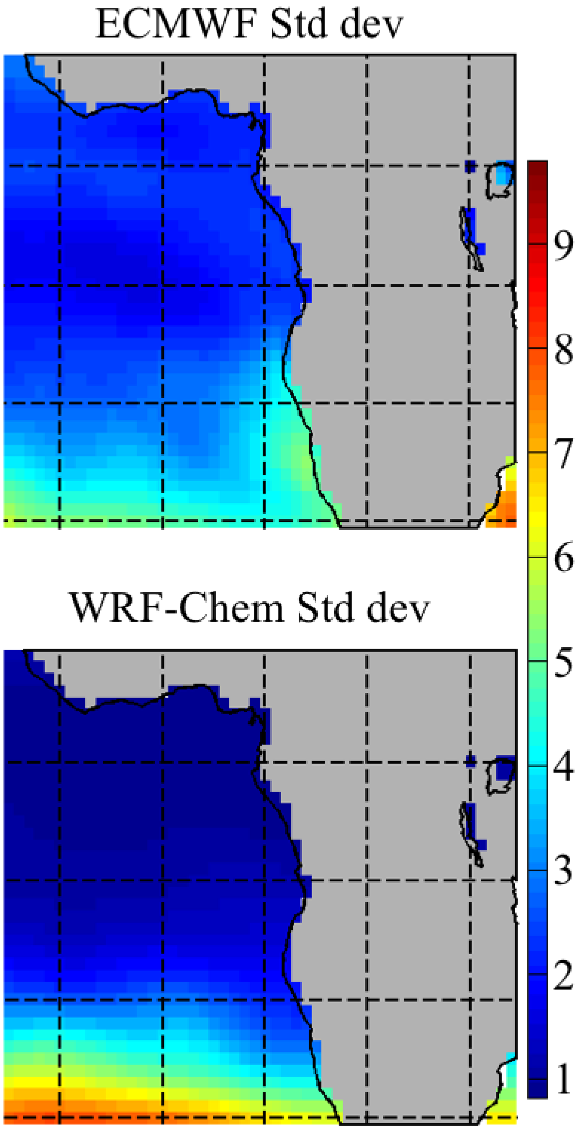

Figure 2.14: Comparison of standard deviation of reanalysis meridional wind at 850 hPa (m/s) with modeled.

boundary layer representations. The model produces more variability in the 850hPa meridional wind over most of the ocean (fig. 2.14).

Above the boundary layer at 700hPa, prevailing meridional winds are weaker and more northerly or neutral in both the reanalysis and the model (fig. 2.15). The model has 1-2 m/s stronger V-winds in some areas, while the reanalysis has a tongue of southerly flow extended further northward in the stratocumulus region. The model has more variability equatorwards of 15° S and less variability polewards of 15° S (fig. 2.16).

The 700hPa mean vertical winds agree reasonably well between the reanalysis and the model (fig. 2.17). Both model and reanalysis show a broad area of gentle subsidence with similar spatial means (excluding coastlines, spatial mean = 0.45 hPa/s for model, 0.46 hPa/s for ERA-Interim). However the model subsidence is a much smoother field, whereas the reanalysis is speckled with rising motion over the ocean and rising motion along most of the continental coastline. These variations in the reanalysis data exist in time as well as space, as seen in Fig. 2.18.

Temperatures near the surface agree fairly well between the model and reanalysis (fig. 2.19). Both fields feature a tongue of cooler water associated with cold air advection; in the model, this feature is narrower and pushed up against the coast. This is consistent with the differences in surface winds. The model produces similar variability as the reanalysis (fig. 2.20).

At 850hPa, the temperature field has a strong gradient tilting northwestward. This feature is represented well in the model (fig 2.21). In the model, the gradient tilts slightly more to the north, and warm air near the coast does not extend as far westward. In both the model and reanalysis, variability in the 850hPa temperature field is centered about the gradient (fig 2.22). These features are likely caused by the 850hPa surface intersecting the planetary boundary layer.

Above the boundary layer at 700hPa, agreement in the temperature fields is very good, although the model is a few degrees warmer over much of the domain (fig 2.23).

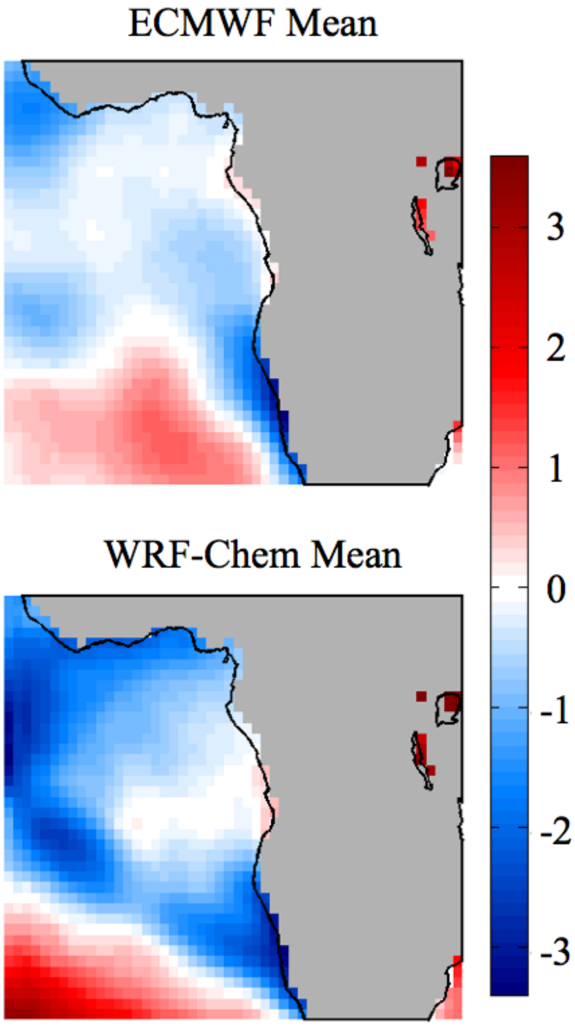

Figure 2.15: Comparison of mean reanalysis meridional wind at 700 hPa (m/s) with modeled.

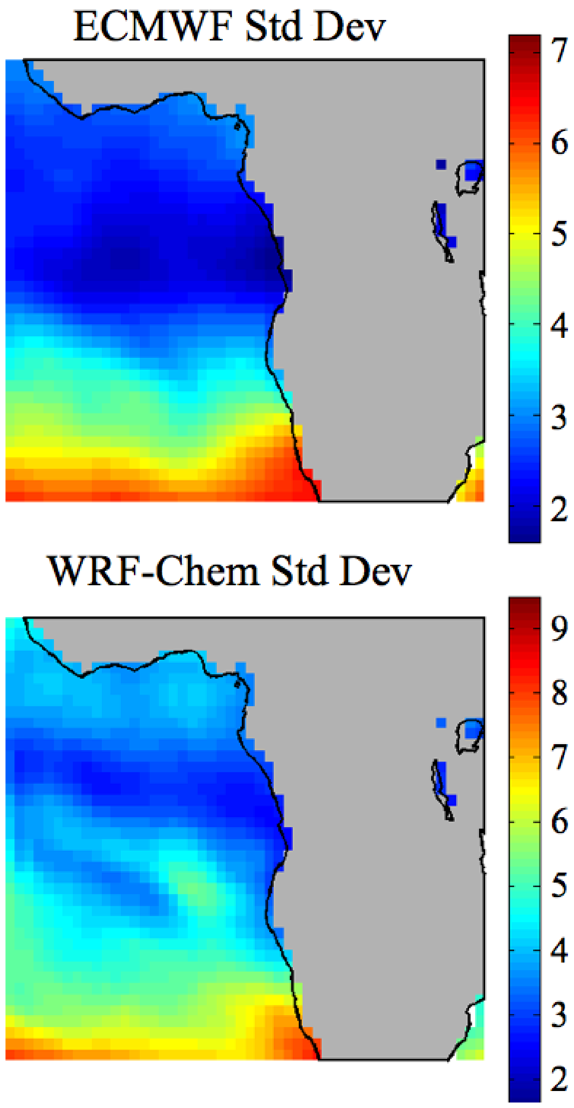

Figure 2.16: Comparison of standard deviation of reanalysis meridional wind at 700 hPa (m/s) with modeled.

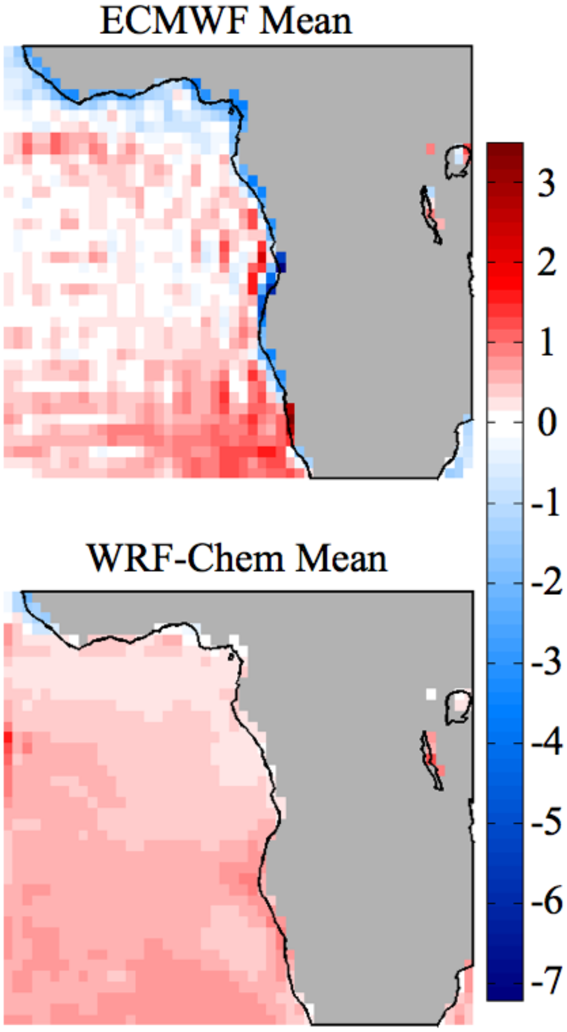

Figure 2.17: Comparison of mean reanalysis vertical wind at 700 hPa (cm/s) with modeled.

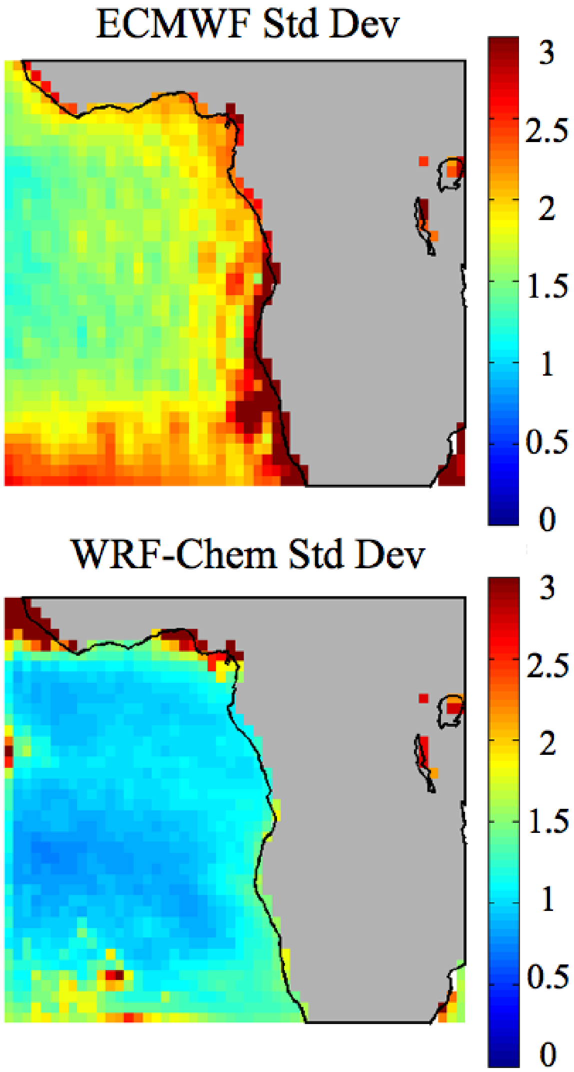

Figure 2.18: Comparison of standard deviation of reanalysis vertical wind at 700 hPa (cm/s) with modeled.

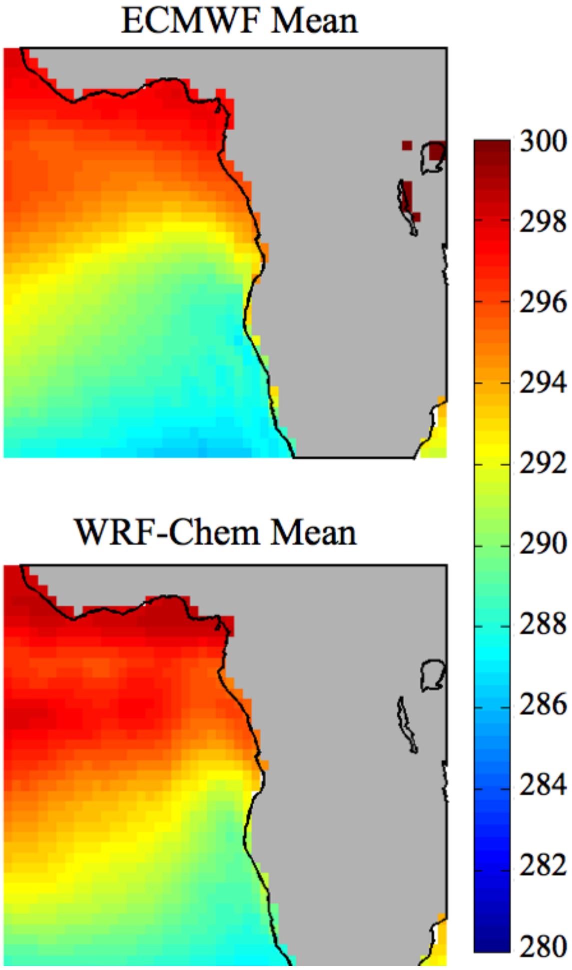

Figure 2.19: Comparison of mean reanalysis air temperature at 1000 hPa (K) with modeled.

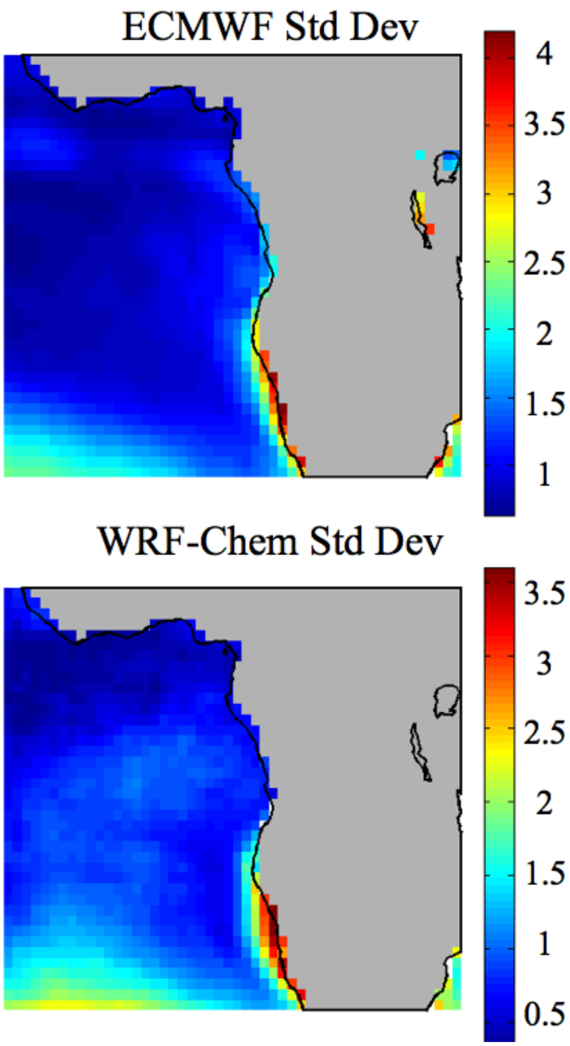

Figure 2.20: Comparison of standard deviation of reanalysis air temperature at 1000 hPa (K) with modeled.

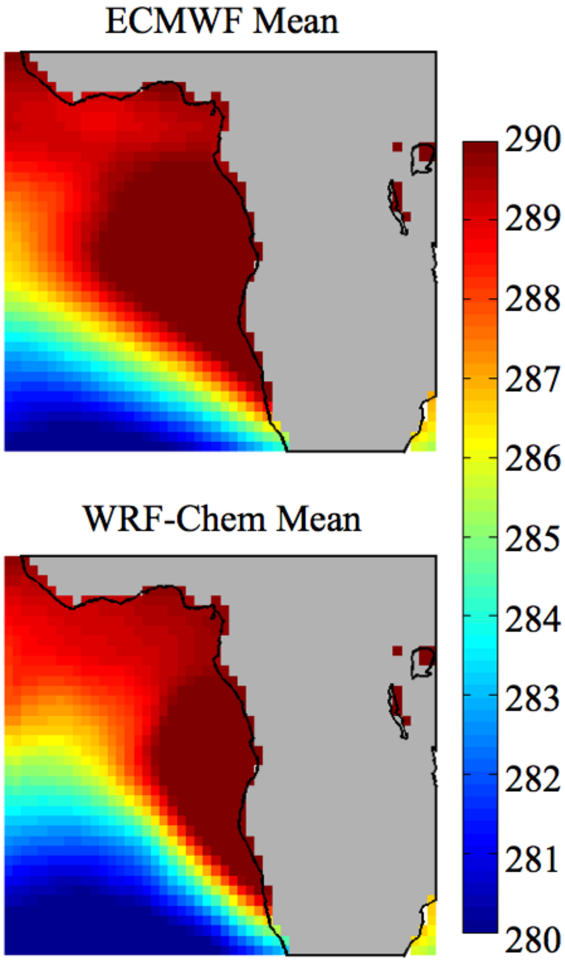

Figure 2.21: Comparison of mean reanalysis air temperature at 850 hPa (K) with modeled.

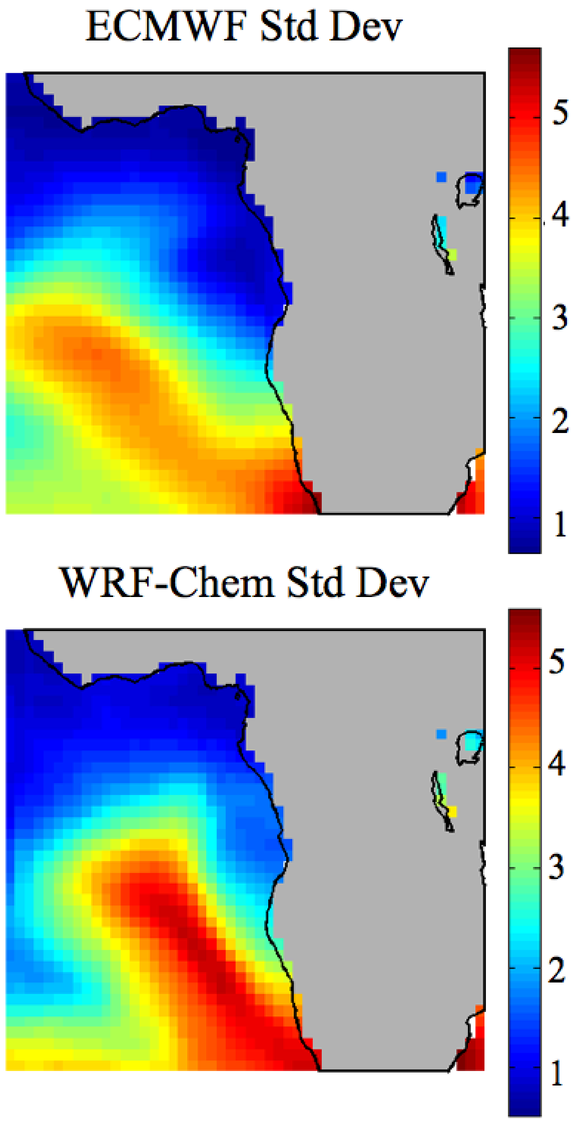
ECMWF Std Dev

WRF-Chem Std Dev

Figure 2.22: Comparison of standard deviation of reanalysis air temperature at 850 hPa (K) with modeled.

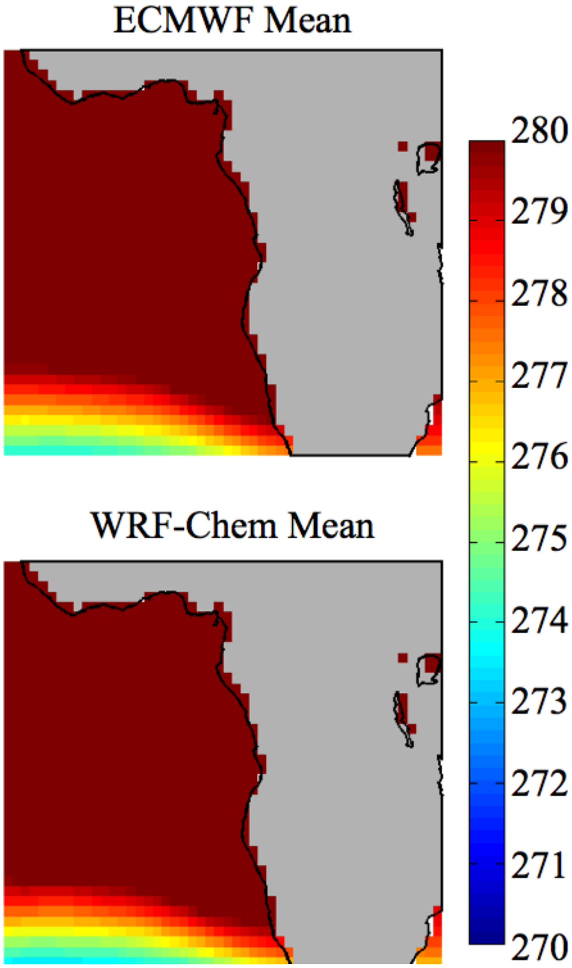

Figure 2.23: Comparison of mean reanalysis air temperature at 700 hPa (K) with modeled.

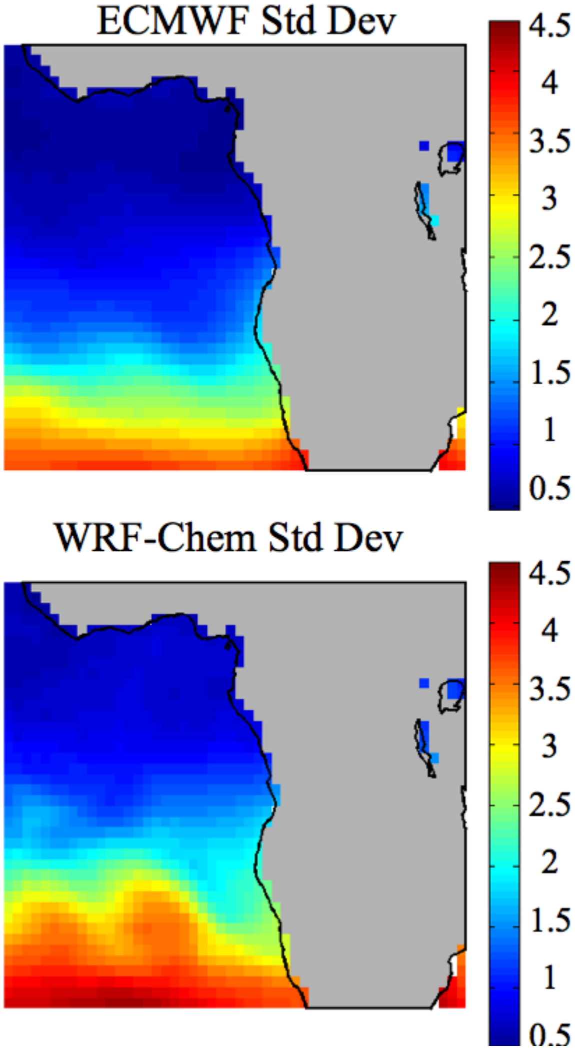

Figure 2.24: Comparison of standard deviation of reanalysis air temperature at 700 hPa (K) with modeled.

Variability is similar as well (fig 2.24).

### *2.2.2 Cloud Properties*

Cloud properties are taken from a number of observational sources. Due to the resolution and lack of sub-grid scale clouds, maintaining a realistic stratocumulus cloud deck was a top priority when designing the model configuration. The model configuration, determined as it was by the need to include aerosol indirect effects and aqueous chemistry, was further refined to maintain realistic cloud properties. For example, shallow convection was turned off to reduce spurious cloud-surface decoupling, and the activation scheme was modified in a way that produced better CCN concentrations in the Southeast Pacific ([33]). The model performs adequately well at capturing the key cloud properties that are essential to this project.

Observed low cloud fraction is derived from CALIPSO retrievals and processed to produce gridded fields (data available from the CALIPSO-GOCCP project). Low clouds are defined as cloudy retrievals beneath 680hPa. WRF-Chem does not actually simulate sub-gridscale cloud fraction, so for these figures the fraction of low clouds at any point is defined as the frequency with which a low cloud appears in that gridbox. The model is able to simulate a spatially broad, temporally persistent population of low clouds that compares well with the CALIPSO observations (fig 2.25). The model exhibits higher variability, which one would expect due to its binary determination of cloud presence.

Cloud liquid water path is calculated as the vertical integral of liquid water content when clouds are present. The value is taken at 1:00pm local time to compare to the AMSR-E Advanced Microwave Scanning Radiometer-EOS (AMSR-E) which makes observations around 1:30pm local time. The model overestimates LWP by approximately 50% in the stratocumulus region of interest (fig 2.26). The model also produces more variability in cloud LWP although without a coherent structure (fig 2.27).

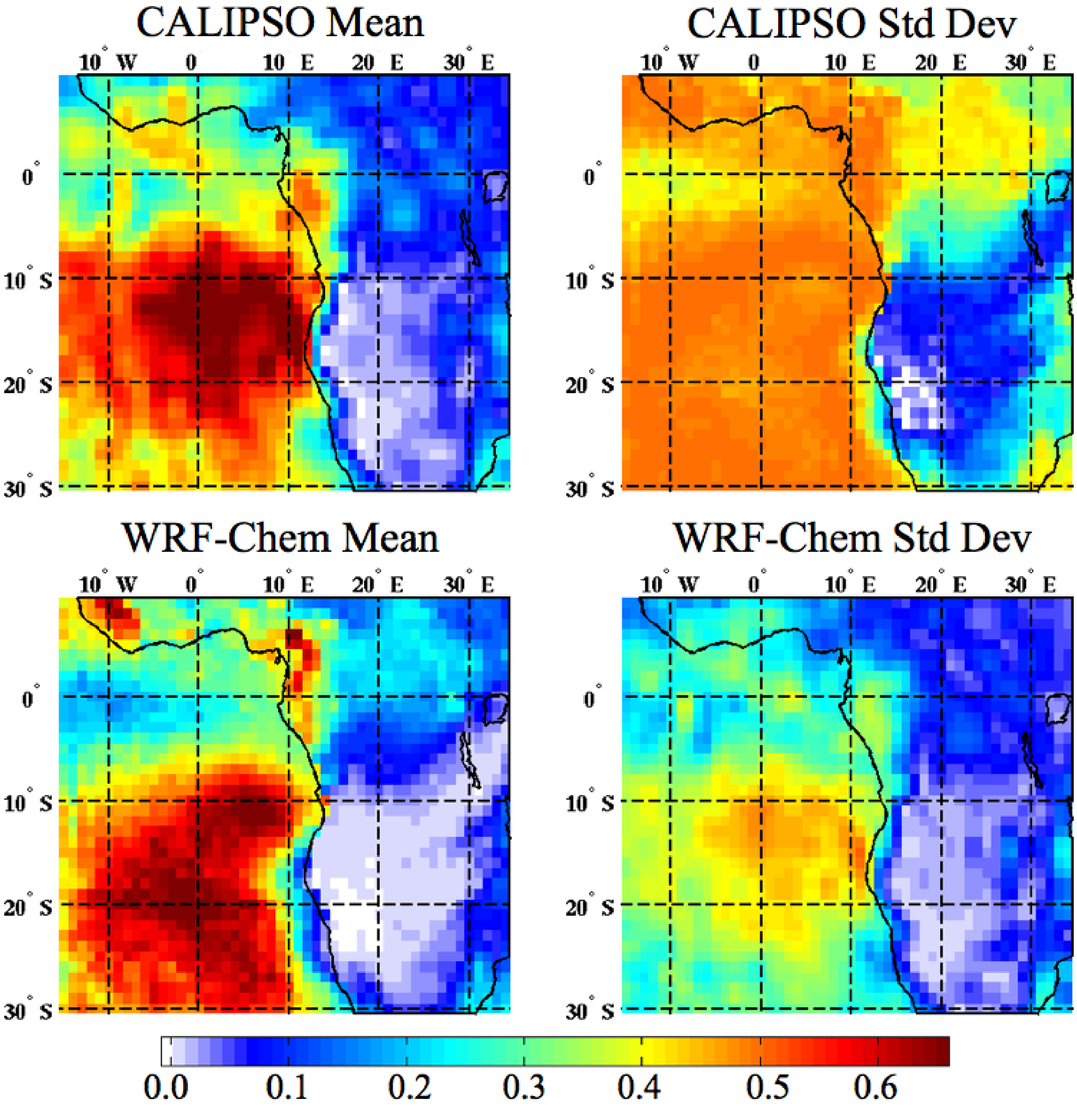

Figure 2.25: Comparison of mean low cloud (base > 680 hPa) frequency/fraction from CALIPSO with model.

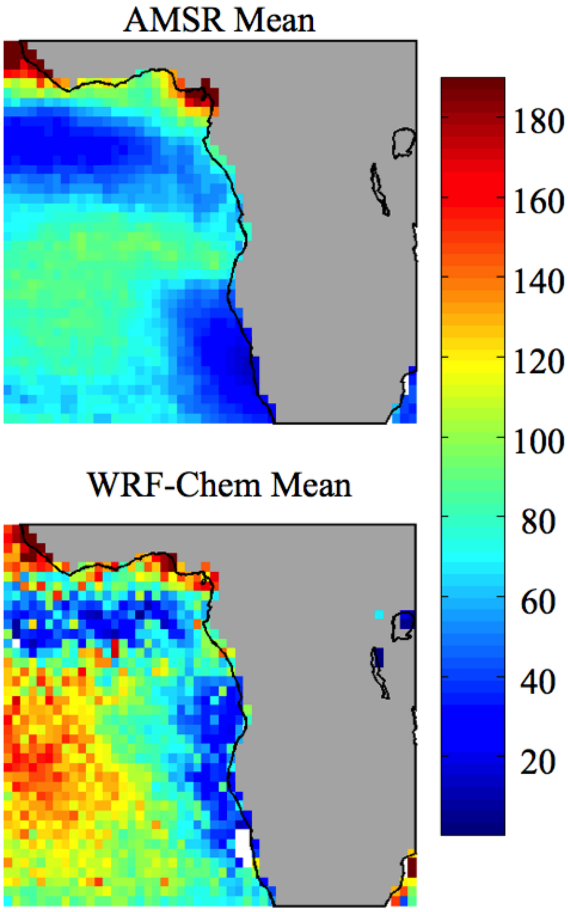

Figure 2.26: Comparison of mean integrated cloud liquid water path ($g/m^2$) from AMSR with model.

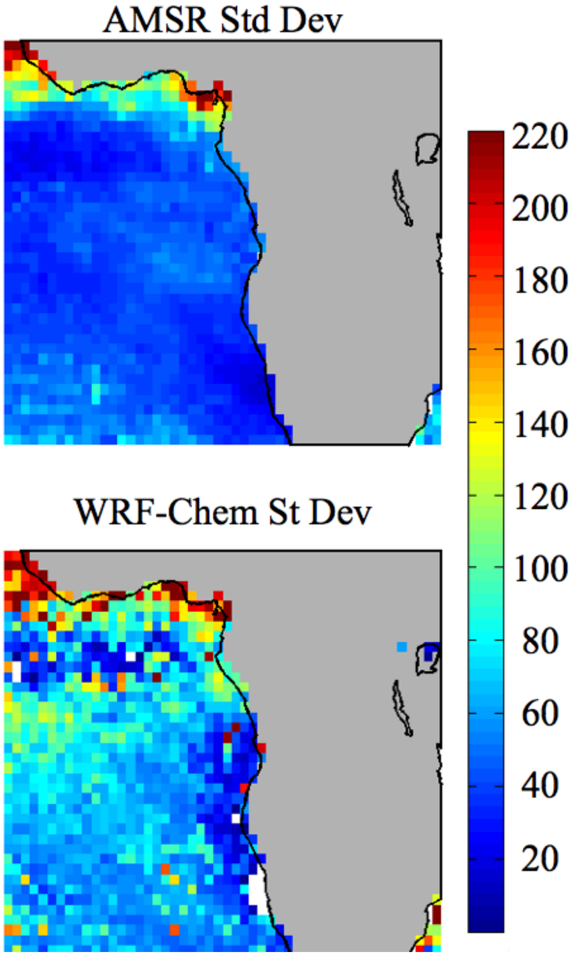

Figure 2.27: Comparison of standard deviation of integrated cloud liquid water path ($g/m^2$) from AMSR with model.

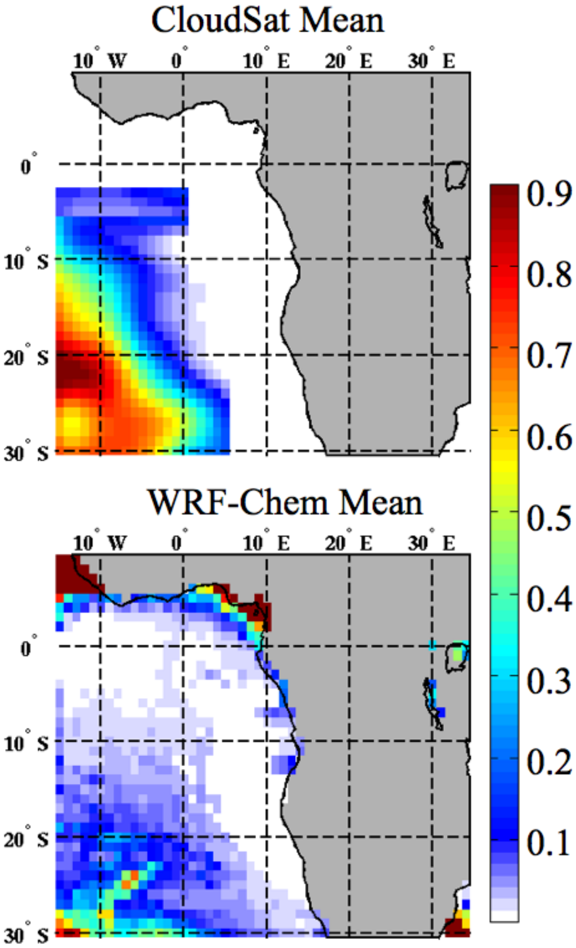

Figure 2.28: Comparison of mean rainfall rates (mm/hr) from MODIS with model.

Surface rainfall is a difficult parameter to measure and model in stratocumulus regions where precipitation rates are small. Climatological mean July - October rainfall rates from the CloudSat instrument are compared with modeled surface rain rates (fig. 2.28). The model is able to capture the spatial pattern of precipitation fairly well, and represents the south-westerly gradient in rainfall rates. Both modeled and observed precipitation peaks at 0.8-0.9 mm/day in the southwest of the domain, decreasing to 0.05-0.1 mm/day at the edge of the Sc cloud area. CloudSat precipitation values are larger throughout much of the oceanic domain. In the area 10-15S, 0-10W where most of the precipitation changes occur in our analysis, rainfall rates for WRF-Chem are 0.05 - 0.25 mm/hr, while CloudSat rainfall rates are 0.05-0.5 mm/hr.

Cloud droplet concentrations from MODIS are compared with WRF-Chem (fig. 2.29). The model accurately represents the spatial extent of high Nd values extending in a northeasterly arc from the Angolan coast towards the equator. Nd concentrations for MODIS and the model are both in the 80-100 $cm^{-3}$ range in this area. WRF-Chem's highest mean values of Nd extend further offshore than MODIS.

Ao et al. (2012) described a method for determining planetary boundary layer height (PBLH) from GPS radio occultation (GPSRO) measurements (via the COSMIC instrument). PBLH is defined as the height at which the vertical gradient of the refractivity is a minimum. Refractivity is related to the thermodynamic properties of the atmosphere through the relationship:

$$N = a1\frac{P}{T} + a2\frac{P_w}{T^2}$$

where T is the temperature, P is the total pressure, $P_w$ is the water vapor partial pressure, with constants $a_1 = 77.6K/hPa$ and $a_2 = 3.73x10^5K^2/hPa$. PBLH can be determined in many ways; refractivity PBLH was chosen because it is measured to high vertical accuracy and in the model, it is well-defined over the whole domain and agrees fairly well with other metrics over the marine Sc zone (not shown). PBLH from COSMIC and WRF-Chem are shown in fig. 2.30. The model differs from the GPSRO

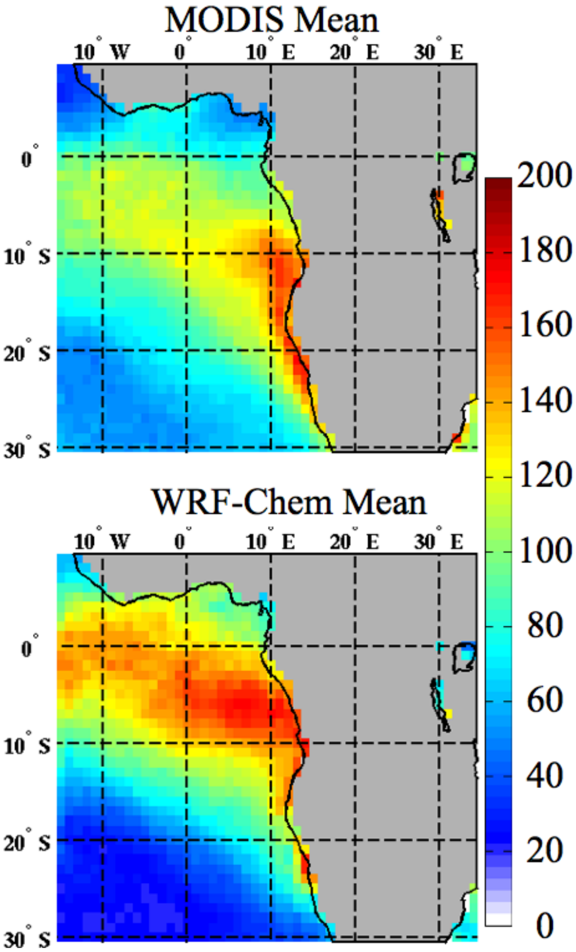

Figure 2.29: Comparison of mean cloud droplet concentration ($cm^{-3}$) from MODIS with model.

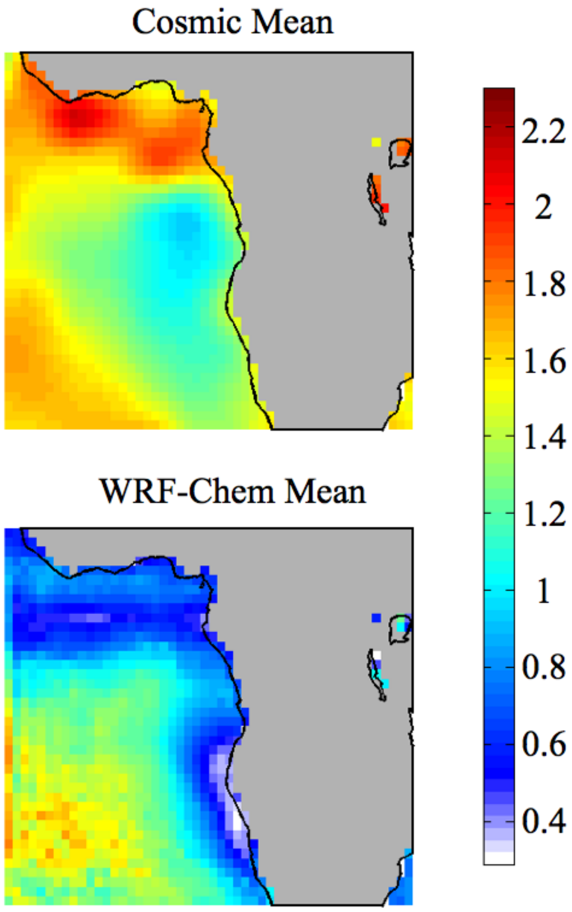

Figure 2.30: Comparison of mean planetary boundary layer height (km) from COSMIC with model.

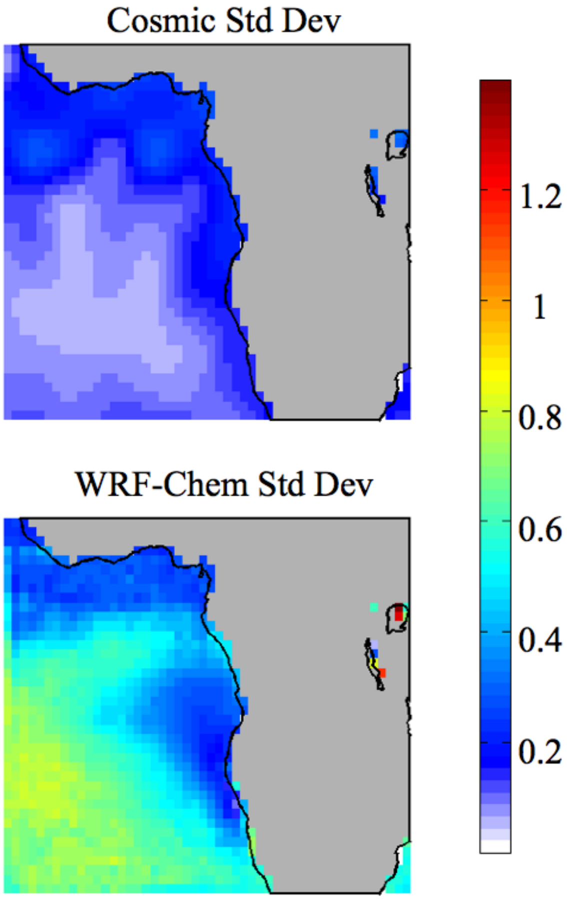

Figure 2.31: Comparison of standard deviation of planetary boundary layer height (km) from COSMIC with model.

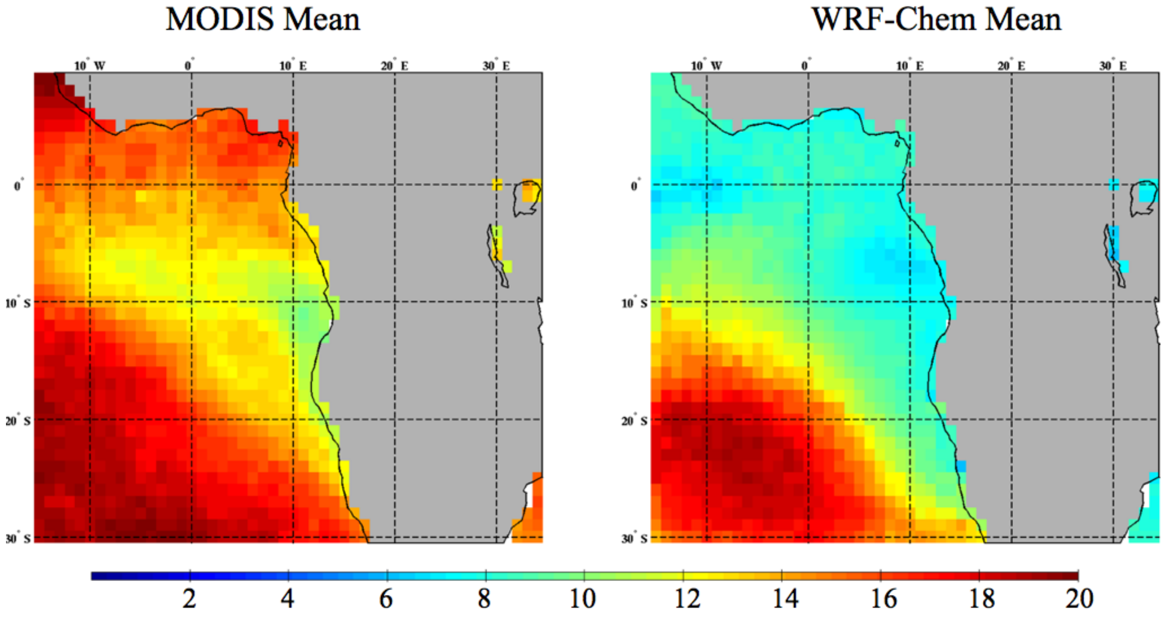

Figure 2.32: Comparison of vertically averaged cloud droplet effective radius (microns) from MODIS with model.

observations most strongly in the Sc-Cu transition region north of the equator, likely because the model does not include shallow convection in the interest of sustaining low clouds in the Sc region. The model also simulates an unrealisitcally shallow boundary layer near the coastline, a problem that has been observed in WRF-Chem previously ([81]). Beyond these issues, the model and observations both show local minima off the Angolan coast with deepening boundary layers to the southwest. The model and observations display variability in the same areas (fig.2.31) except the GPSRO has much lower variability in general.

Mean MODIS retrieval of daytime estimated effective cloud droplet radius is compared to the mean simulated value of vertically averaged effective cloud droplet radius in fig. 2.32. The WRF-Chem $R_e$ is calculated from a simple parameterizaton from Martin et al. ([71]) relating $R_e$ with $R_v$, the volumetric average radius if the cloud

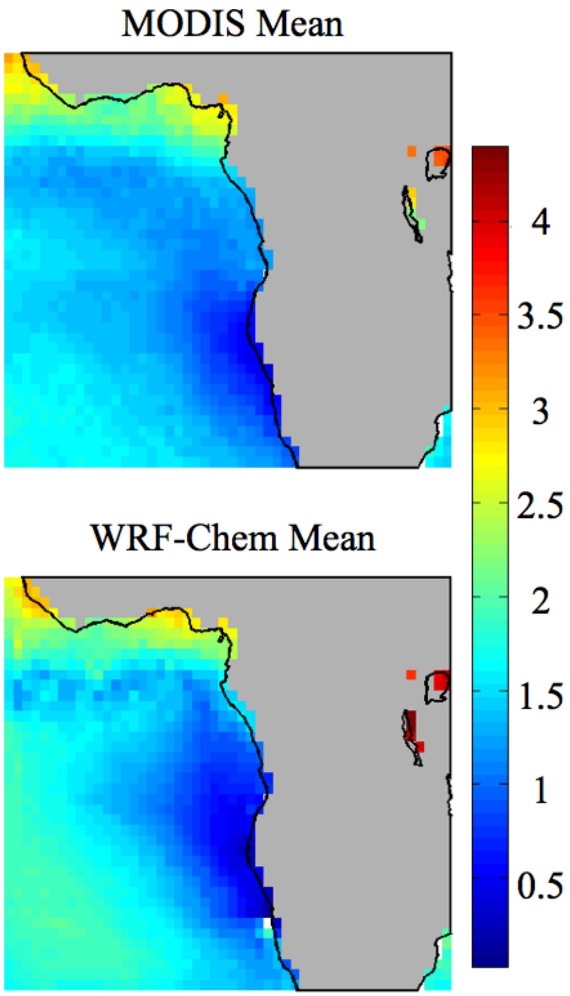

Figure 2.33: Comparison of cloud top height from MODIS with model.

liquid water were distributed equally over all cloud droplets.

$$R_v^3 = kR_e^3$$

where $k = 0.8$, a typical value for marine stratocumlus, is used. WRF-Chem captures the general pattern and magnitude of mean $\mathrm{R_e}$ in the stratocumlus area, with mean $\mathrm{R_e}$ between 12-20 microns.

MODIS cloud top height is calculated according to Zuidema and Painemal et al ([113]) from cloud-top temperature and sea surface temperatures. WRF-Chem cloud

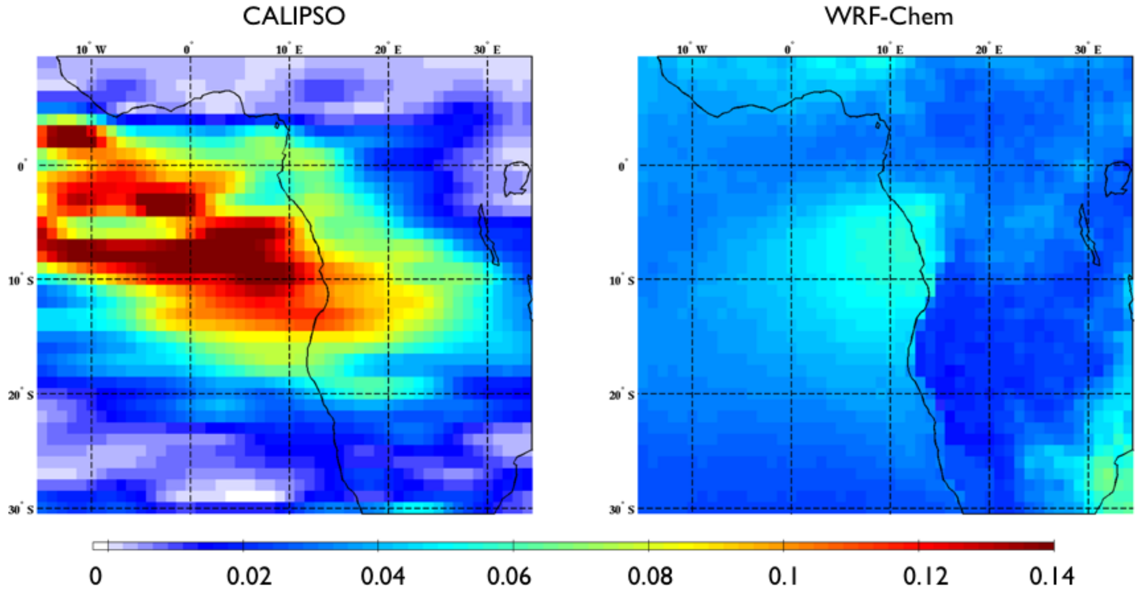

Figure 2.34: Comparison of above cloud aerosol optical depth from CALIPSO with model.

top heights are taken directly from the model as the height of the highest cloudy layer in the model at any given place and time. These metrics compare very well in the mean (fig. 2.33) over most of the ocean, except near the Angolan coast where the model PBL heights are too shallow. Cloud top height is related to boundary layer depth, but ultimately more important for considering cloud-aerosol intersections, so the faithful representation of cloud top height boosts our confidence in the model.

### *2.2.3 Aerosols*

The models most egregious errors occur in its ability to simulate accurate aerosol mass concentrations. Formenti et al ([29]) collated aircraft measurements of several compounds detected in biomass burning plumes during the SAFARI2000 campaign. These data were collected in the region 16-24°S, 11-18°E between 2-6 km between 5-10 September, 2000 and reported in units of ng $m^{-3}$) at standard temperature and pressure. Fig. 2.35 shows time series during July - Oct 2007 of several species

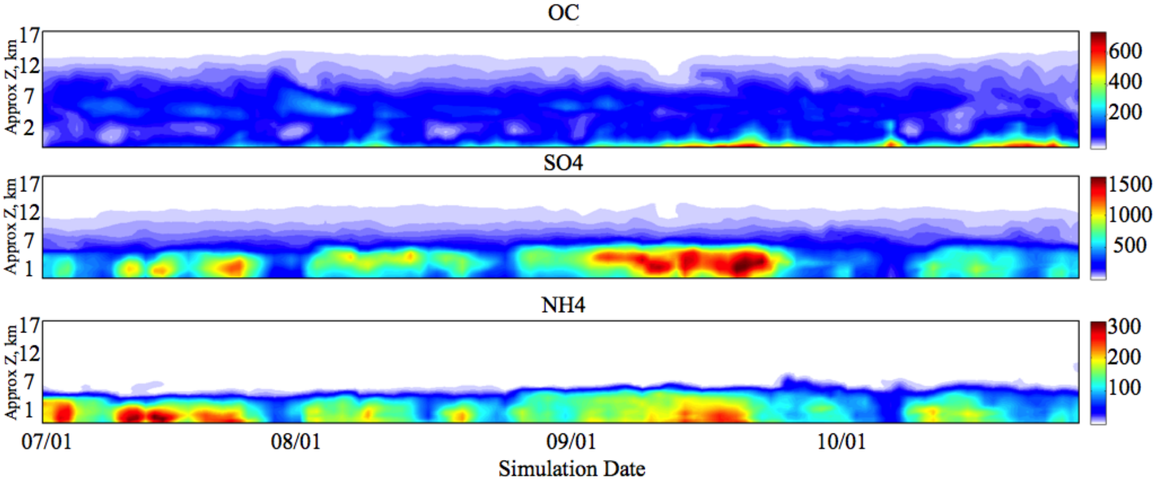

Figure 2.35: Accumulation and aitken mode concentrations of organic carbon, $SO_4^{2-}$, $NH_4^+$,$NO_3^-$ 16-24S, 11-18E, 5-10 Sept 2007. Units ng/m3 at STP.

averaged over the same horizontal region as Formenti et al ([29]). Modeled sulfate, which reaches concentrations of 1500 ng $m^{-3}$), compares reasonably well to observed values of 1984±1509 ng $m^{-3}$). Ammonia values, at 200-300 ng $m^{-3}$) are only a third of the observed values of 910±758 ng $m^{-3}$). Organic carbon aloft rarely exceeds 200 ng $m^{-3}$), a small fraction of the 6150±3628 ng $m^{-3}$) reported by Formenti et al ([29]).

The issues with aerosol mass representation are reflected in the aerosol optical depth predictions. Fig. 2.34 shows how CALIPSO often detects aerosol optical depths above cloud up to 0.20, with mean values near 0.15 in many places. WRF-Chem, meanwhile, produces above-cloud AODs that average 0.08 or less in most places. The model is able to generate plumes of aerosols with CCN concentrations exceeding 300-400 per cc, but the optical depths simply dont reflect that. Adjusting the internal-mixing mechanism didnt particularly help (not shown). The exclusion of absorbing aerosols from the model likely accounts for some of the errors. WRF-Chem also tends to badly underestimate secondary organic aerosol production ([50],[5]) which it is possible to address by using alternate chemistry mechanism, but those mechanisms unfortunately do not work with aerosol indirect effects. The input data for savanna

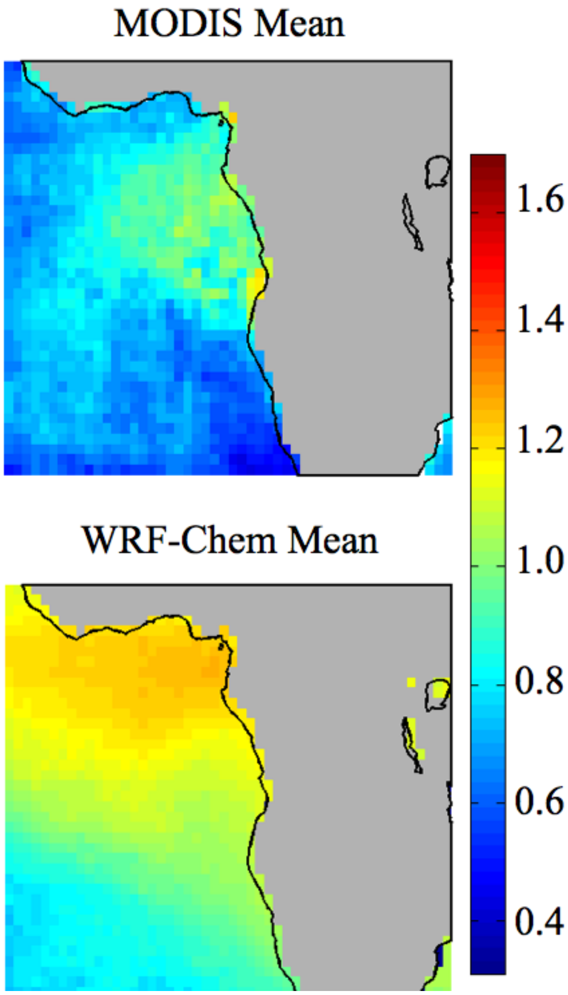

Figure 2.36: Comparison of mean Angstrom exponent from MODIS with model.

fires are also likely biased low relative to other emissions datasets (e.g. RETRO), as noted by Weidenmyer et al ([106]). This discrepancy in AOD means we need to scale the optical metrics used to determine the presence of aerosols in the model. Impacts from aerosols on clouds are very likely underestimated.

The model does a much better job representing the wavelength dependence of aerosol optical depth, the Angstrom exponent (fig. 2.36). Angstrom exponent values of 1-2 are typical of biomass burning aerosols. WRF-chem produces a broad area

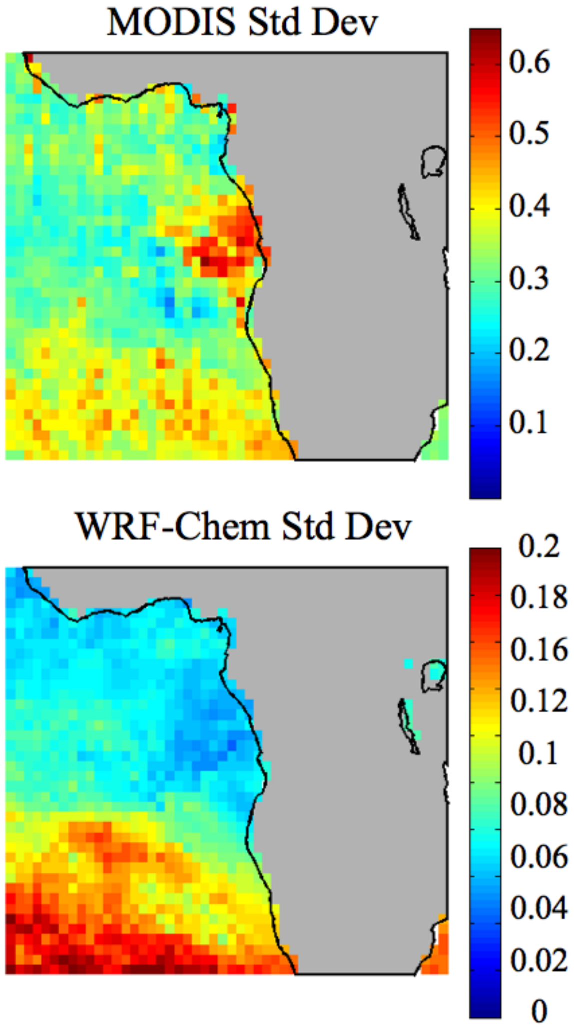

MODIS Std Dev

WRF-Chem Std Dev

Figure 2.37: Comparison of standard deviation of Angstrom exponent from MODIS with model.

of such values, suggesting the model disperses biomass burning aerosols more widely than the real world. Since dust is turned off in the model, BB aerosols are also the dominant contributor to the mean Angstrom exponent, which may help explain the spatial differences. Both MODIS and WRF-Chem show variability in the Angstrom exponent in the south of the domain, while WRF-Chem is has too little variability off the Angolan coast (fig 2.37).

AERONET data offers the best comparisons for AOD and Angstrom exponent. AERONET ground stations collect data continuously for the whole column during clear-sky daytime conditions. Unfortunately, only a few stations exist in the area of interest, and these are shown here. Mongu, Zambia is a continental site with 15 years of data located near the biomass burning source regions . Observed 440-675 nm Angstrom exponents at Mongu agree well in the mean with 400-600nm Angstrom exponents from WRF-Chem, but have a much larger spread– the model produces outliers only at lower and higher values(fig. 2.38). Observed 500nm AOD typically exceeds modeled 500nm AOD, with the models 75th percentile approximately equal to AERONETs 25th percentile (fig. 2.38). The spread of AOD values in WRF-Chem is also erroneously narrow. The same discrepancies in the spread of Angstrom exponents and deficiencies in AOD can be seen at the Etosha Pan, Namibia site, which is near the coastline (figs. 2.39). At Ascension Island, located 4000km off the coast in the Atlantic Ocean, the same problems persist (figs. 2.40).

There are a number of metrics one could use to detect an aerosol layer: a threshold of AOD, an extinction coefficient, a concentration of particles, a concentration of CCN, or some other chemical or optical property. For comparisons to CALIPSO aerosol layers, we use an extinction threshold of 0.02 to most closely mimic the capabilities of the LIDAR sensor (e.g. [109]). CALIPSO layer detections happen within a swath and the distribution of values from the swath are included in the processed data; for these comparisons of highest aerosol layer, the median value is used, and then averaged in time. For WRF-Chem, a single value of the highest aerosol layer is used. WRF-Chem

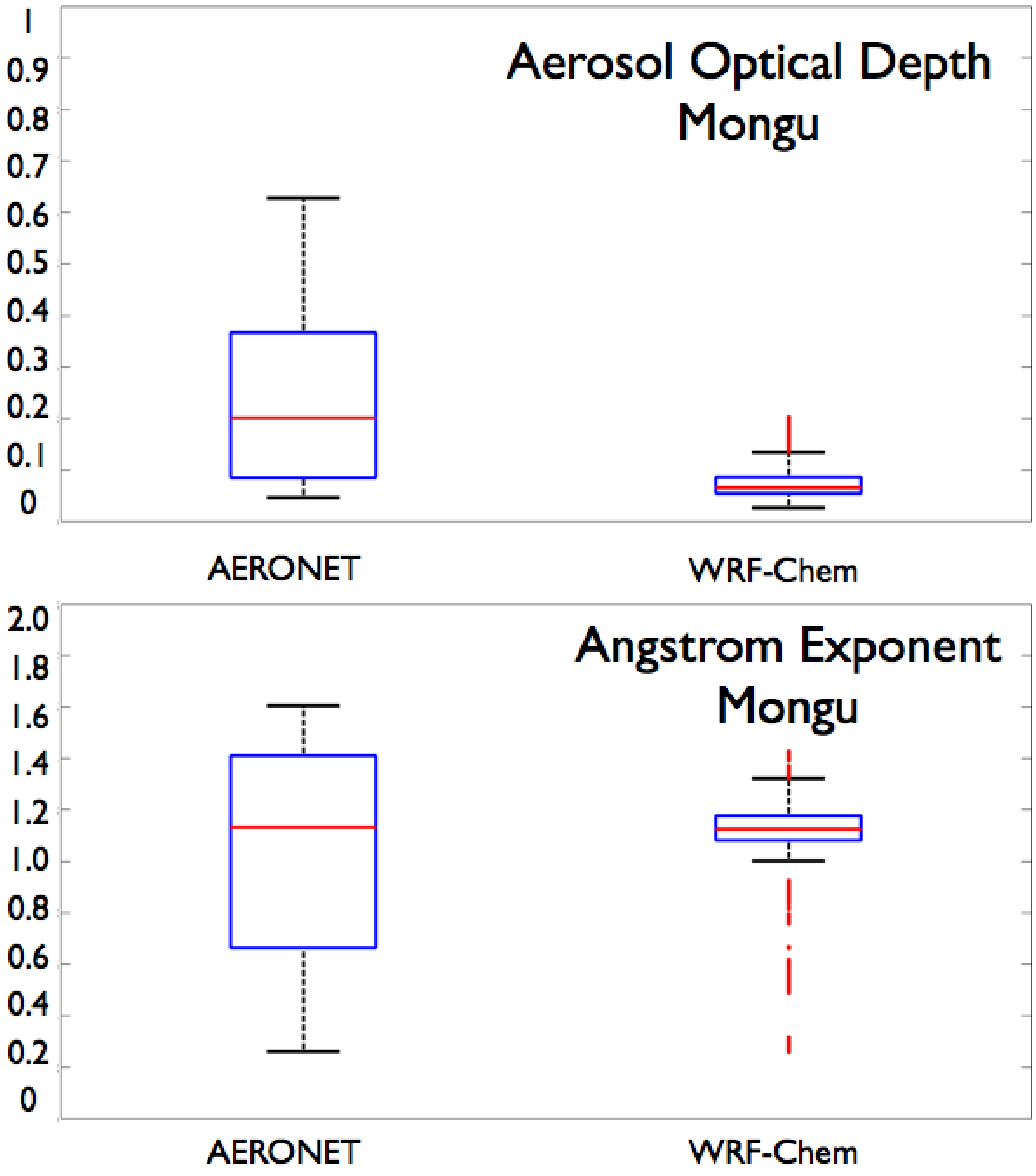

Figure 2.38: Comparison of clear sky aerosol optical depth and Angstrom exponent from AERONET at Mongu with model.

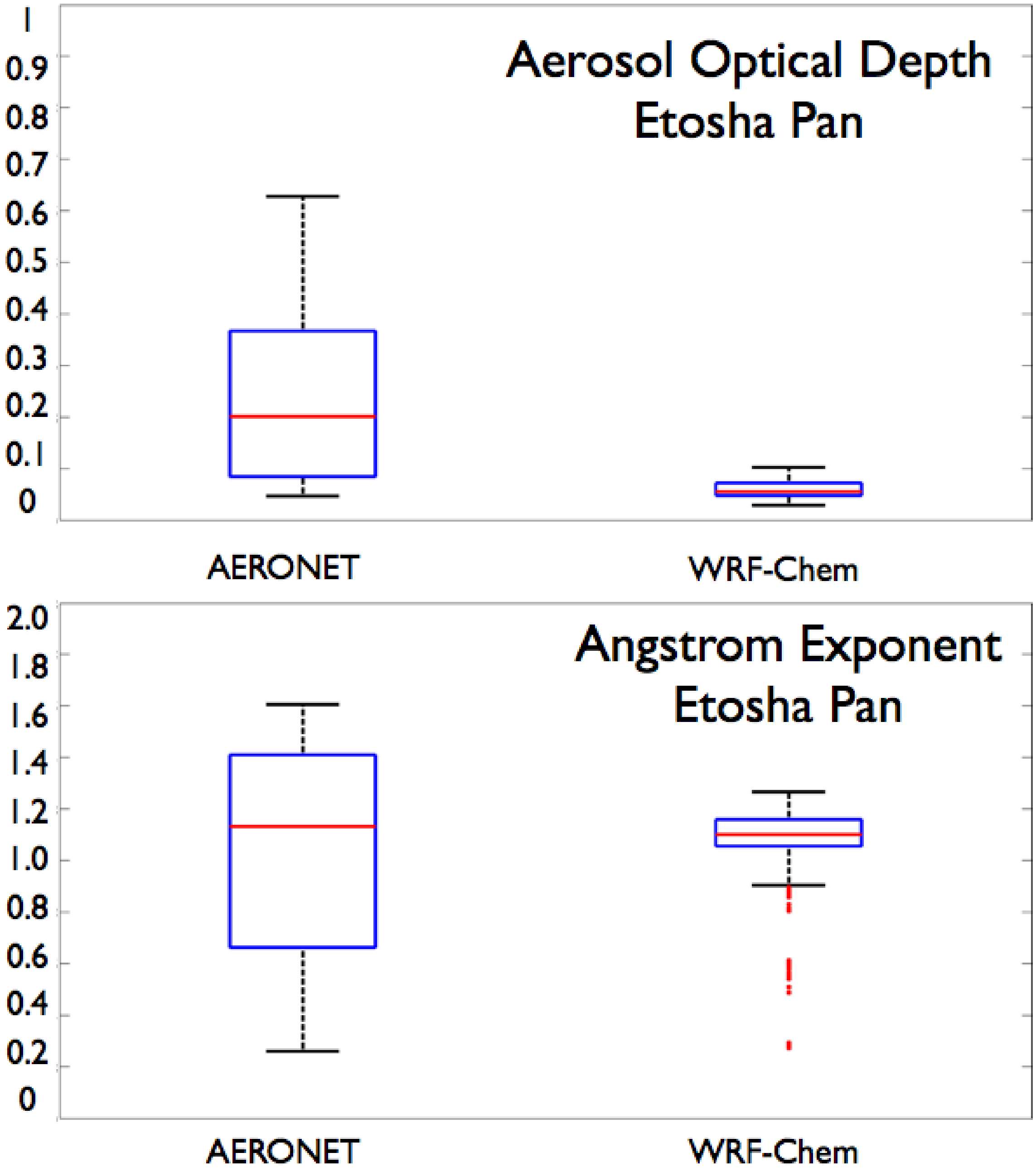

Figure 2.39: Comparison of clear sky aerosol optical depth and Angstrom exponent from AERONET at Etosha Pan with model.

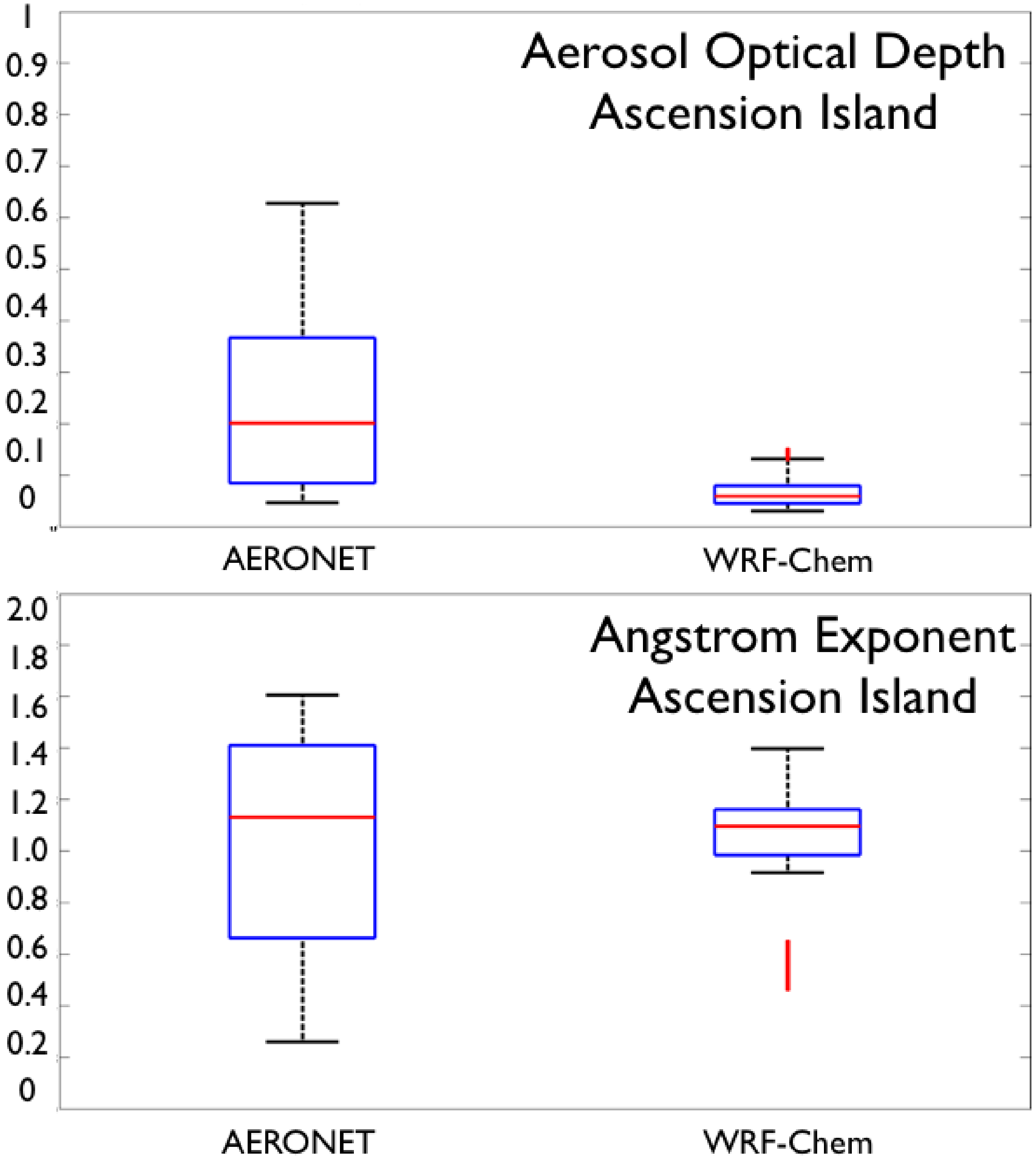

Figure 2.40: Comparison of clear sky aerosol optical depth and Angstrom exponent from AERONET at Ascension Island with model.

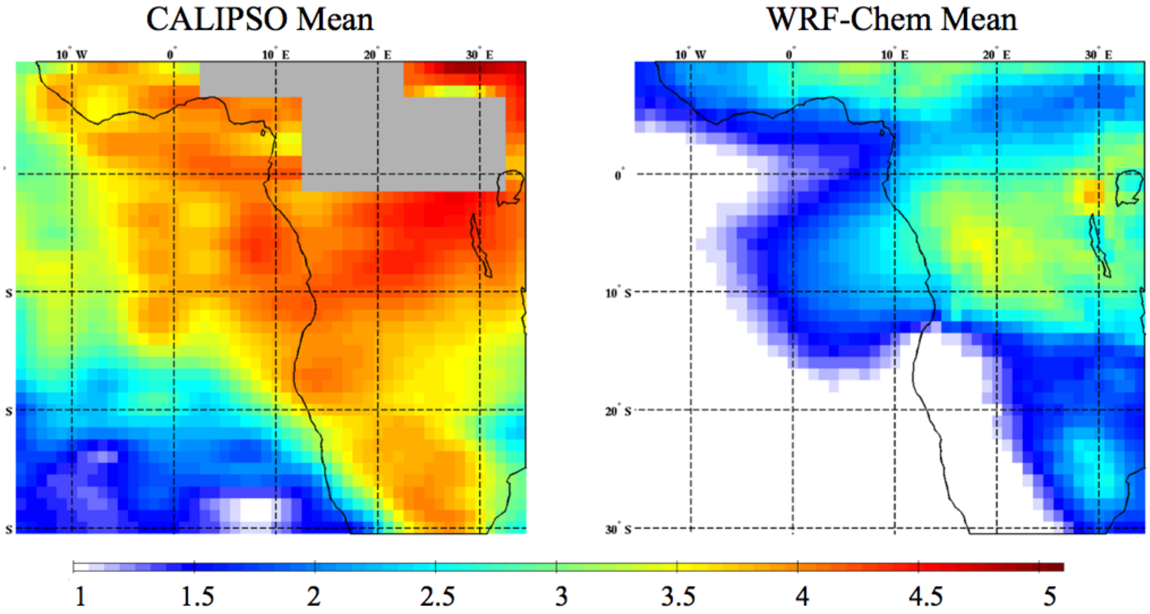

Figure 2.41: Comparison of mean highest aerosol layer determined by CALIPSO with model estimate based on same 0.02/km detection threshold.

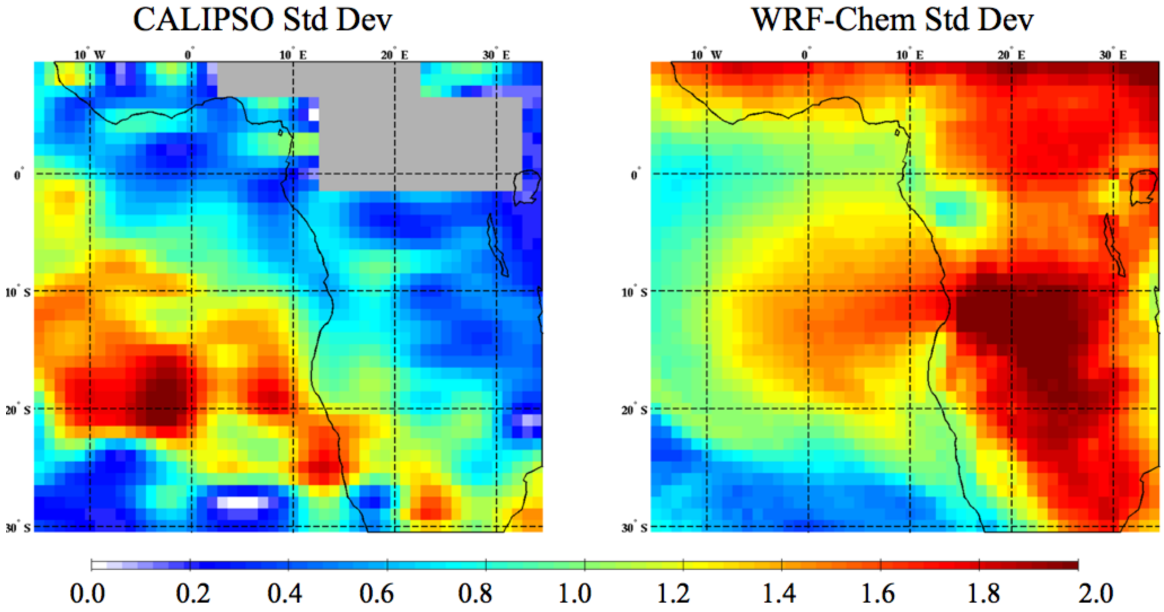

Figure 2.42: Comparison of standard deviation highest aerosol layer determined by CALIPSO with model estimate based on same 0.02/km detection threshold.

generates lofted aerosol layers at 3-4 km near the source region, similar to CALIPSO (fig. 2.41). The height of the highest aerosol layer declines off-shore, albeit more strongly for WRF-Chem (to 1-2km vs 2-3km). CALIPSO has a much larger area of lofted aerosols, possibly because more aerosols (e.g. dust) are represented in the observations. WRF-Chem assigns more variability in the continental interior, whereas CALIPSO detects more variability over the oceans (fig 2.42).

### *2.2.4 Summary of WRF-Chem Comparisons to Observations*

WRF-Chem simulations of meteorology, cloud variables, and aerosol variables were compared to reanalysis, remote sensing, and ground observations. The most pressing concern is that WRF-Chem aerosol mass concentrations are biased low by a factor of 2-3 overall, with the main discrepancy existing in the mass of organic compounds. These biases are reflected in the aerosol optical depth, which is a factor of 2-3 too low relative to observations. Consequently, aerosol-driven responses in the model will likely be underestimated.

WRF-Chem produces very good representations of the meteorology, including height and wind fields. Cloud properties are fairly well represented, particularly the cloud fraction and droplet concentration. On average, liquid water path is overestimated while rain rates are underestimated. Responses in these variables should be considered in this context.

# Chapter 3

# RESULTS

## *3.1 Mean Differences between Simulations with and without biomass burning (non-carbonaceous) emissions*

### *3.1.1 Cloud and lower tropospheric properties*

Two model simulations were analyzed: BBon and BBoff. These simulations were set up in identical ways except for the inclusion of Southern African biomass burning aerosols in BBon. They are forced with the same meteorological conditions every six hours and with the same chemical boundary conditions (both lacking organic carbon to minimize aerosol advection from sources external to the domain). Mean differences between BBon and BBoff are therefore interpreted as being caused by aerosol macrophysical and microphysical effects, which may include impacts on intra-domain meteorological variability. Differences in means are determined to be statistically significant at the 1-sigma level after accounting for autocorrelation.

Concentrations of CCN (for supersaturation S = 0.2%) at 850hPa in the BBon simulation exceeded those in BBoff by 20-100$cm^{-3}$ on average (fig. 3.1). BBoff has aerosol sources from secondary oxidation of non-combustion biogenic emissions, industrial emissions, DMS and non-open burning. The positive contribution from Southern African open burning represented by the difference BBon-BBoff of CCN is concentrated between 2.5°N - 10°S latitude, but extends southward and to the western edge of the domain. The increase in CCN at 850hPa coincides spatially with a strong (20-90$cm^{-3}$) average increase in the cloud droplet concentration (fig. 3.3) as the aerosols entrained into the boundary layer uptake liquid water to form cloud droplets. These droplets are, on average, 0.5-3.5 microns smaller (fig. 3.4), in spite

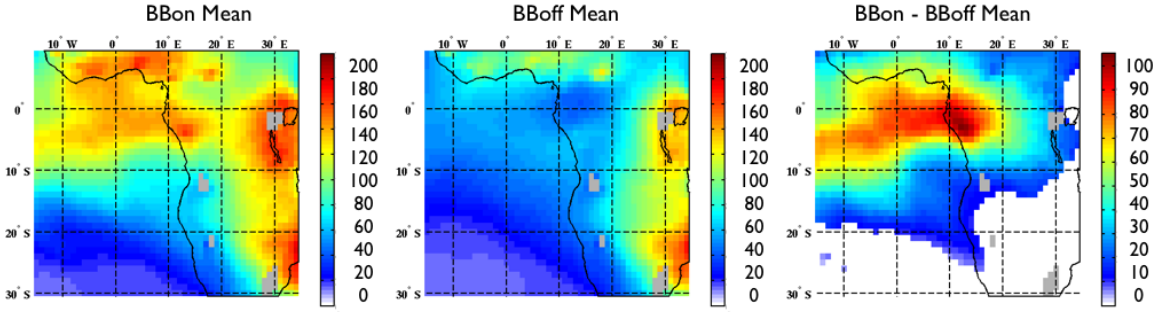

Figure 3.1: Mean values of CCN at 4km (per $cm^3$) for simulations (left to right) BBon, BBoff, and the difference between BBon - BBoff

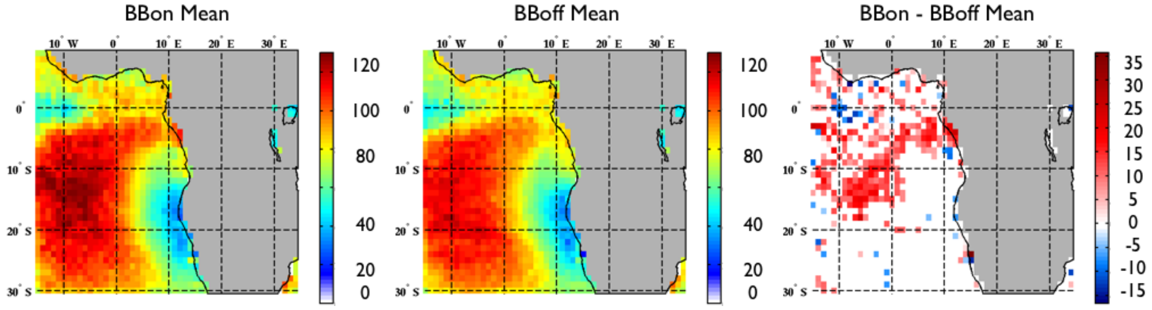

Figure 3.2: Mean values of cloud liquid water path (g/m$^2$) for simulations (left to right) BBon, BBoff, and the difference between BBon - BBoff

of increased liquid water path (fig. 3.2). An increase in cloud droplet concentration and a decrease in effective cloud droplet radius together indicate the potential for significant aerosol indirect effects as cloud properties respond to changes in their microphysics ([7],[78]). The set of modeled responses is shown to be consistent with these anticipated aerosol indirect effects.

Precipitation was strongly suppressed in the region of enhanced cloud droplet concentration and diminished effective radius. Smaller droplets collide and coalesce less efficiently, which tends to reduce the production of drizzle droplets. Fig. 3.5 shows the fractional decrease in precipitation. The change in cloud droplet size and concentration associated with biomass burning aerosols was co-located with an average

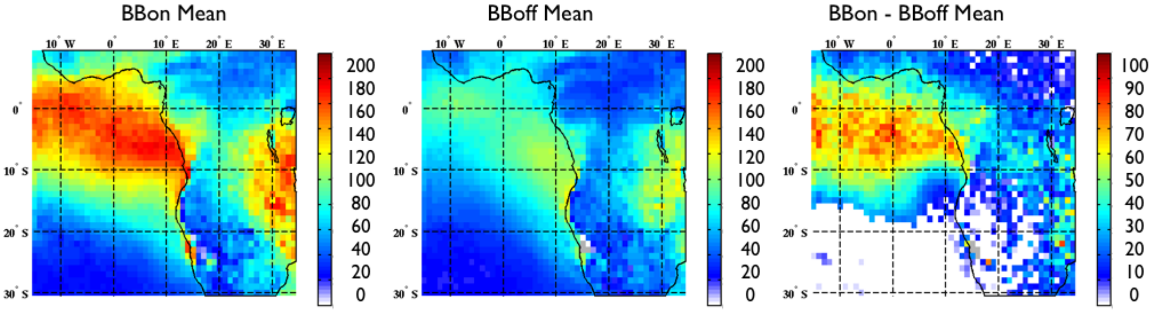

Figure 3.3: Mean values of vertically averaged cloud droplet concentration ($cm^{-3}$) for simulations (left to right) BBon, BBoff, and the difference between BBon - BBoff

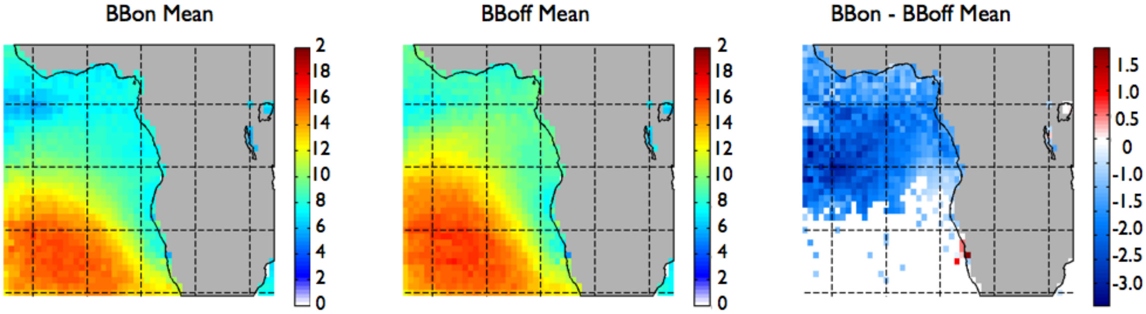

Figure 3.4: Mean values of vertically averaged cloud droplet effective radius ($\mu m$) for simulations (left to right) BBon, BBoff, and the difference between BBon - BBoff

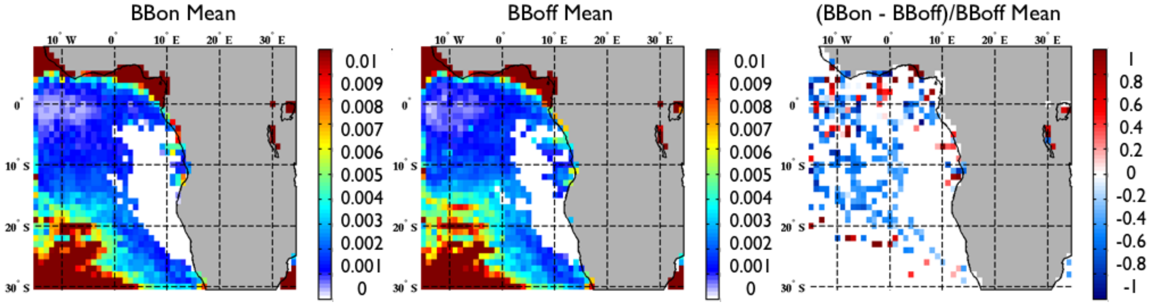
BBon Mean
BBoff Mean
(BBon - BBoff)/BBoff Mean

Figure 3.5: Mean values of precipitation $(\frac{mm}{hr})$ for simulations (left to right) BBon, BBoff, and the fractional difference $\frac{BBon-BBoff}{BBoff}$

decline in precipitation of 30-60%. This strong decline in precipitation allows clouds in the region to retain a greater quantity of liquid water, which contributes to an average increase in cloud liquid water path by 10-25 $\frac{g}{m^2}$. Wilcox et al. ([108]) observed a similarly strong increase in liquid water path, which this study was able to replicate despite the exclusion of absorbing aerosols in the model simulations.

We might reasonably expect the strong suppression of precipitation to influence the turbulent kinetic energy of the marine cloud-topped boundary layer. As drizzle droplets form, they release latent heat that warms the cloud layer and tends to diminish the buoyant production of turbulent kinetic energy, especially in downdrafts. Drizzle falling beneath the cloud-base causes evaporative cooling in the boundary layer which further diminishes turbulent mixing. Consequently, precipitation production tends to diminish the turbulent kinetic energy of the marine boundary layer. Strongly suppressed precipitation would tend to increase the net boundary layer turbulent kinetic energy, which is precisely what we see in the model results (3.6) as TKE is increased 0.5-1.5 $\frac{m^2}{s^2}$ in the region of strong precipitation suppression. The area of enhanced TKE is co-located with low cloud top heights increased by 25-100 meters (3.7) which suggests the increased turbulence is driving greater cloud-top entrainment, deepening the cloud-topped boundary layer.

Low cloud cover responds negatively to enhanced cloud-top entrainment of drier

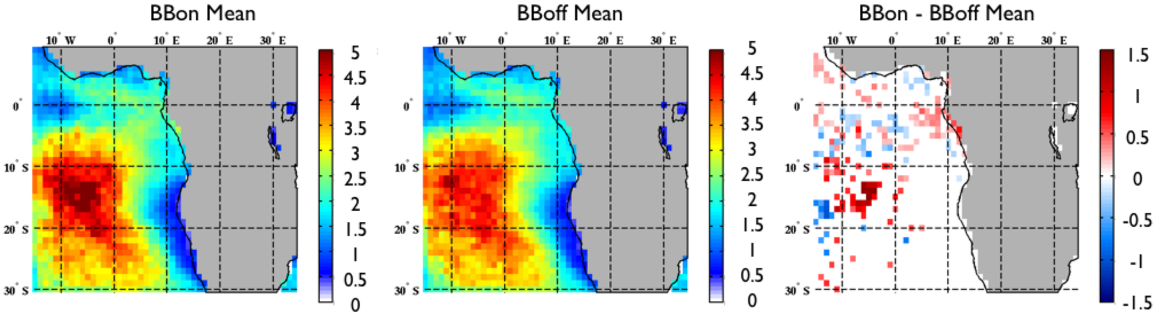

Figure 3.6: Mean values of net boundary layer turbulent kinetic energy ($\frac{m^2}{s^2}$) for simulations (left to right) BBon, BBoff, and the difference between BBon - BBoff

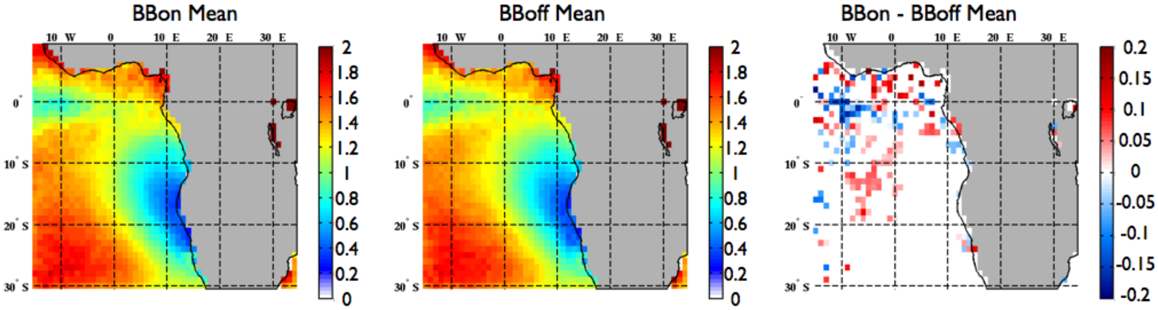

Figure 3.7: Mean values of mean low cloud-top height (km) for simulations (left to right) BBon, BBoff, and the difference between BBon - BBoff

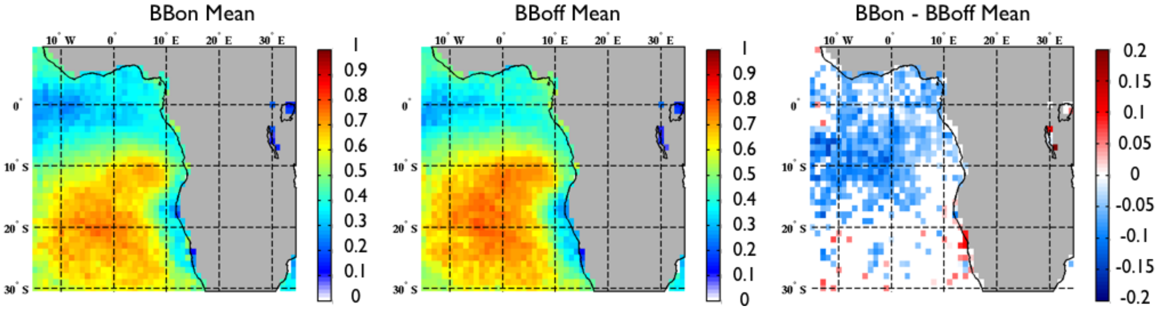

Figure 3.8: Mean values of low cloud frequency for simulations (left to right) BBon, BBoff, and the difference between BBon - BBoff

air from the free troposphere. Mean low cloud frequency maps for BBon and BBoff are shown in figure 3.8. BBon has 5-15% fewer low clouds than BBoff in the region off the Angolan coast from 0-20 ° S latitude where the cloud droplet concentration, effective radius, and turbulence signals are maximal. Low cloud cover and lower tropospheric stability (the vertical difference between potential temperature at 800hPa and potential temperature at 1000 hPa (similar [56])) are closely related: Decreased stability is associated with diminished moisture supply to the boundary layer which can reduce stratocumulus clouds, and reduced low cloud cover during daytime results results in a warmer sea surface reflected in reduced stability. Enhanced turbulent kinetic energy would be reflected in lower LTS, and increased cloud-top entrainment might evaporate low clouds. While it is difficult to determine the precise nature of the relationships among these cloud and boundary layer variables, the set of responses strongly suggests significant aerosol indirect effects stemming from changes in cloud droplets and precipitation rates. Notably, the modeled LWP response mimics previous research results including absorbing aerosols, while the low cloud and stability responses appear to oppose the findings of previous researchers ([108],[85]).

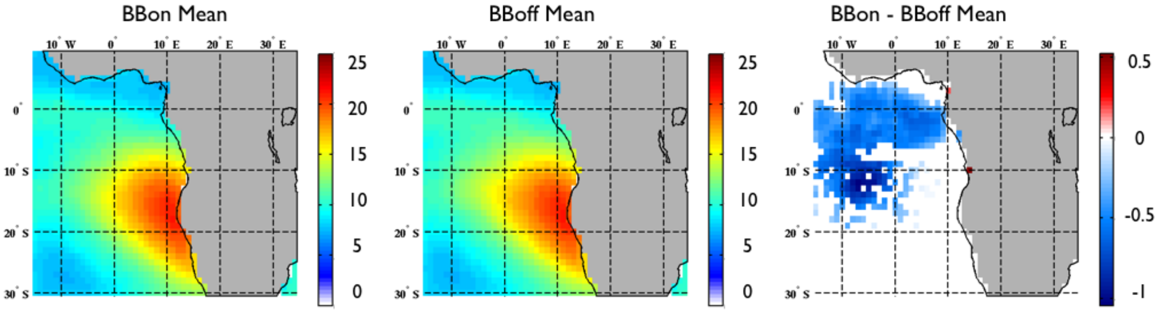
BBon Mean

BBoff Mean

BBon - BBoff Mean

Figure 3.9: Mean values of lower tropospheric stability ($\theta_{8}00 - \theta_{1}000$, K) for simulations (left to right) BBon, BBoff, and the difference between BBon - BBoff

### *3.1.2 Aerosol and Aerosol layer properties*

Aerosol layer properties, including their frequency, vertical extent, and height above clouds, are discussed for both model simulations to facilitate later analysis of the impact of these layers on cloud variability. The detection of aerosol layers relies on choosing a threshold 550 nm extinction coefficient, which is a diagnostic variable within WRF-Chem. The 550 nm extinction coefficient is used by CALIPSO as well to detect aerosol layers; the exact threshold is somewhat uncertain because the lidar measures backscatter, and the extinction to backscatter ratio (the lidar ratio) must be specified for BB aerosols ([76]). CALIPSOs detection threshold is approximately 0.02 $\text{km}^{-2}$ ([109]) for BB aerosols above clouds, which allows measurements of aerosol optical depth (fig. 2.34) and aerosol layer frequency. Fig 3.10, courtesy of Meloe Kacenelenbogen (NASA AMES) shows percent frequency of aerosols above clouds (AAC) for July-October 2006-2012. Both AOD and AAC counts were used to estimate an equivalent detection threshold for our model simulations, which we showed previously, underpredict the aerosol loading in the free troposphere. The ratio of model AOD to CALIPSO AOD suggests that a multiplier of 1.5-3.2 is appropriate to scale up the model AOD, or equivalently, scale down the extinction threshold used in the model for finding layers by a similar multiplier. Different thresholds were tested

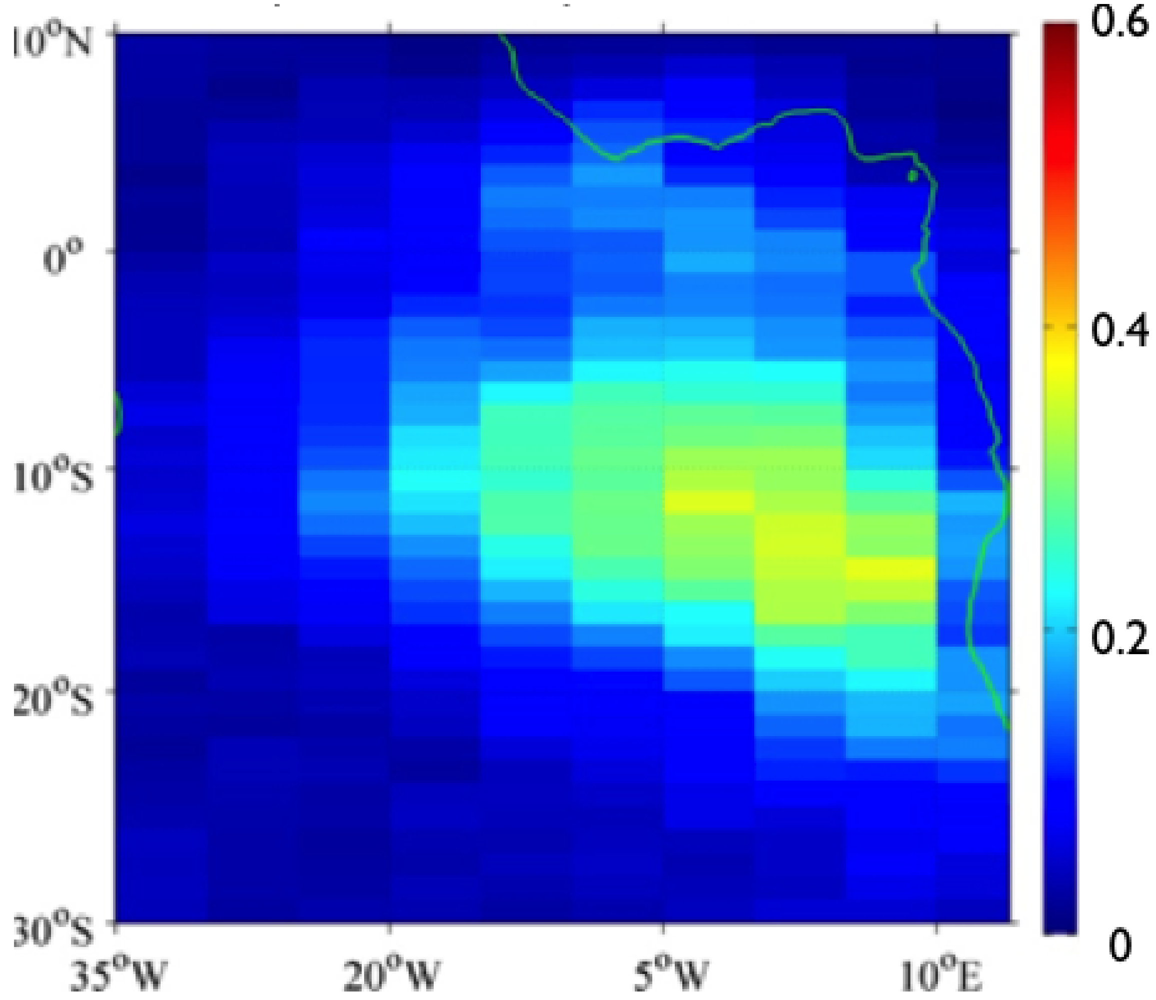

Figure 3.10: July - Oct 7 year mean value of CALIPSO frequency of aerosols detected above clouds.

within this range. An extinction coefficient threshold of 0.01 km$^{-2}$ (e.g. a multiplier of 2) was found to produce AAC frequency and scaled AOD that best resembled the observational data. Scaled AOD is shown in fig. 3.11, and AAC frequency for both BBon and BBoff are shown in fig. 3.12. In the BBon simulations, aerosol layers were detected above clouds 20-45% of the time with a strong local maximum off the coast at 10°S between 10°E and 0°E. In the BBoff simulations, AL were detected with a frequency of 0-17%, with most grid-points less than 10% frequency (fig. 3.12).

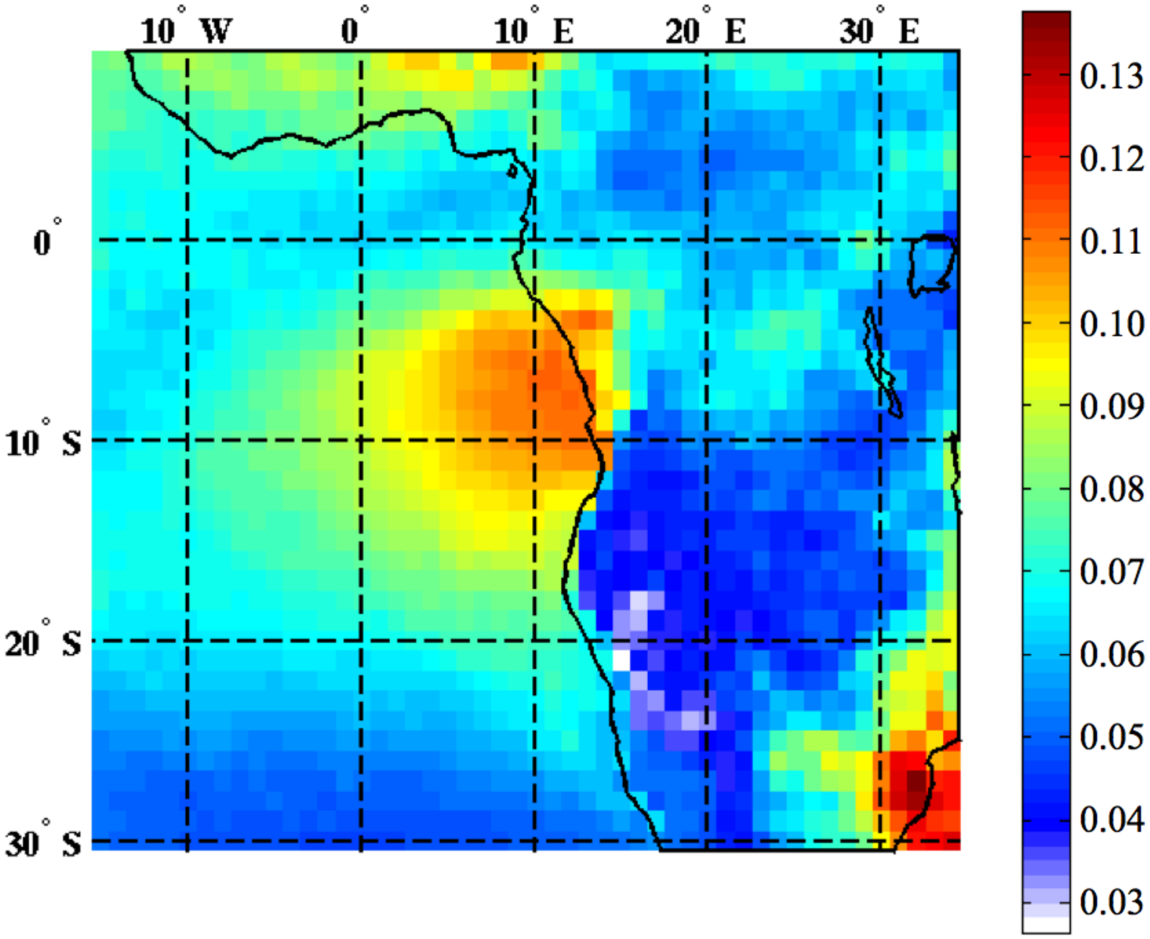

Figure 3.11: Mean value of above-cloud AOD from BBon simulation, scaled by a factor of 2.

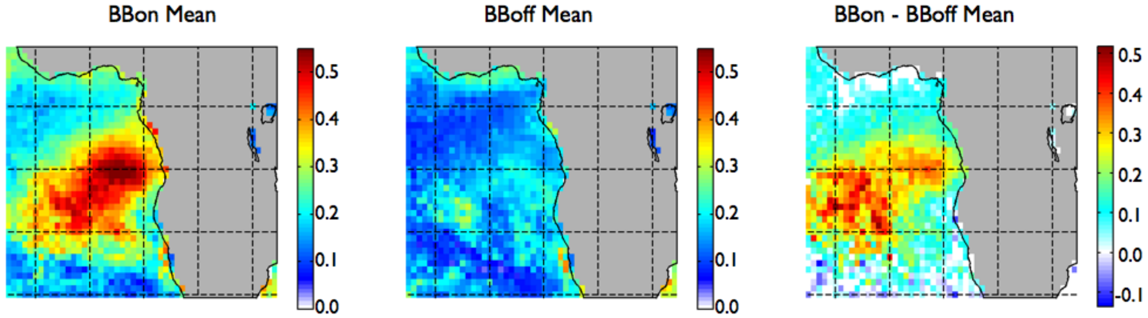

Figure 3.12: Mean values of frequency of aerosols above cloud using modified threshold, for simulations (left to right) BBon, BBoff, and the difference between BBon - BBoff

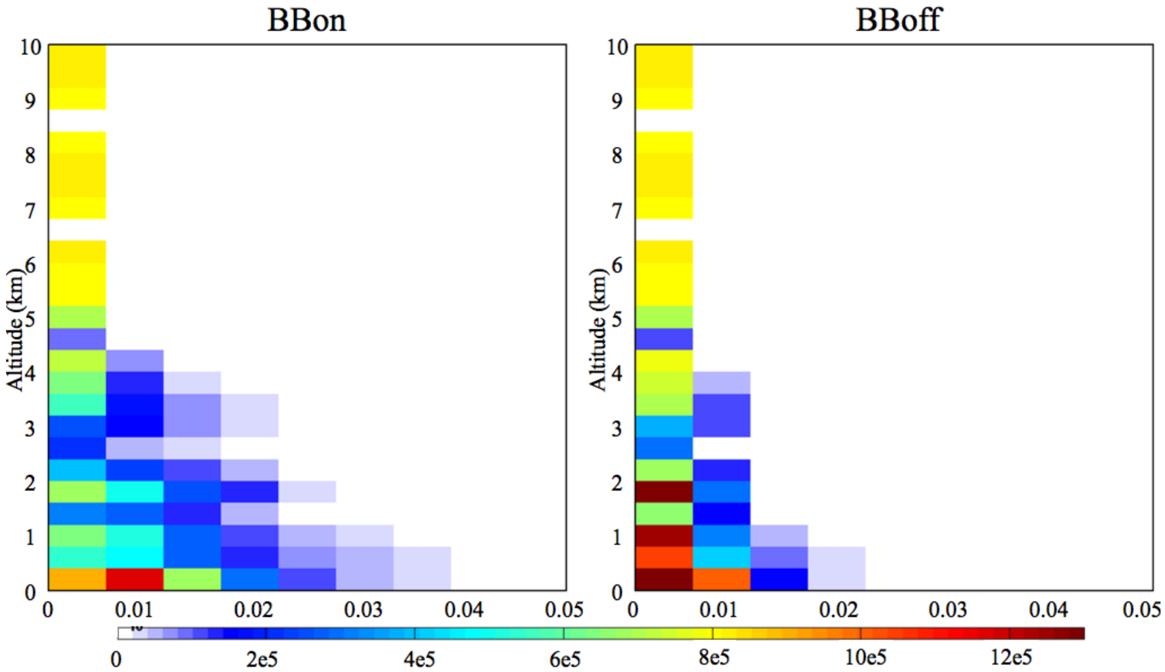

Figure 3.13: Combined frequency and distribution (CFAD) diagrams for 550nm extinction coefficient in BBon and BBoff. Extinction coefficient on x-axis, frequency in color.

Figure 3.13 shows combined frequency and distribution (CFAD) diagrams for 550nm extinction coefficient in BBon and BBoff. Data are binned first by height and then by magnitude, and instances are counted. The color scale ranges from 0 to $12 * 10^5$ occurrences among the $86 * 10^5$ hourly lat x lon data. Aerosols are present in both model simulations from several sources including DMS, so both simulations show low extinction coefficients at all levels, and frequent moderate extcof values near the surface. Consistent with Fig. 3.12, BBon has more frequent extcof exceeding the 0.01 $\mathrm{km}^{-1}$ threshold lofted above the surface than BBoff, but BBoff still has some lofted layers. We shall see later how the presence of non-biomass burning aerosols contributes to atmospheric conditions during synoptic-driven transport events.

Bearing in mind that the frequency of aerosol layers above clouds is considerably higher for BBon vs BBoff, we can consider the vertical geometry of these layers when

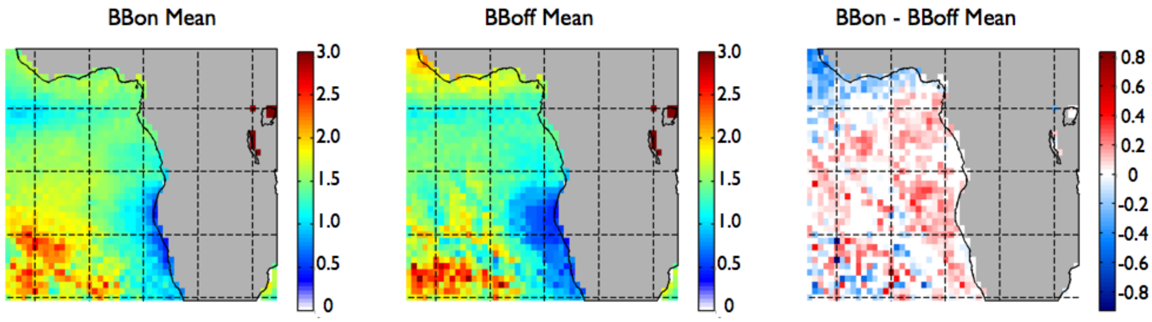

Figure 3.14: Mean values of lowest altitude of aerosols above cloud (km), for simulations (left to right) BBon, BBoff, and the difference between BBon - BBoff

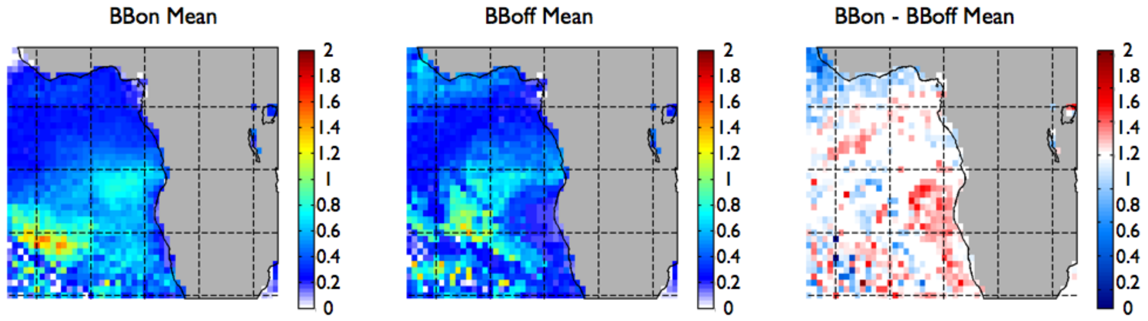

Figure 3.15: Mean values of vertical distance between aerosol layer and underlying cloud (km), for simulations (left to right) BBon, BBoff, and the difference between BBon - BBoff

they do occur. Microphysical cloud aerosol effects can only occur when the base of the aerosol layer intersect with cloud-tops. This requires that both cloud and aerosol layers occur simultaneously, and the cloud top height exceeds the height of the lowest aerosols. Since the presence of biomass burning aerosols influences the cloud top height via indirect aerosol effects, it may also alter the likelihood of those same microphysical interactions. The cloud top heights are increased on average by 25-100 meters (fig. 3.7) in the region 8.5-20°S, 0-10°W where the both rain rates and boundary layer turbulence responded to increased aerosol loading in the BBon simulation. On average, the height of the aerosol layer base is 100-600m greater under the influence of biomass burning in these simulations (fig. 3.14). The aerosol layer base altitude increases over a broad area extended to the coastline, where low clouds are frequently (50-60%) present (fig. 3.8). The increase in aerosol layer base on average exceeds the increase in cloud top heights over much of the low cloud areas so we might expect fewer opportunities for aerosol-cloud microphysical interactions in the presence of biomass burning aerosols. The vertical separation between aerosols and clouds, calculated at each time step, demonstrates 100-600m increases near the sub-equatorial western coast of Africa, consistent with the increase in aerosol base height (fig. 3.15). However, the average vertical separation actually decreases slightly in the region of increased cloud top heights, suggesting perhaps enhanced likelihood of microphysical interactions in the area where we have evidence the microphysical impacts are most significant.

## *3.2 Differences between Strong Easterly Flow and Weak Easterly or Westerly Flow*

### *3.2.1 Establishing the meteorological flow metric*

Many different quantities were tested to find a time-dependent meteorological metric to represent large-scale meteorological variations in aerosol and cloud fields. The metric needed to be a meaningful measure of large scale flow; similar between BBon

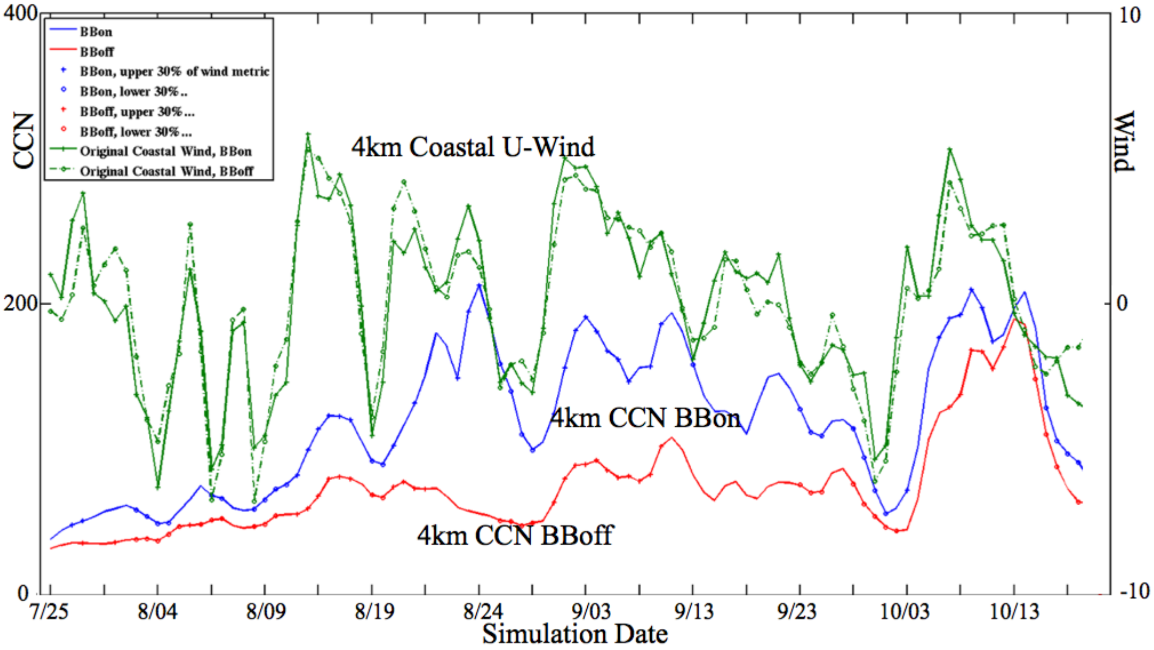

Figure 3.16: Time-series of daily averages of of the zonal 600hPa wind near the coast and the 4km CCN (at $S = 0.2\%$, in cm$^{-3}$) off the coast (12.5°S-2.5°S, 8.5°E-15.5°W)

and BBoff; with reasonable correlations with aerosols and cloud cover; and related to differences in other fields that are large enough to establish statistical significance with relatively few samples (123 days, less 10 days spin-up). 600hPa zonal wind near the Angolan and Namibian coasts (2.5°S to 12.5°S) was chosen to represent meteorological variability, and correlates particularly well with modulation of westward aerosol transport associated with a strengthening of the synoptic scale high pressure in the domain.

To construct the flow metric, the 600hPa zonal wind between 2.5°S-12.5°S was averaged over several longitude points near the coast (5.5°E to the coast at 8.5°E) to obtain smoother estimates. Daily averages were computed to reduce noise and a linear trend was removed to minimize seasonal influence and obtain a more statistically stationary time series focused on short-term weather variations. The sign is reversed so that strong positive values are associated with westward offshore transport events.

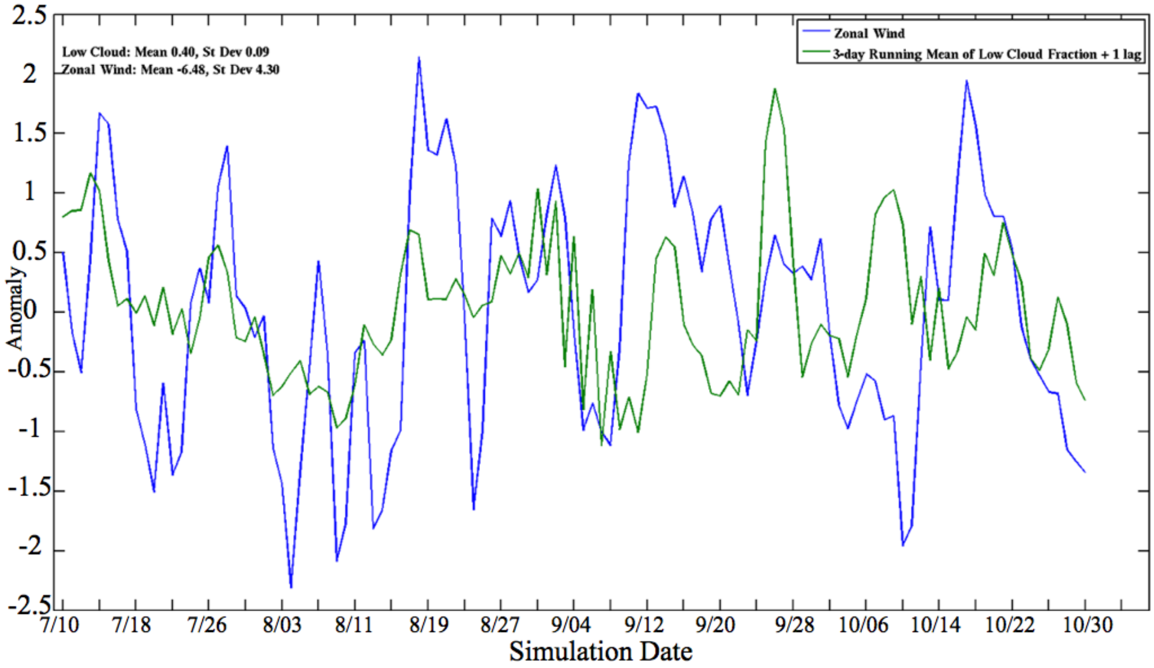

Figure 3.17: Time-series of the daily wind metric and the 3-day running mean of low cloud fraction off the coast (12.5°S-2.5°S, 8.5°E-15.5°W)

Figure 3.16 shows time-series of daily averages of of the zonal 600hPa wind near the coast and the 4km CCN (S=0.2%) off the coast (in the box 12.5°S-2.5°S, 8.5°E-15.5°W, where aerosol loading coincides with cloud cover). Signs are flipped so that positive flow is synonymous with off-shore flow. Data for BBon and BBoff simulations are shown. Later, we show how aerosol and cloud fields composited on the flow metric change. In fig. 3.16, markers are used to indicate where (on the CCN series), the standardized flow metric exceeds (or falls below) 70th (or 30th) percentiles of its distribution. This provides a sense of which CCN values are included in the composite populations. The zonal flow is very similar between BBon and BBoff; despite some differences in magnitudes, the time series peaks and troughs coincide which is important in a compositing sense. Beginning in mid-August, the winds exhibit extended 7-10 day easterlies aloft which is associated with increased CCN

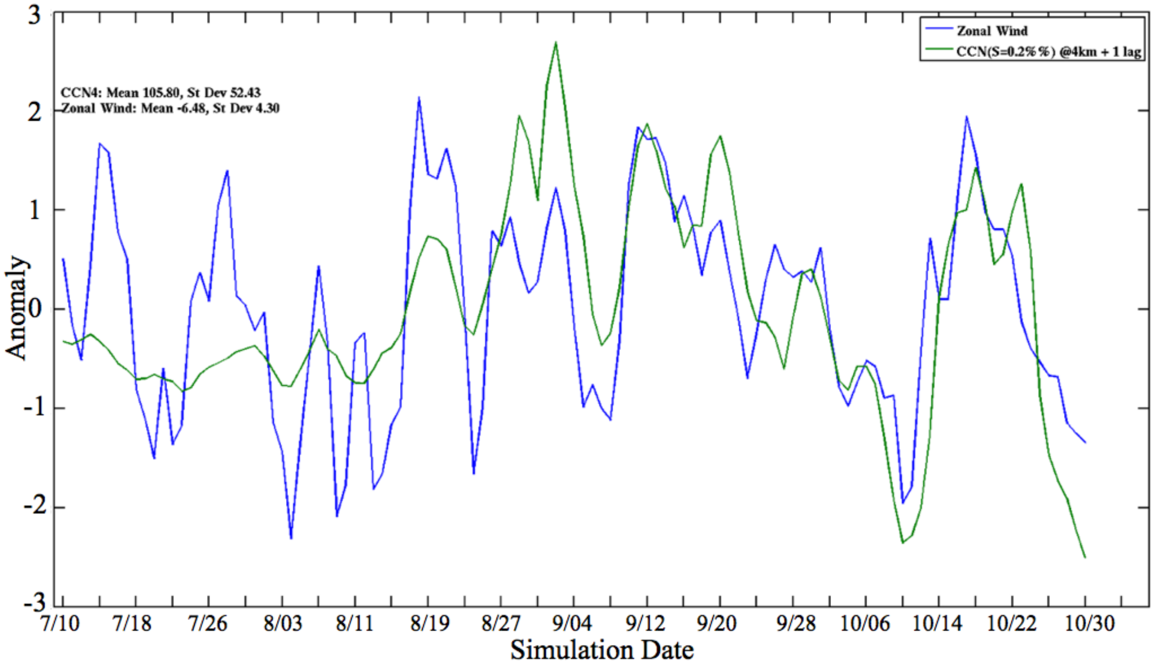

Figure 3.18: Time-series of the daily wind metric and the daily mean of CCN4 at 4km (at $S = 0.2\%$, in $\mathrm{cm}^{-3}$) off the coast (12.5°S-2.5°S, 8.5°E-15.5°W)

concentrations off the coast – in both simulations, but particularly for the BBon case. These extended periods of stronger easterly flow are likely necessary to transport aerosols far off the coast, a process that Swap et al ([93]) estimated takes 7-10 days. Curiously, BBoff and BBon have similar CCN at 4km from mid-October to the end of the simulation period, suggesting perhaps a biogenic SOA source or a flux of aerosol precursors from the boundaries.

As expected, in general the strongest responses in aerosol and cloud variables are lagged 1-2 days behind the coastal off-shore flow metric (e.g. lagged correlations between off-coast CCN4 and the flow metric, fig. 3.19). Fig 3.18 shows time-series from BBon of anomalies of the flow metric and 4km CCN (S = 0.2%) with a +1 day lag applied to the wind metric. The correlation between these time-series is R = 0.64, with an even stronger correlation (R = 0.83) for the period after mid-August. Fig

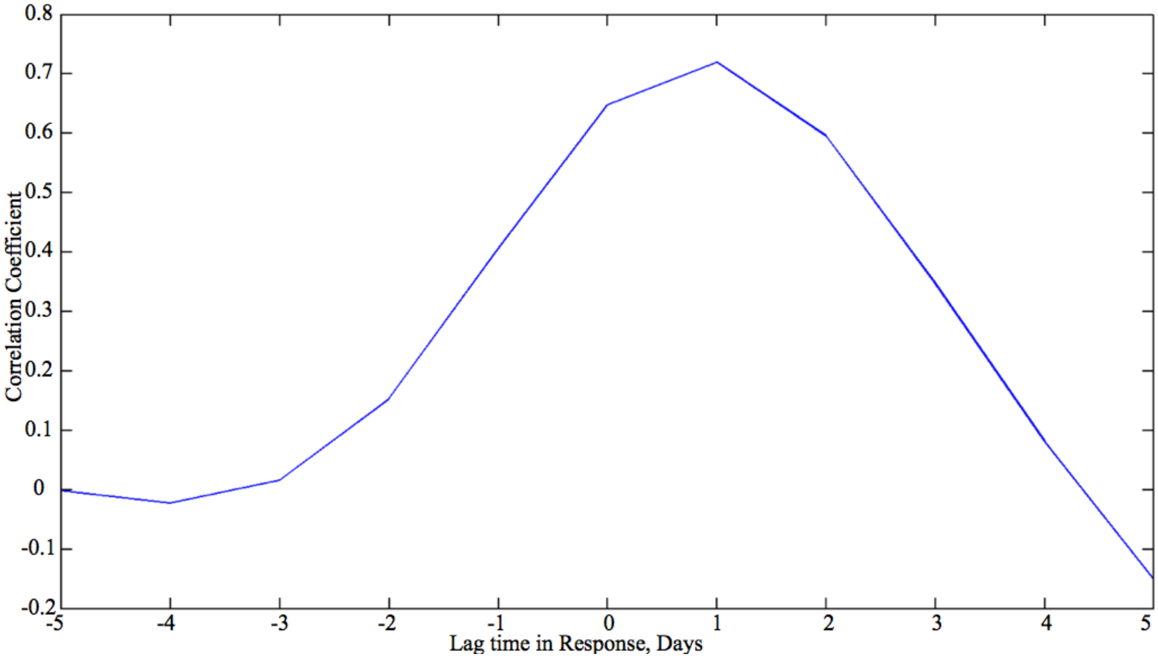

Figure 3.19: Lagged Correlation between wind metric and CCN4 at 4km (at $S = 0.2\%$, in $\text{cm}^{-3}$) off the coast (12.5°S-2.5°S, 8.5°E-15.5°W)

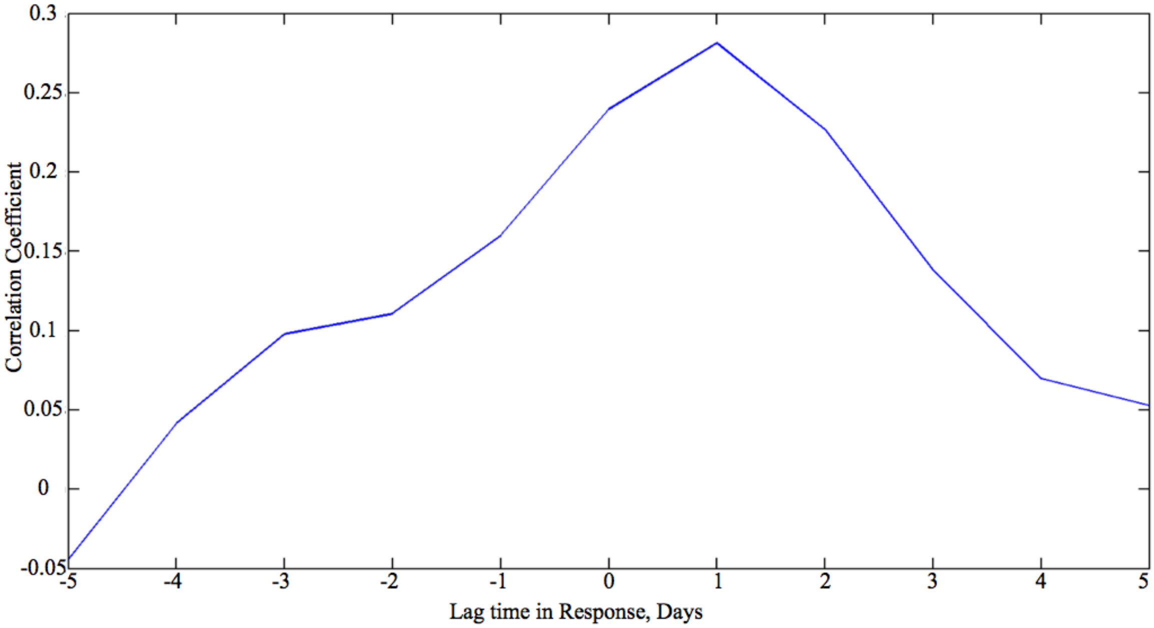

Figure 3.20: Lagged Correlation between wind metric and daily low-cloud fraction off the coast (12.5°S-2.5°S, 8.5°E-15.5°W)

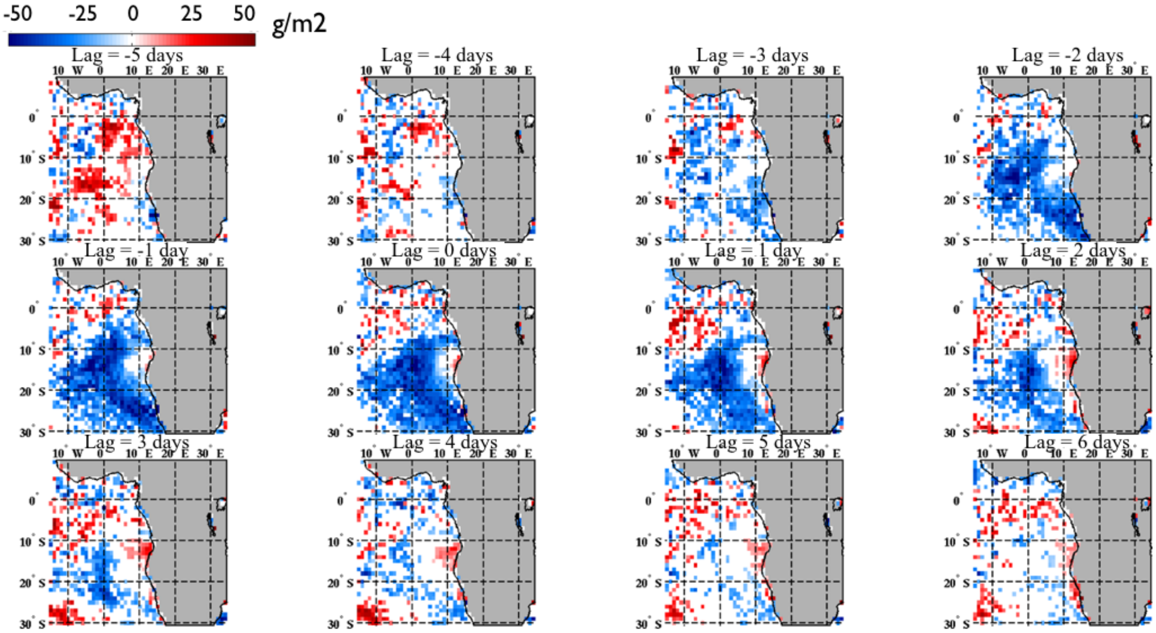

Figure 3.21: Liquid water path ($g/m^2$) for the BBon simulation: difference between composites on the upper 30% of the wind metric minus composites on the lower 30% of the wind metric. Composite differences are plotted (left to right, then up to down) at lag times -6 to +5 days.

3.17 is analogous to fig. 3.18, except that a 3-day running mean of low cloud fraction within the box is plotted instead of CCN. Low cloud fraction exhibits much larger temporal variability than zonal flow so it is helpful to consider the strength of their relationship with some smoothing applied to the cloud field. This correlation value is R = 0.28, a respectable value in the context of how difficult it is to construct simple proxies for cloud variables. To put this into context, the first principal component of the low cloud fraction field only explains 10% of the low cloud fraction variance in the BBon simulation, and previous authors have considered correlation coefficients of INSERT to be adequate. Without the 3-day running mean, R = 0.20 at lag + 1 for low cloud and the flow metric (fig. 3.20). Taken together, the correlations between the flow metric and CCN and low cloud fraction were considered adequate to proceed with composite analysis.

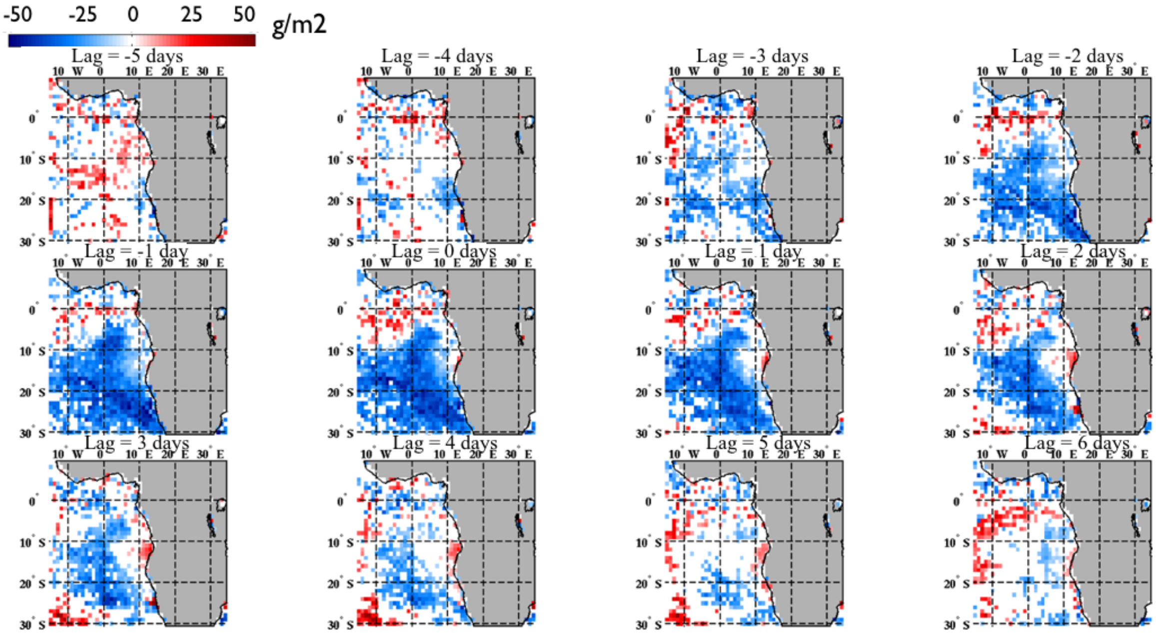

Figure 3.22: Liquid water path ($g/m^2$) for the BBoff simulation: difference between composites on the upper 30% of the wind metric minus composites on the lower 30% of the wind metric. Composite differences are plotted (left to right, then up to down) at lag times -6 to +5 days.

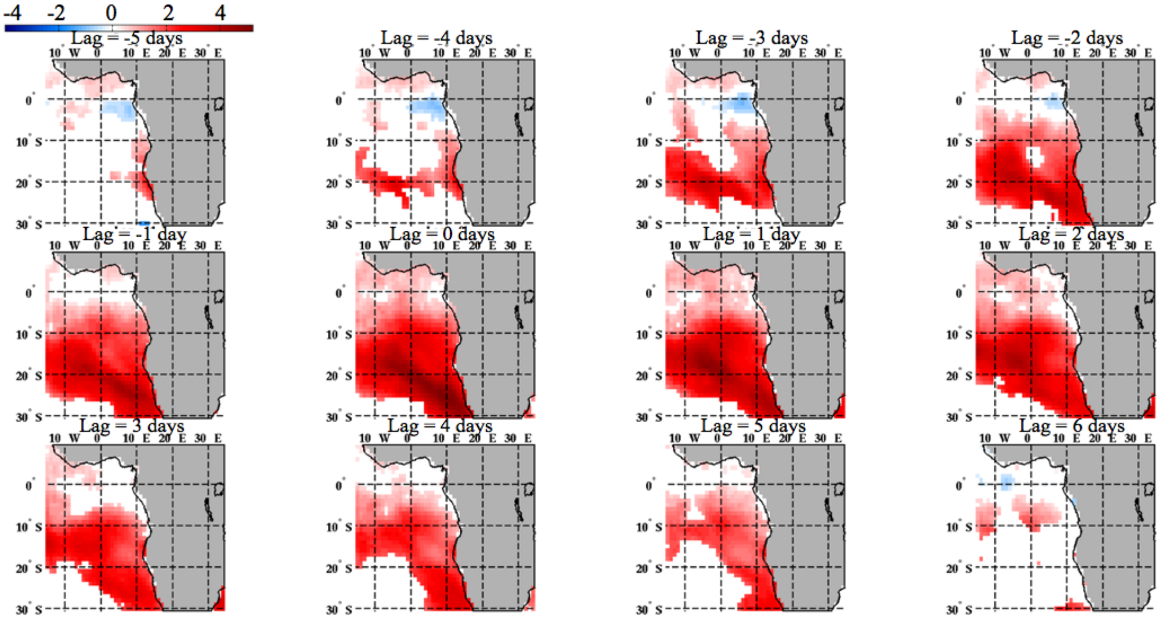

Figure 3.23: Lower tropospheric stability (K) for the BBonsimulation: difference between composites on the upper 30% of the wind metric minus composites on the lower 30% of the wind metric. Composite differences are plotted (left to right, then up to down) at lag times -6 to +5 days.

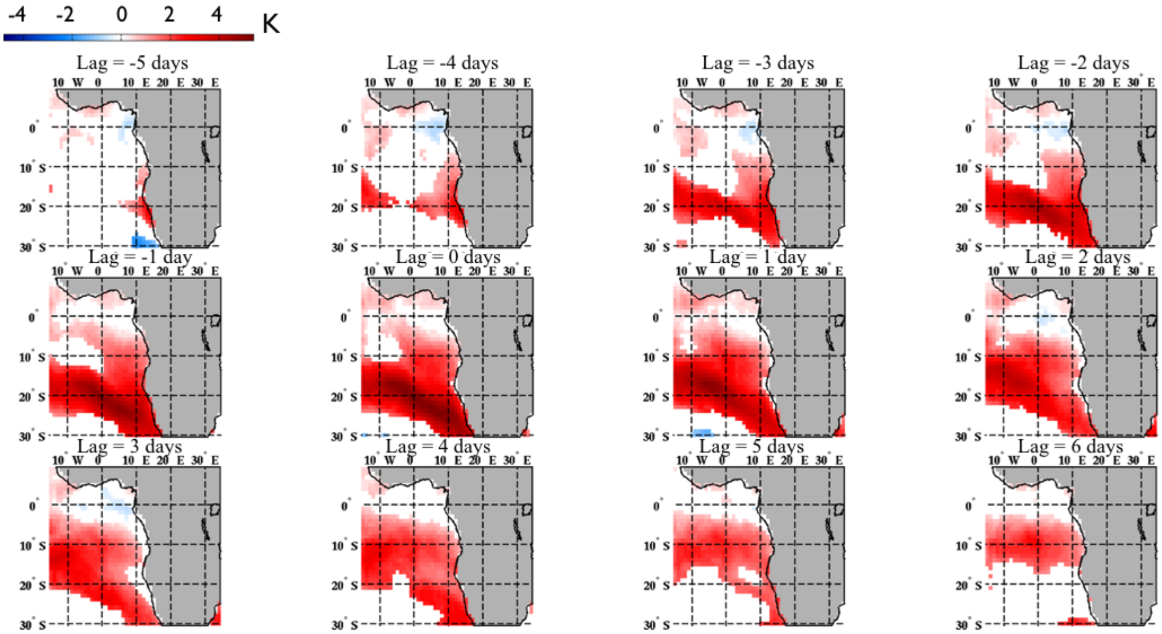

Figure 3.24: Lower tropospheric stability (K) for the BBoff simulation: difference between composites on the upper 30% of the wind metric minus composites on the lower 30% of the wind metric. Composite differences are plotted (left to right, then up to down) at lag times -6 to +5 days.

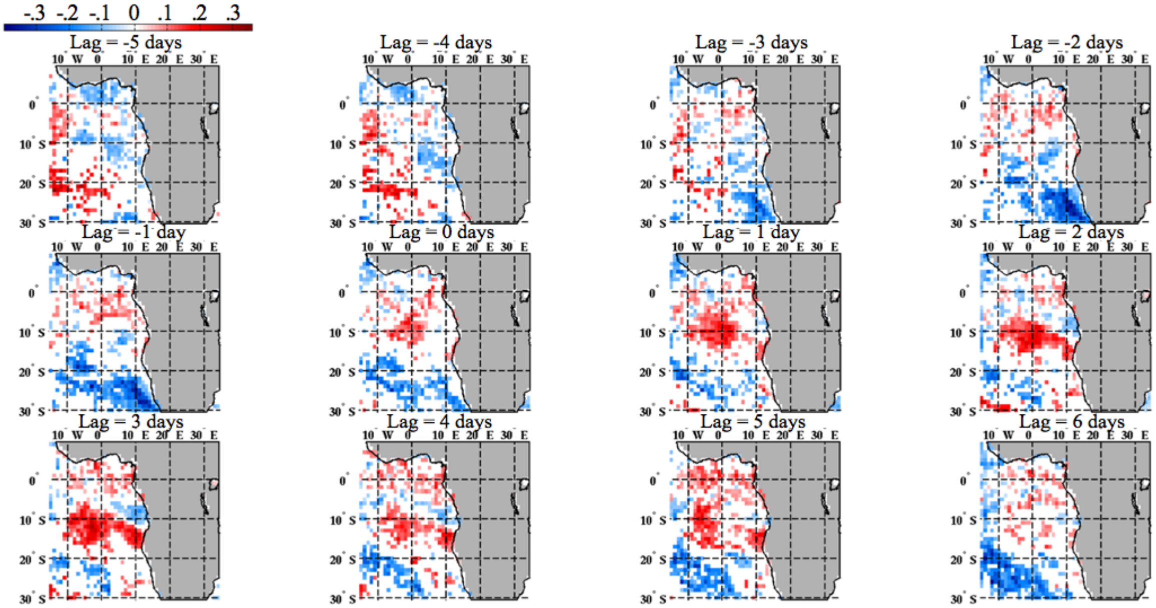

Figure 3.25: Low cloud frequency for the BBon simulation: difference between composites on the upper 30% of the wind metric minus composites on the lower 30% of the wind metric. Composite differences are plotted (left to right, then up to down) at lag times -6 to +5 days.

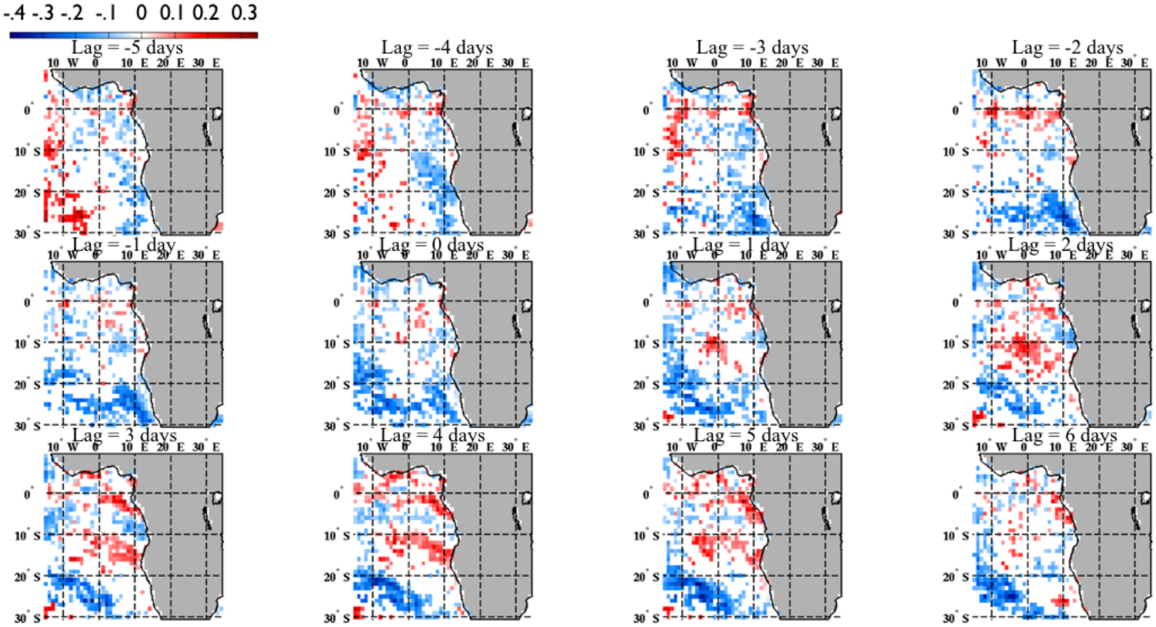

Figure 3.26: Low cloud frequency for the BBoff simulation: difference between composites on the upper 30% of the wind metric minus composites on the lower 30% of the wind metric. Composite differences are plotted (left to right, then up to down) at lag times -6 to +5 days.

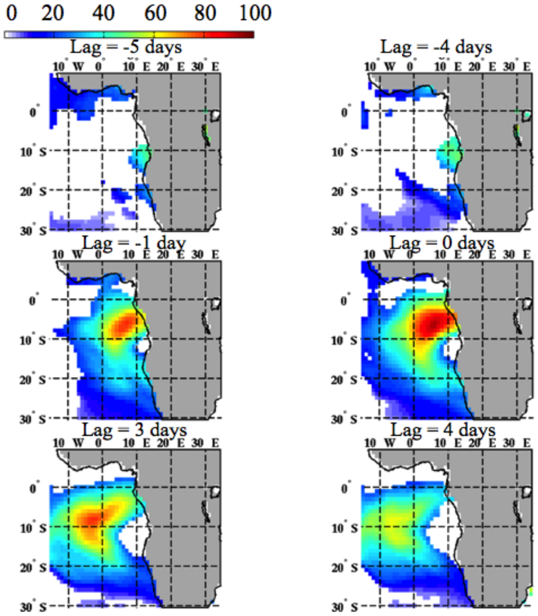

Figure 3.27: 4 km CCN (at $S = 0.2$, $\text{cm}^{-3}$) for the BBon simulation: difference between composites on the upper 30% of the wind metric minus composites on the lower 30% of the wind metric. Composite differences are plotted (left to right, then up to down) at lag times -6 to +5 days.

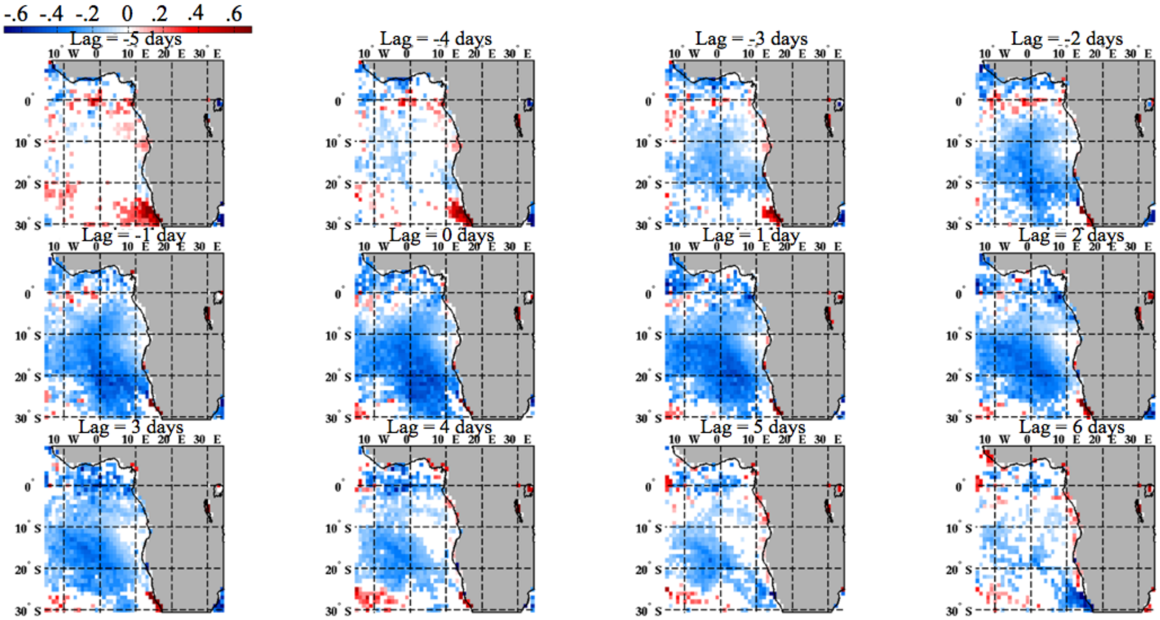

Figure 3.28: 4 km CCN (at $S = 0.2$, $\mathrm{cm}^{-3}$) for the BBoff simulation: difference between composites on the upper 30% of the wind metric minus composites on the lower 30% of the wind metric. Composite differences are plotted (left to right, then up to down) at lag times -6 to +5 days.

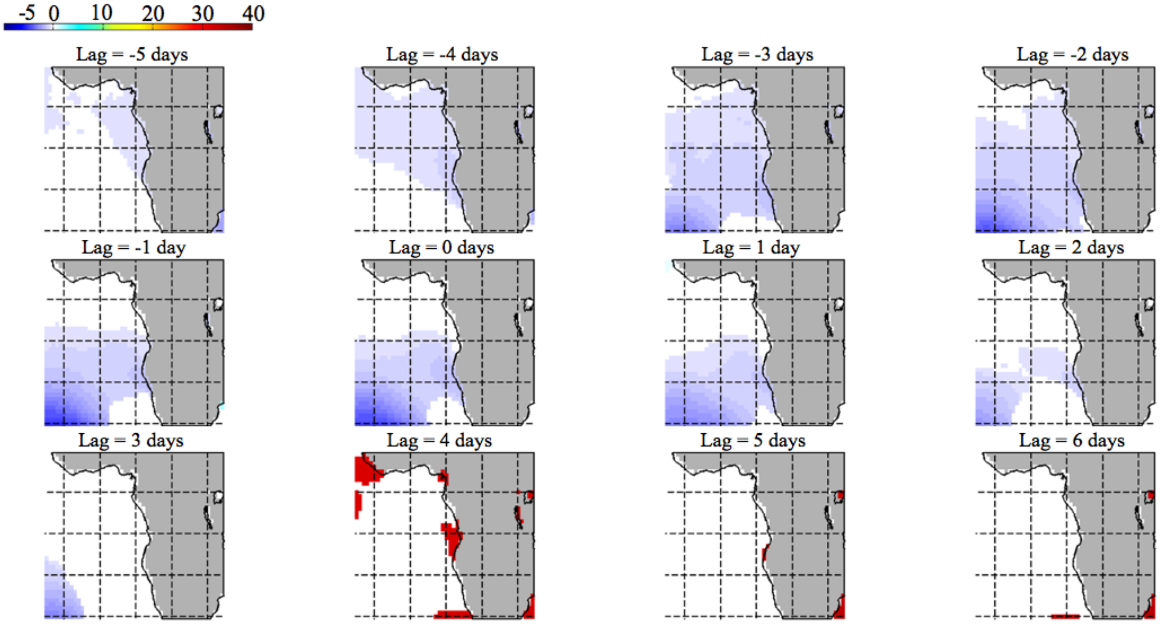

Figure 3.29: Sea level pressure (hPa) for the BBoff simulation: difference between composites on the upper 30% of the wind metric minus composites on the lower 30% of the wind metric. Composite differences are plotted (left to right, then up to down) at lag times -6 to +5 days.

Composites of meteorological variables on the wind metric demonstrate the metrics ability to represent synoptic-scale meteorological variability. First, 70th and 30th percentiles are computed for the flow metric. Then, days when the flow metric exceeds the 70th percentile or falls below the 30th percentile are used to select co-incident fields of meteorological, aerosol, and cloud fields which represent the upper and lower ends of the flow distribution, respectively. Composites are computed of these upper and lower populations and differences (upper - lower) are shown at lag times from -5 to +6 days to illustrate the differences in the field associated with the meteorological cycle represented by the flow metric. The range of lags is chosen to capture the full extent of an aerosol transport event (e.g. fig. For the large-scale meteorological fields, no significance tests are applied because we simply wish to show the synoptic setup associated with the wind metric. For other fields, 1-sigma significance is enforced, which is considered preliminary pending several more years worth of simulations to allow for the degree of autocorrelation present in most fields.

Strong easterly flow is associated with a 20-80m strengthening of the subtropical high in the 500hPa height field that precedes the maximal easterly flow by 3 days and continues for +2 days afterwards. The subtropical high aloft also shifts eastwards towards the continent, a result supported by observations (P.Zuidema, personal comm.). Stronger easterly winds, stronger northerly winds over the continent, and stronger southerly winds off the coast at these same lag times indicate a strengthening of cyclonic flow associated with the subtropical high. At the surface, sea level pressure response to the offshore flow metric is characterized by 3-5 hPa lower pressure at lag times -3 to +2 days (fig. 3.29), which is associated with weaker anticyclonic flow.

The strengthening of the subtropical anticyclonic circulation transports increased quantities of aerosols off the western coast, as expected from the timeseries of the flow metric and CCN. Composite differences in the 4km CCN ($S = 0.2\%$) field are shown in fig. 3.27 which illustrates a coherent plume of CCN as it emerges from the continent and wafts westward until it exits the domain. The magnitude of the

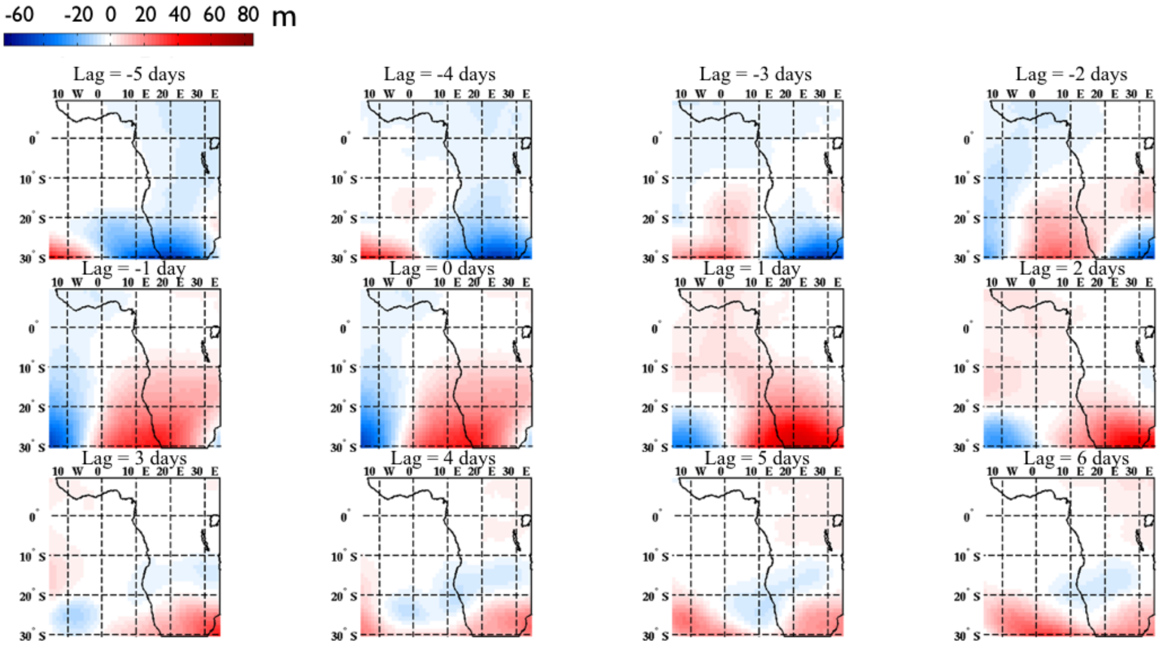

Figure 3.30: 500 hPa geopotential height (km) for the BBon simulation: difference between composites on the upper 30% of the wind metric minus composites on the lower 30% of the wind metric. Composite differences are plotted (left to right, then up to down) at lag times -6 to +5 days.

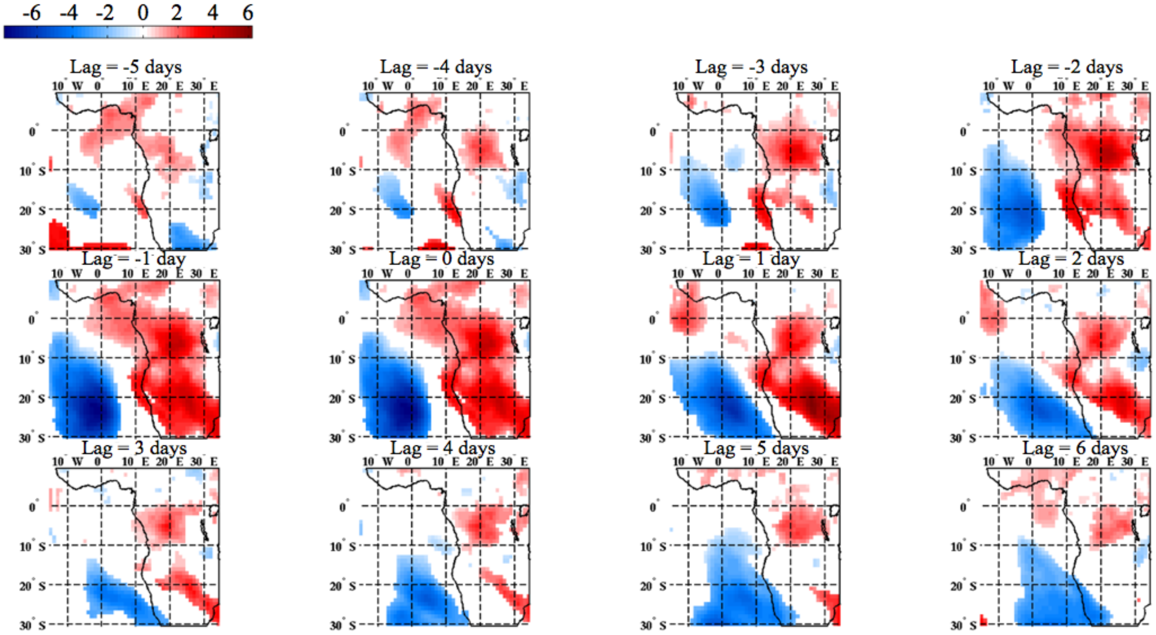

Figure 3.31: 600 hPa meridional wind (m/s) for the BBoff simulation: difference between composites on the upper 30% of the wind metric minus composites on the lower 30% of the wind metric. Composite differences are plotted (left to right, then up to down) at lag times -6 to +5 days.

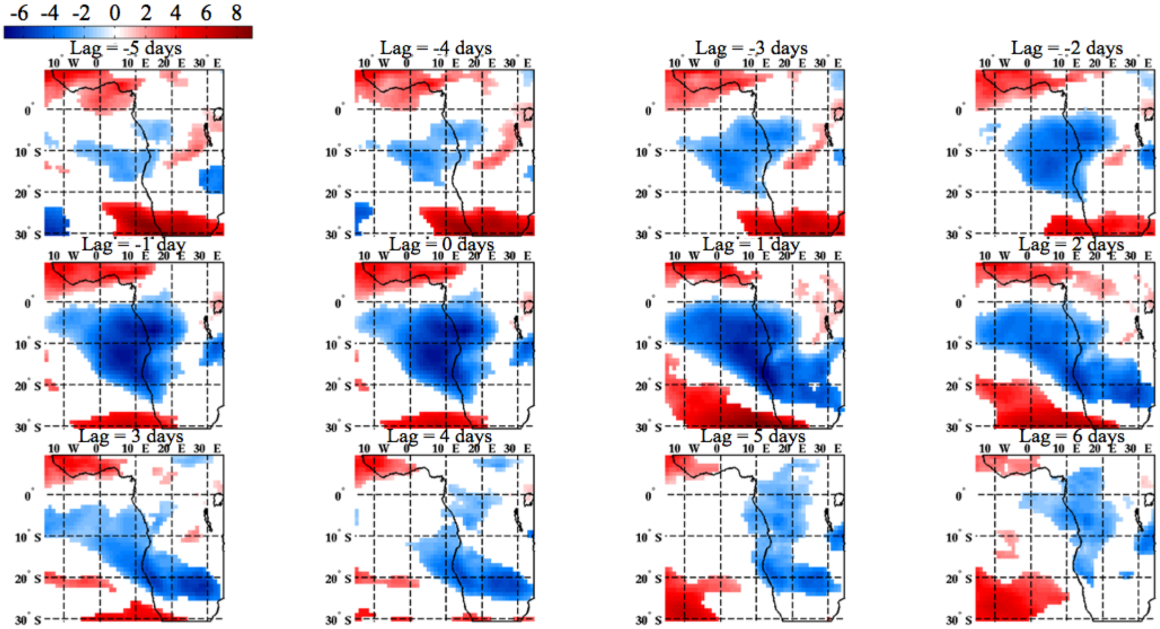

Figure 3.32: 600 hPa zonal wind (m/s) for the BBoff simulation: difference between composites on the upper 30% of the wind metric minus composites on the lower 30% of the wind metric. Composite differences are plotted (left to right, then up to down) at lag times -6 to +5 days.

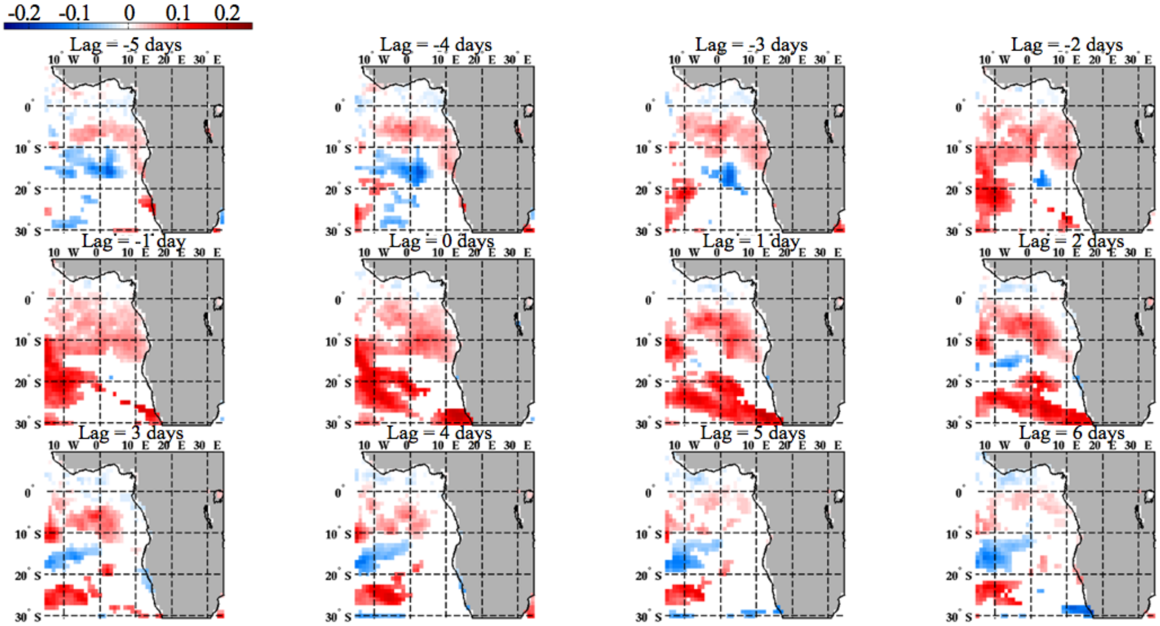

Lag = -5 days
Lag = -4 days
Lag = -3 days
Lag = -2 days
Lag = -1 day
Lag = 0 days
Lag = 1 day
Lag = 2 days
Lag = 3 days
Lag = 4 days
Lag = 5 days
Lag = 6 days

Figure 3.33: 800 hPa potential temperature advection (K/hr) for the BBon simulation: difference between composites on the upper 30% of the wind metric minus composites on the lower 30% of the wind metric. Composite differences are plotted (left to right, then up to down) at lag times -6 to +5 days.

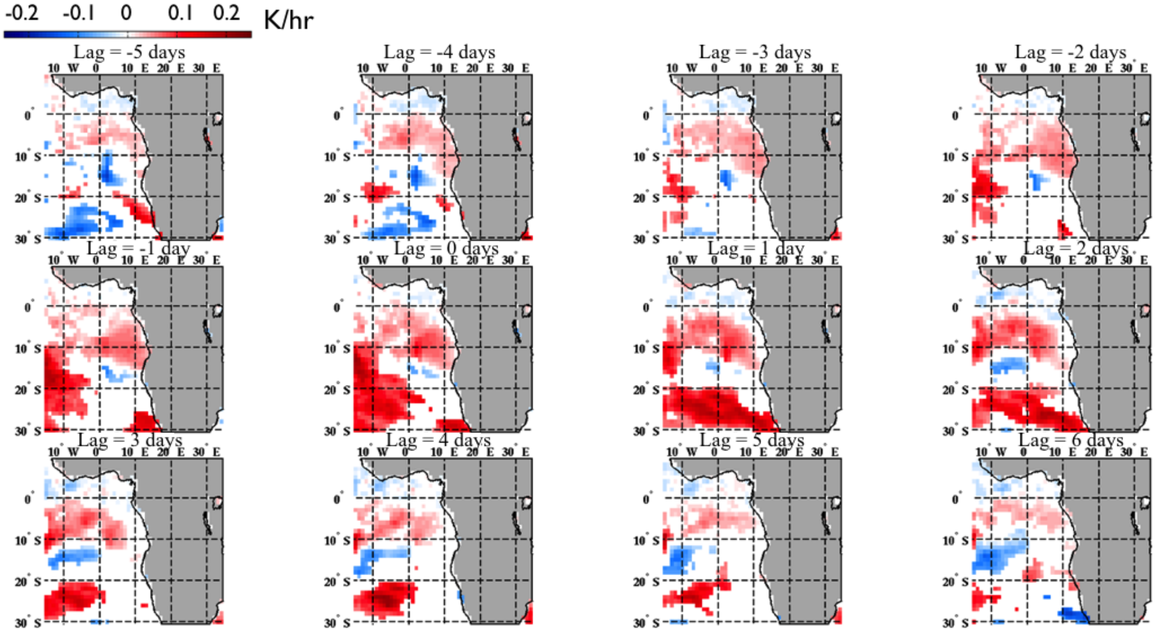

Figure 3.34: 800 hPa potential temperature advection (K/hr) for the BBoff simulation: difference between composites on the upper 30% of the wind metric minus composites on the lower 30% of the wind metric. Composite differences are plotted (left to right, then up to down) at lag times -6 to +5 days.

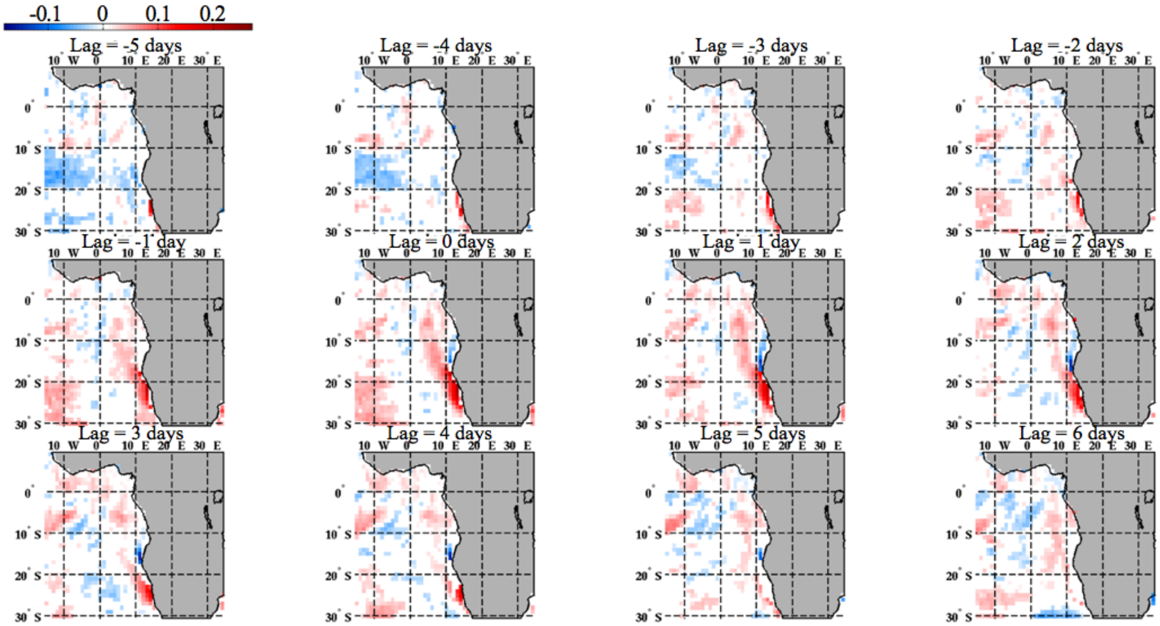

Figure 3.35: 1000 hPa potential temperature advection (K/hr) for the BBoff simulation: difference between composites on the upper 30% of the wind metric minus composites on the lower 30% of the wind metric. Composite differences are plotted (left to right, then up to down) at lag times -6 to +5 days.

composite differences within BBon are comparable to the maximum mean difference between the the BBon and BBoff simulations, and the composite difference over the ocean exceeds the mean difference BBon - BBoff. This means that differences in fields of BBon composited on the flow metric are reflecting differences due to both aerosols and the large-scale meteorology. However, differences in the same fields of BBoff composited in the same way represent the response to the (same) large-scale meteorological pattern with a much smaller aerosol influence(fig. 3.28). By comparing composites drawn from BBon and BBoff data, we can make quantitative estimates of the relative influences from aerosols and meteorology.

### *3.2.2 Cloud/Lower Tropospheric response to meteorological flow metric*

The strengthening of the subtropical high pressure aloft and intensification of offshore easterly winds occurs against a backdrop of large temperature gradients between the cool marine environment and the hot equatorial continental surfaces. Unsurprisingly, the intensification of the easterly flow is accompanied by significant 0.1-0.2 K/hr increases in potential temperature advection at 800 hPa which is similar in both model simulations (figs. 3.33, 3.34). Near the surface, the potential temperature advection response to the meteorological cycle is neutral to weakly positive in the coastal zone (3.35). The influence of the synoptic cycle on potential temperature advection can be seen in the vertical profile of potential temperature calculated over the subregion 2.5-12.5°S-8.5°E-15.5°W which shows substantial warming associated with the meteorological cycle for both BBon and BBoff of 1.8K and 2.4K, respectively, at 820 hPa (fig. 3.36). Consequently, the lower tropospheric stability is 2-4 K larger during peak offshore flow for both the BBon and BBoff simulations (figs. 3.23,3.24).

The wind-driven changes in lower tropospheric stability are reflected in significant increases in the low cloud fraction present in both simulations. Low cloud fraction at lag times 0 to +5 days after an easterly transport event is greater by 0.3 - 0.4 for the BBon simulation (fig. 3.25). For the BBoff case, low cloud fraction increases 0.2 - 0.3

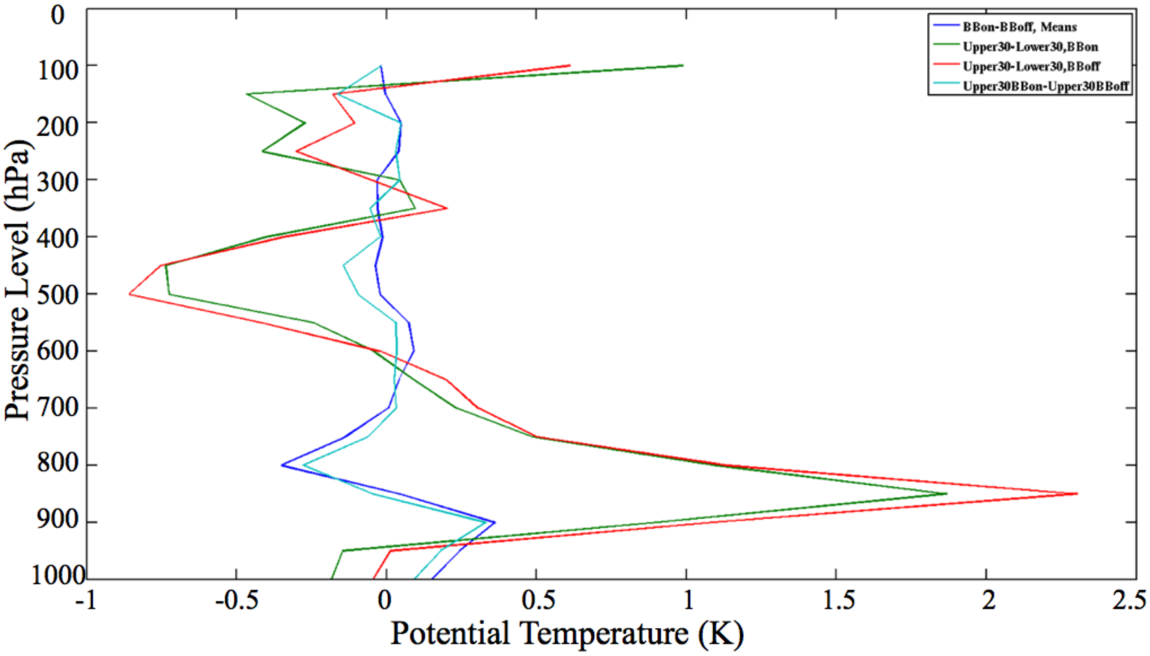

Figure 3.36: Potential temperature, vertical profiles in the region 12.5°S-2.5°S, 8.5°E-15.5°W. Four quantities are shown: 1. difference between mean BBon and mean BBoff; 2. difference between composites on the upper 30% of the wind metric minus composites on the lower 30% of the wind metric for BBon; 3. difference between composites on the upper 30% of the wind metric minus composites on the lower 30% of the wind metric for BBoff; 4. difference between composites on the upper 30% of the wind metric for BBon minus composites on the upper 30% of the wind metric for BBoff.

in the same area for lags +1 to +4 days over a smaller area (fig. 3.26). To put these responses in context, we showed earlier that the low cloud fraction decreases by 0.10 - 0.15 in response to aerosols (fig. 3.8). The increase in low cloud fraction associated with variability in the synoptic high are similar in magnitude to the increased cloud fraction observed in the presence of absorbing aerosols ([108]). These results suggest a possible confounding influence of warm air advection on lower tropospheric stability during periods of high aerosol loading.

Liquid water path also demonstrated a strong, but opposite sign, response to the synoptic cycle relative to aerosol-driven responses. LWP decreases strongly in the days before and after peak easterly flow for both the BBon (fig. 3.21) and BBoff (fig. 3.22) simulations. LWP is lower by 20-30 g m-2 over a broad region of the tropical S.E. Atlantic Ocean for both simulations. The similarity in the LWP response to the flow metric between the models suggests it is mainly associated with meteorological variability. This difference is about twice as large and opposite sign as the mean difference between BBon and BBoff that we presume is due mainly to aerosol variability (3.2). The cloud liquid water path response is explored in more detail for the subregion 2.5 ° S - 18.5 ° S, 8.5 ° E - 15.5 ° E.

As the liquid water path decreases, effective droplet radius decreases by 3-5 microns for both simulations, with larger changes occurring south of 10°S and east of the prime meridian (figs. 3.37, 3.38). These Re changes are larger but of the same sign as those associated with aerosols alone (fig. 3.4), although the spatial pattern is focused further south and seem to be driven by the strong reductions in liquid water availability. The apparently strong influence of liquid water path on effective radius during variations in the synoptic cycle may lead to overestimates of cloud albedo susceptibility to aerosols in the observational data.

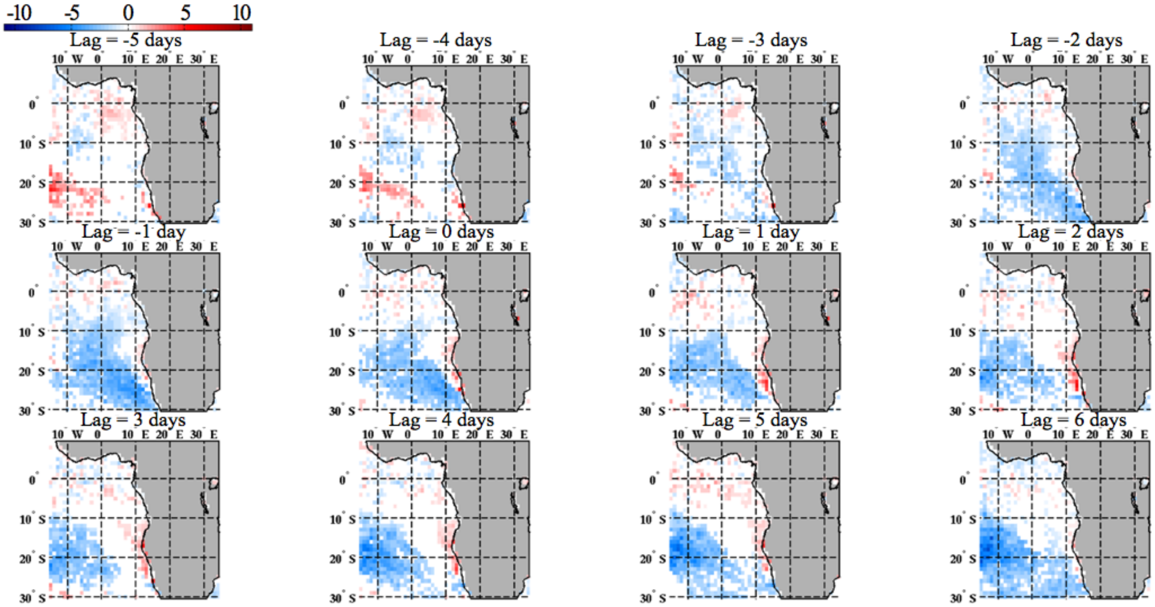

Figure 3.37: Vertical mean cloud droplet effective radius ($\mu m$) for the BBon simulation: difference between composites on the upper 30% of the wind metric minus composites on the lower 30% of the wind metric. Composite differences are plotted (left to right, then up to down) at lag times -6 to +5 days.

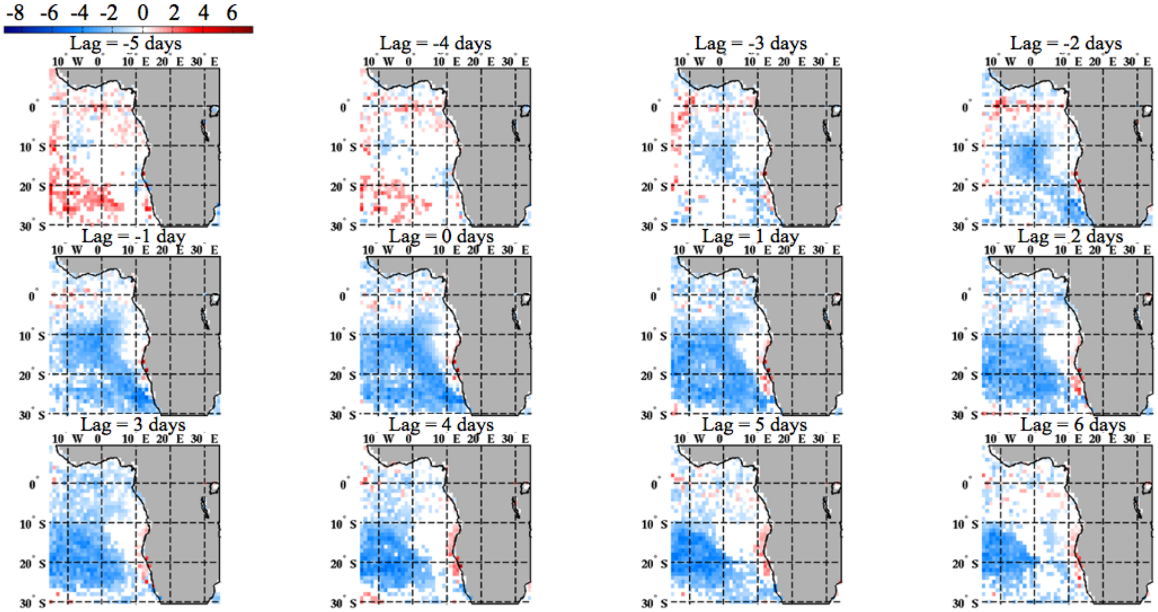

Lag = -5 days

Lag = -4 days

Lag = -3 days

Lag = -2 days

Lag = -1 day

Lag = 0 days

Lag = 1 day

Lag = 2 days

Lag = 3 days

Lag = 4 days

Lag = 5 days

Lag = 6 days

Figure 3.38: Vertical mean cloud droplet effective radius ($\mu m$) for the BBoff simulation: difference between composites on the upper 30% of the wind metric minus composites on the lower 30% of the wind metric. Composite differences are plotted (left to right, then up to down) at lag times -6 to +5 days.

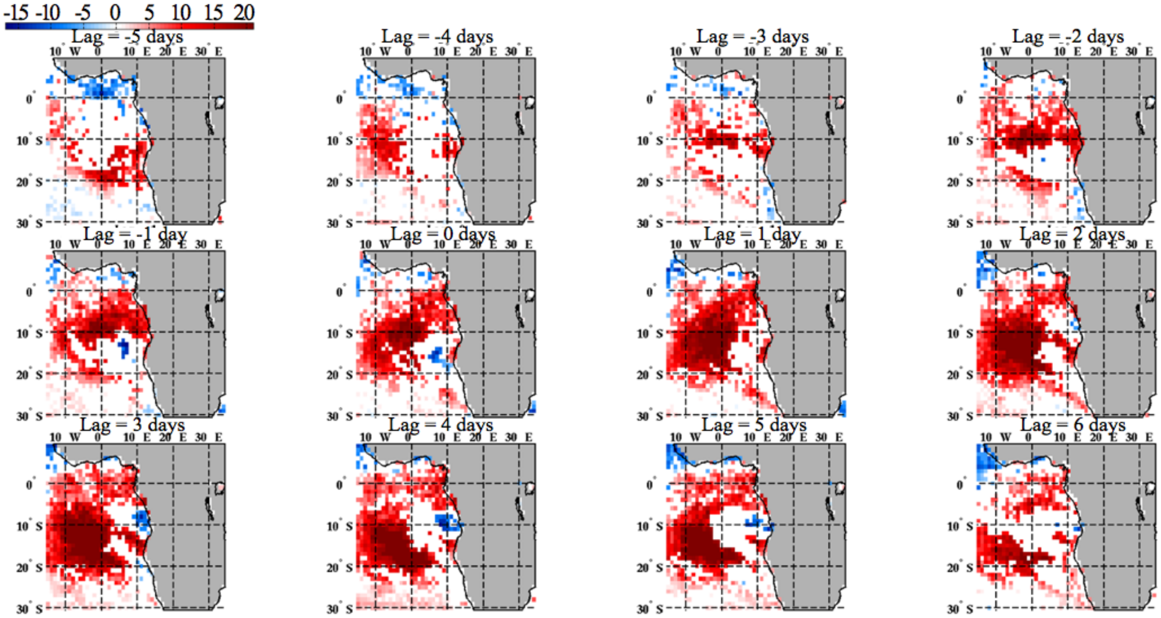

Figure 3.39: Frequency of aerosol layers above clouds for the BBon simulation: difference between composites on the upper 30% of the wind metric minus composites on the lower 30% of the wind metric. Composite differences are plotted (left to right, then up to down) at lag times -6 to +5 days.

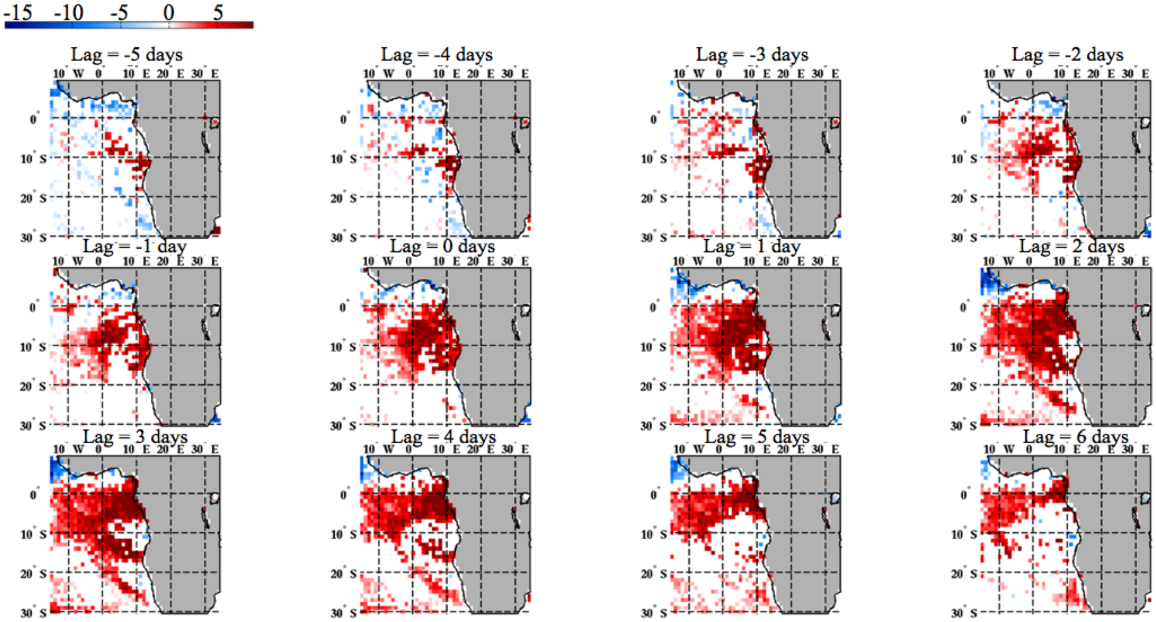

Figure 3.40: Frequency of aerosol layers above clouds for the BBoff simulation: difference between composites on the upper 30% of the wind metric minus composites on the lower 30% of the wind metric. Composite differences are plotted (left to right, then up to down) at lag times -6 to +5 days.

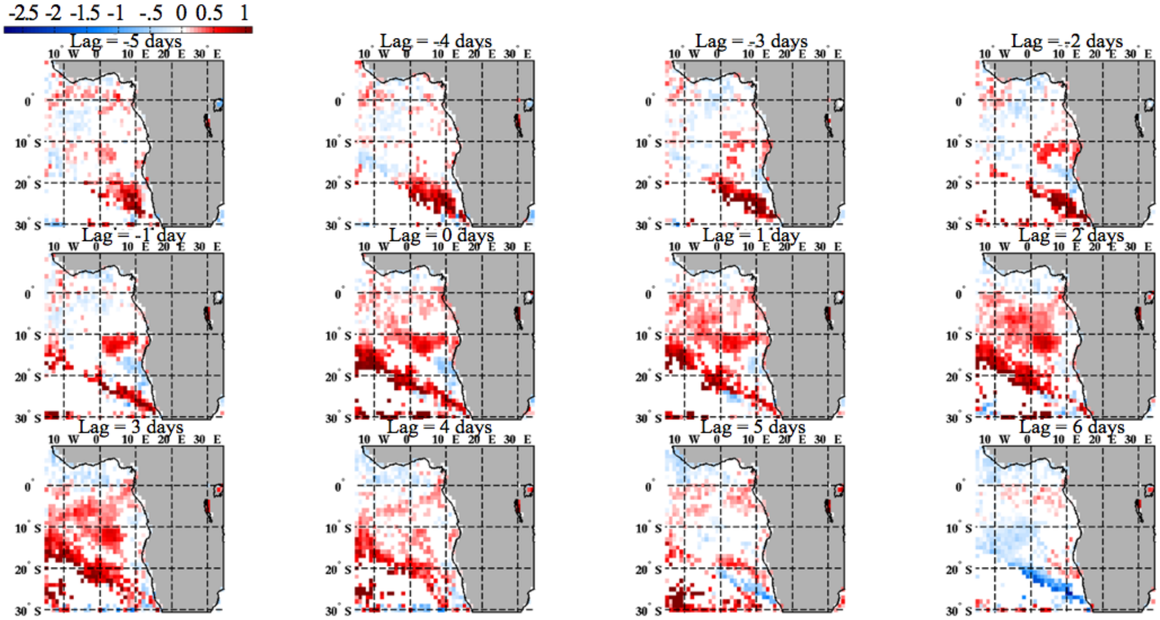

Figure 3.41: Base altitude of aerosol layers above clouds (km) for the BBon simulation: difference between composites on the upper 30% of the wind metric minus composites on the lower 30% of the wind metric. Composite differences are plotted (left to right, then up to down) at lag times -6 to +5 days.

### *3.2.3 Aerosol Layer(s) response to meteorological flow metric*

The response of the aerosol layer variables to the flow metric are consistent with the mean differences between BBon and BBoff, and with the CCN pattern associated with easterly flow. Figs. 3.39 and 3.40 show the differences in the frequency of aerosol layer above cloud (ALAC) occurrence between the upper 30% and lower 30% of the easterly flow metric for BBon and BBoff, respectively. Unsurprisingly, the patterns of ALAC frequency resemble the progression of CCN for both simulations; BBon had 10-20% more frequent ALAC during peak easterly flow while BBoff had 5-10% more frequent ALAC at these times.

The altitude of the base of the aerosol layer above clouds is an important measure of the potential for aerosol-modulated cloud microphysical responses. Figs. 3.41 and 3.42 show the response of the base height of ALAC to the synoptic pattern represented

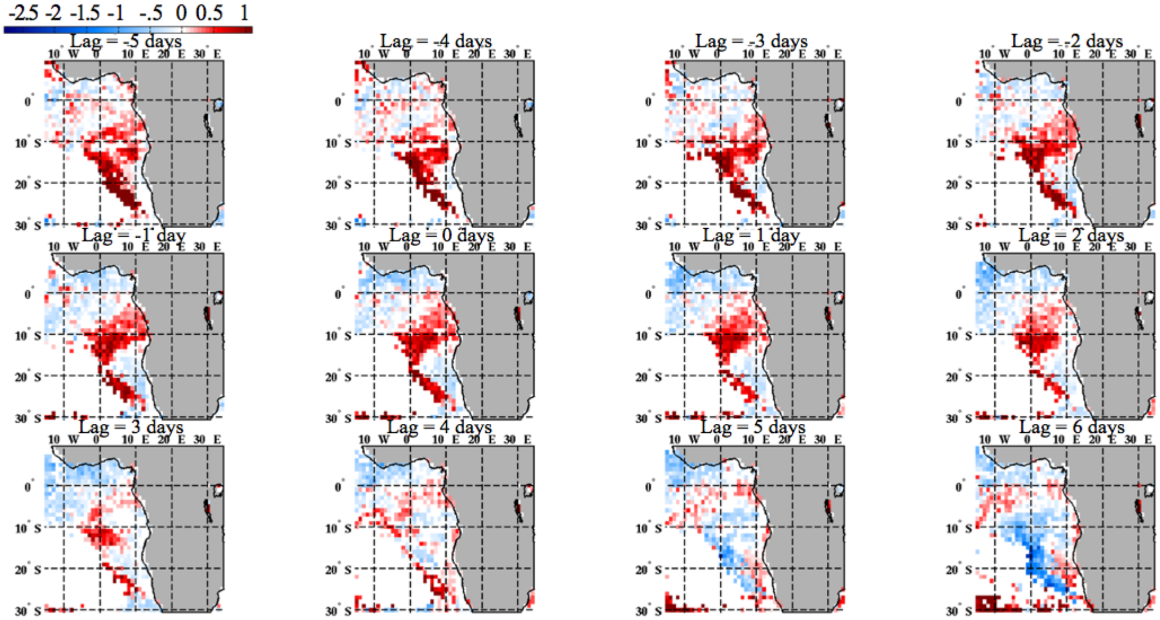

Figure 3.42: Base altitude of aerosol layers above clouds (km) for the BBoff simulation: difference between composites on the upper 30% of the wind metric minus composites on the lower 30% of the wind metric. Composite differences are plotted (left to right, then up to down) at lag times -6 to +5 days.

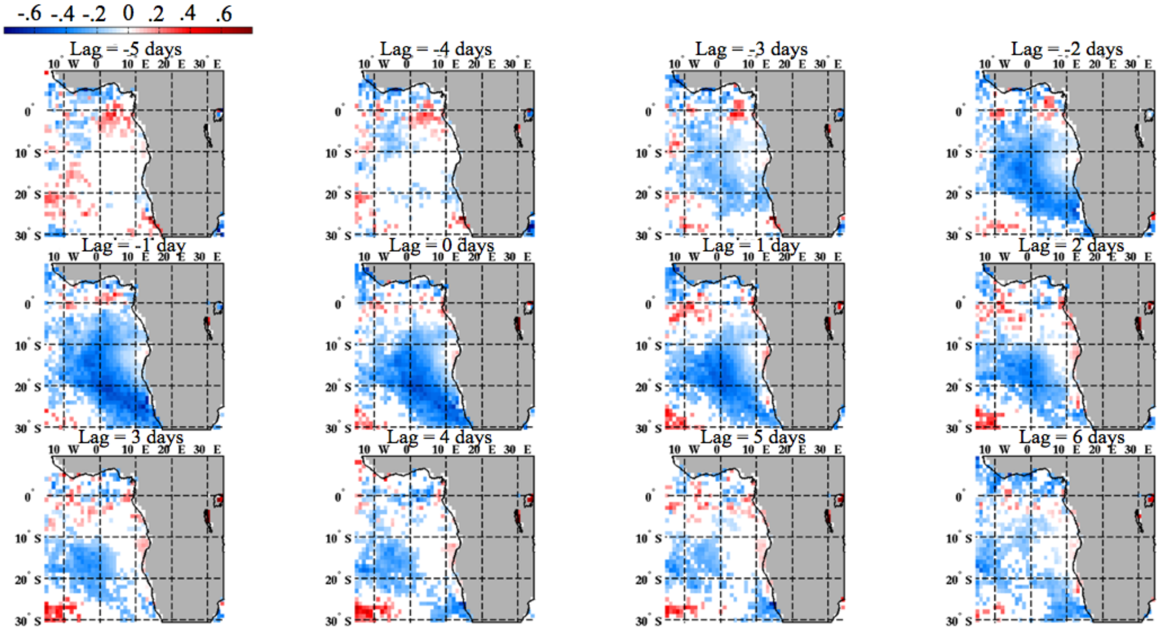

Figure 3.43: Cloud top height (km) for the BBon simulation: difference between composites on the upper 30% of the wind metric minus composites on the lower 30% of the wind metric. Composite differences are plotted (left to right, then up to down) at lag times -6 to +5 days.

by the easterly wind metric. For both BBon and BBoff the base of the aerosol layer above cloud is elevated 0.5-1km during peak easterly flow. The area of elevated ALAC base is more widespread in BBon and more consequential as it has these layers much more frequently. But whatever is driving the relative lifting of the aerosol layers away from the cloud deck is related to the meteorology and happens in both simulations. In fact these changes associated with the wind metric are larger or comparable to the mean difference in BBon-BBoff (fig. 3.14), presumably associated mainly with aerosols.

Recall that in the mean differences between BBon and BBoff, the vertical separation between aerosol layers and their underlying clouds in BBon was 100-300 m higher than in BBoff (fig. 3.15). The response of the vertical separation to the meteorological metric is also positive, and ranges from 200-600 m (figs. 3.45,3.46). BBon

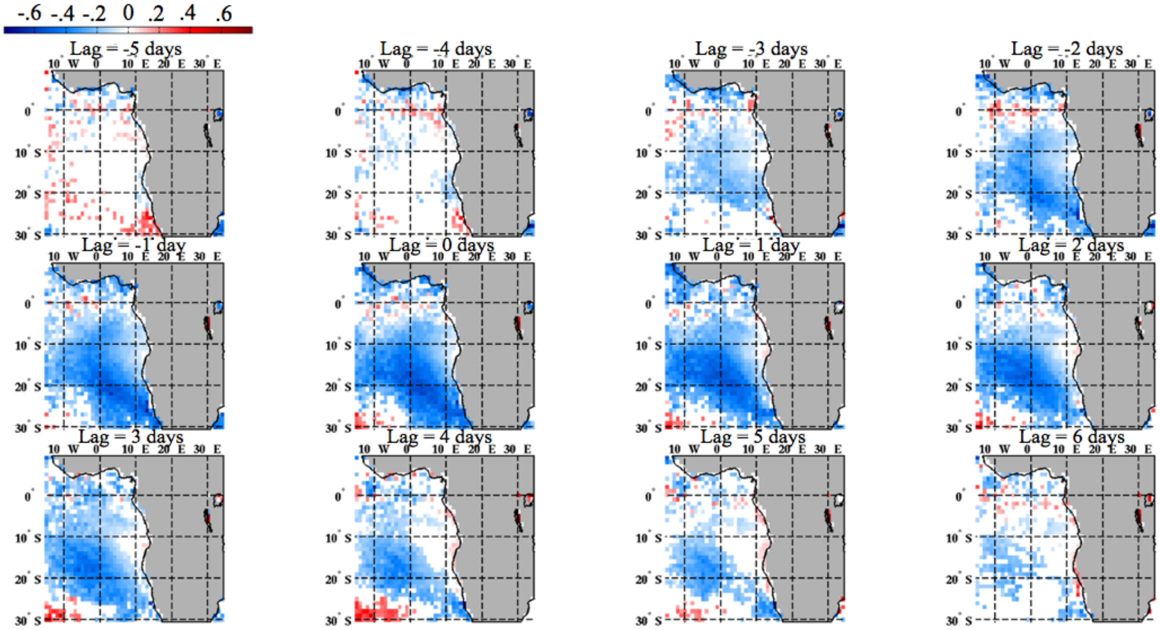

Lag = -5 days

Lag = -4 days

Lag = -3 days

Lag = -2 days

Lag = -1 day

Lag = 0 days

Lag = 1 day

Lag = 2 days

Lag = 3 days

Lag = 4 days

Lag = 5 days

Lag = 6 days

Figure 3.44: Cloud top height (km) for the BBoff simulation: difference between composites on the upper 30% of the wind metric minus composites on the lower 30% of the wind metric. Composite differences are plotted (left to right, then up to down) at lag times -6 to +5 days.

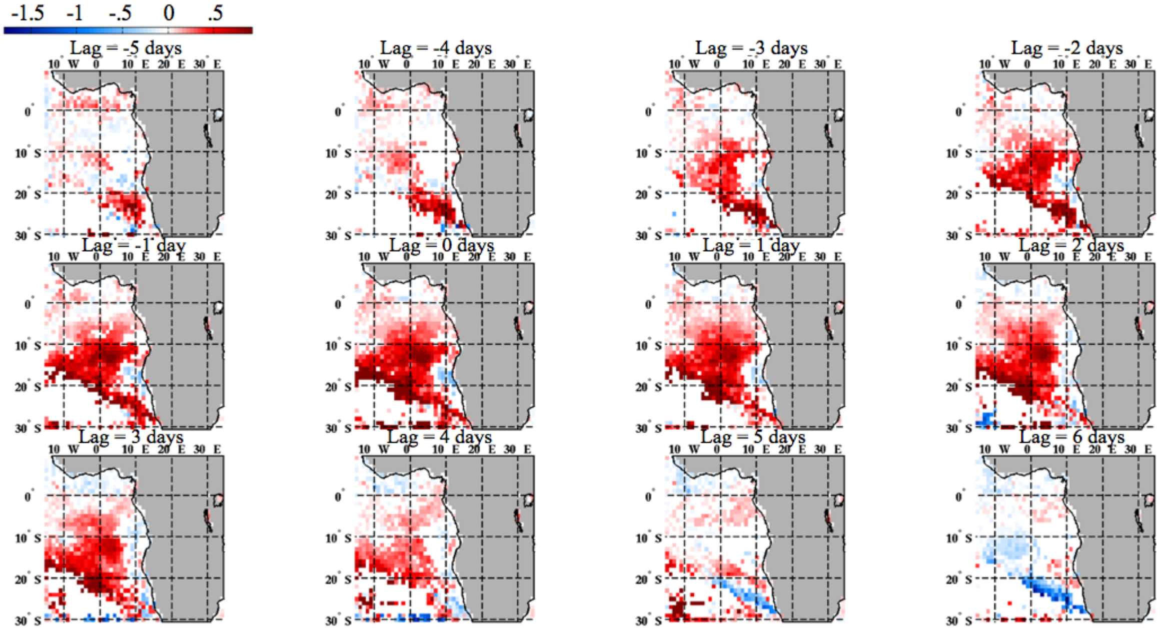

Figure 3.45: Vertical separation between aerosol and cloud layers (km) for the BBon simulation: difference between composites on the upper 30% of the wind metric minus composites on the lower 30% of the wind metric. Composite differences are plotted (left to right, then up to down) at lag times -6 to +5 days.

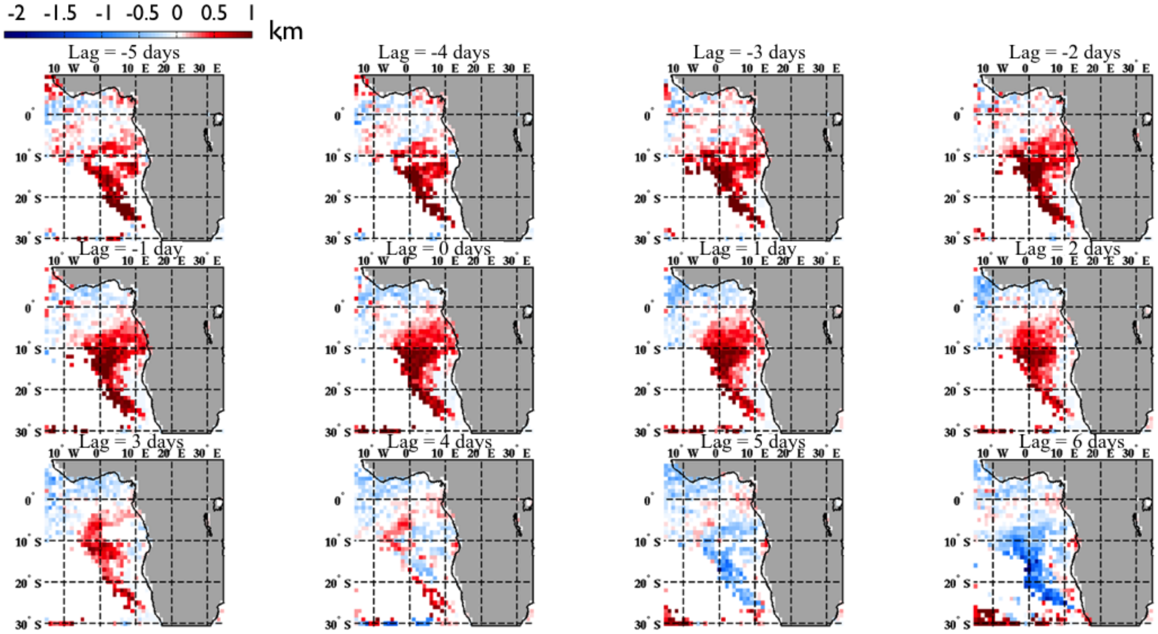

Figure 3.46: Vertical separation between aerosol and cloud layers (km) for the BBoff simulation: difference between composites on the upper 30% of the wind metric minus composites on the lower 30% of the wind metric. Composite differences are plotted (left to right, then up to down) at lag times -6 to +5 days.

and BBoff show a similar response, although again, the response in BBoff is only as important as an indicator that the effect is associated with meteorology since the layers themselves are infrequent. The aerosol layers above clouds are lofted higher as the lag time increases from -4 days to 0 days, and remain high until +5 days after peak easterly flow. The increase in the aerosol - cloud separation occurs as both the aerosol layer is lofted higher (figs. 3.41, 3.42), and the cloud layer sinks lower (figs. 3.43,3.44) as if the cloudy and polluted layers were repulsed like magnets away from one another; that is, the meteorological conditions that favor offshore transport also favor a greater separation between clouds and aerosols. In the mean difference between BBon and BBoff, which were loosely interpreting as aerosol-driven, the clouds and the base of the aerosol layer are **both** higher for BBon vs BBoff, but the distance between them increases due to the aerosol layer lofting further than the cloud layer. So we see increases in the vertical separation associated with the variability in both the aerosols and the meteorology, but in different ways.

## *3.3 Cloud and Aerosol Co-variations in Subregion during Synoptic Cycle*

This research has revealed a complicated set of responses to an enhancement of the subtropical high pressure in the Southeast Atlantic which is represented by the easterly flow metric. Stratocumulus cloud properties, lower tropospheric atmospheric conditions, and aerosol layer geometry have been shown to co-vary in coherent ways as the easterly flow peaks and subsides. In this section, we zoom in on the subregion 2.5 ° S-18.5 ° S, 8.5 ° E-15.5 ° W where aerosol layers often exist above clouds, and where there are significant co-variations among the different properties we have examined. By condensing the map results into simple figures, we can develop a physical understanding of how the system is producing the set of modeled responses.

Figures like fig. 3.48 show a fractional difference in a quantity composited on the synoptic flow metric. Composites are calculated at different lag times, as for the

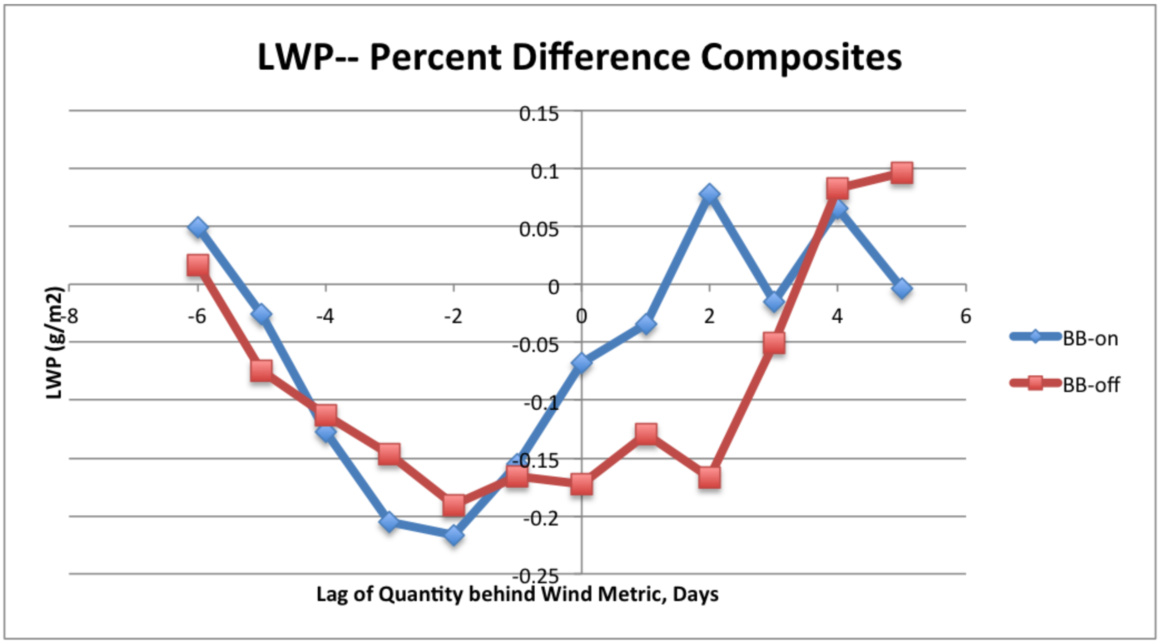

Figure 3.47: Liquid water path (g/$rmm^2$) for BBon and BBoff, averaged over subregion 2.5 ° S - 18.5 ° S, 8.5 ° E - 15.5 ° E. Lines represent the percent difference between composites on the upper 30% of the wind metric minus composites on the lower 30% of the wind metric for each simulation, divided by the composites on the lower 30%. Percent composite differences are plotted (left to right) at lag times -6 to +5 days.

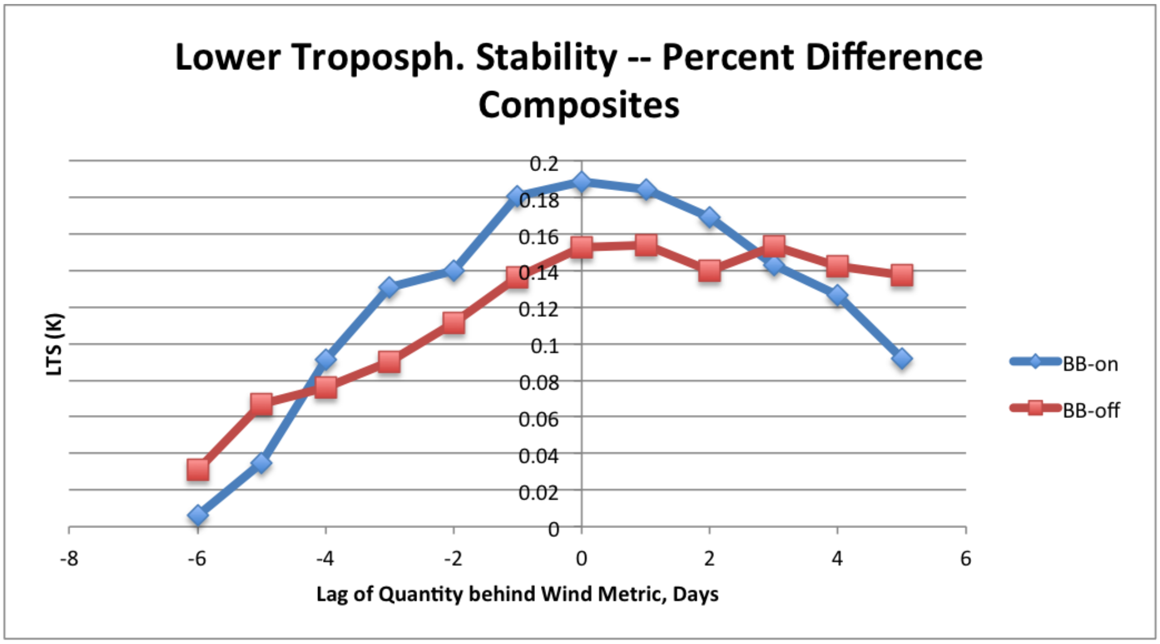

Figure 3.48: Lower tropospheric stability (K) for BBon and BBoff, averaged over subregion 2.5 ° S - 18.5 ° S, 8.5 ° E - 15.5 ° E. Lines represent the percent difference between composites on the upper 30% of the wind metric minus composites on the lower 30% of the wind metric for each simulation, divided by the composites on the lower 30%. Percent composite differences are plotted (left to right) at lag times -6 to +5 days.

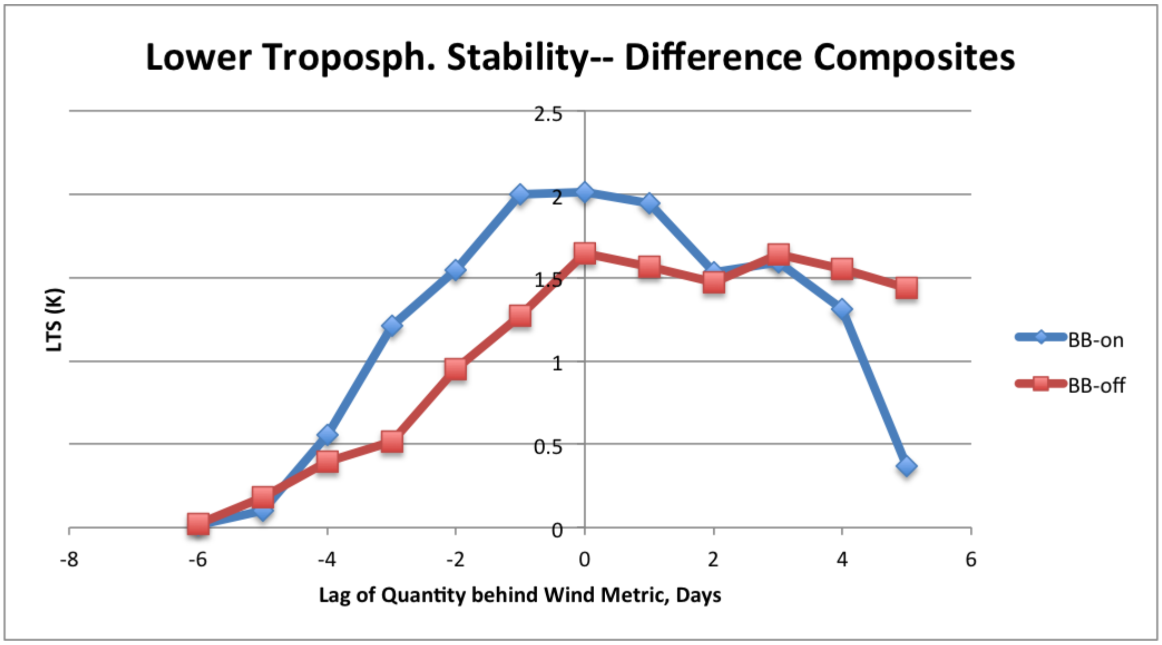

Figure 3.49: Lower tropospheric stability (K) for BBon and BBoff, averaged over subregion 2.5 ° S - 18.5 ° S, 8.5 ° E - 15.5 ° E. Lines represent the difference between composites on the upper 30% of the wind metric minus composites on the lower 30% of the wind metric for each simulation. Composite differences are plotted (left to right) at lag times -6 to +5 days.

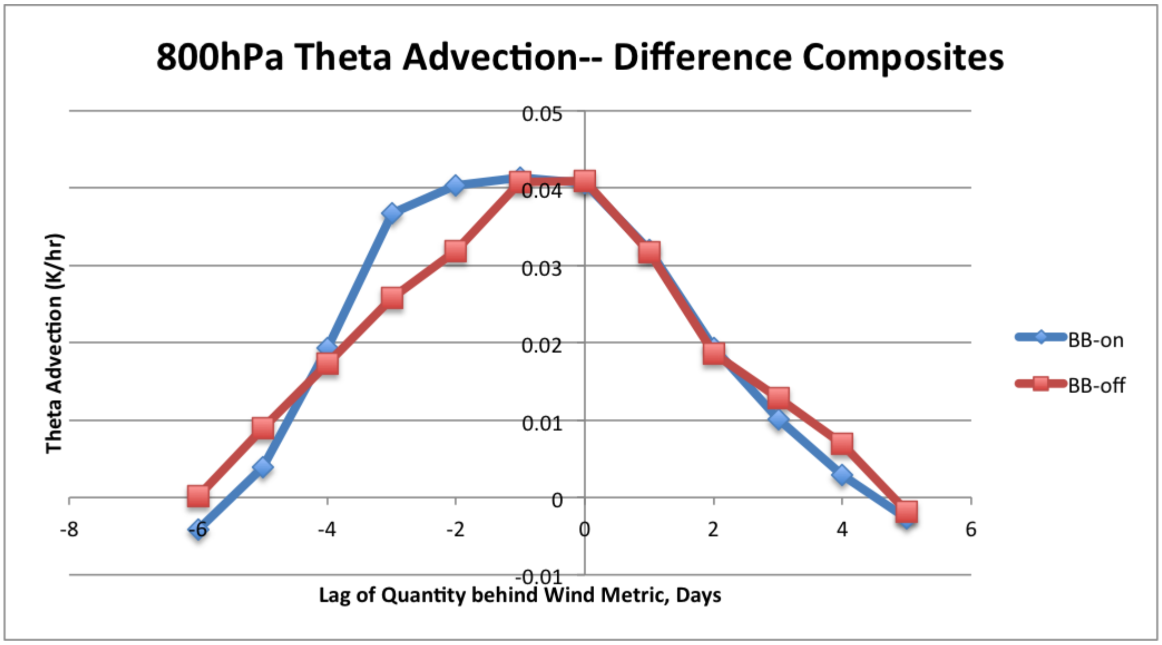

Figure 3.50: Horizontal potential temperature advection at 800 hPa (K) for BBon and BBoff, averaged over subregion 2.5 ° S - 18.5 ° S, 8.5 ° E - 15.5 ° E. Lines represent the difference between composites on the upper 30% of the wind metric minus composites on the lower 30% of the wind metric for each simulation. Composite differences are plotted (left to right) at lag times -6 to +5 days.

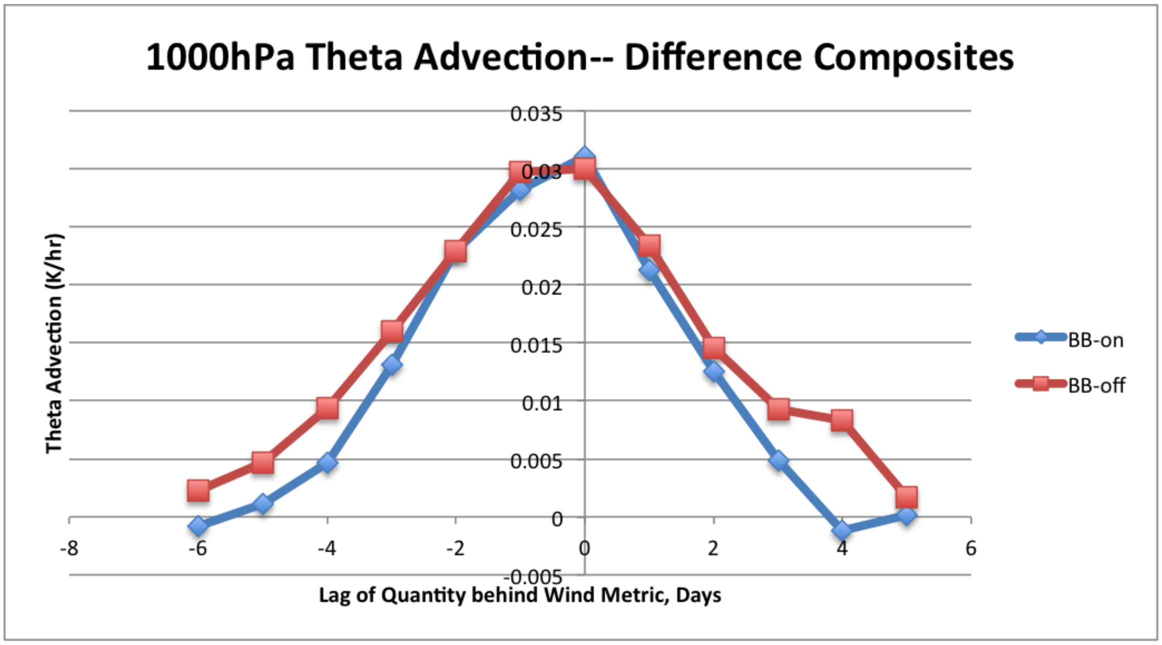

Figure 3.51: Horizontal potential temperature advection at 1000 hPa (K) for BBon and BBoff, averaged over subregion 2.5 ° S - 18.5 ° S, 8.5 ° E - 15.5 ° E. Lines represent the difference between composites on the upper 30% of the wind metric minus composites on the lower 30% of the wind metric for each simulation. Composite differences are plotted (left to right) at lag times -6 to +5 days.

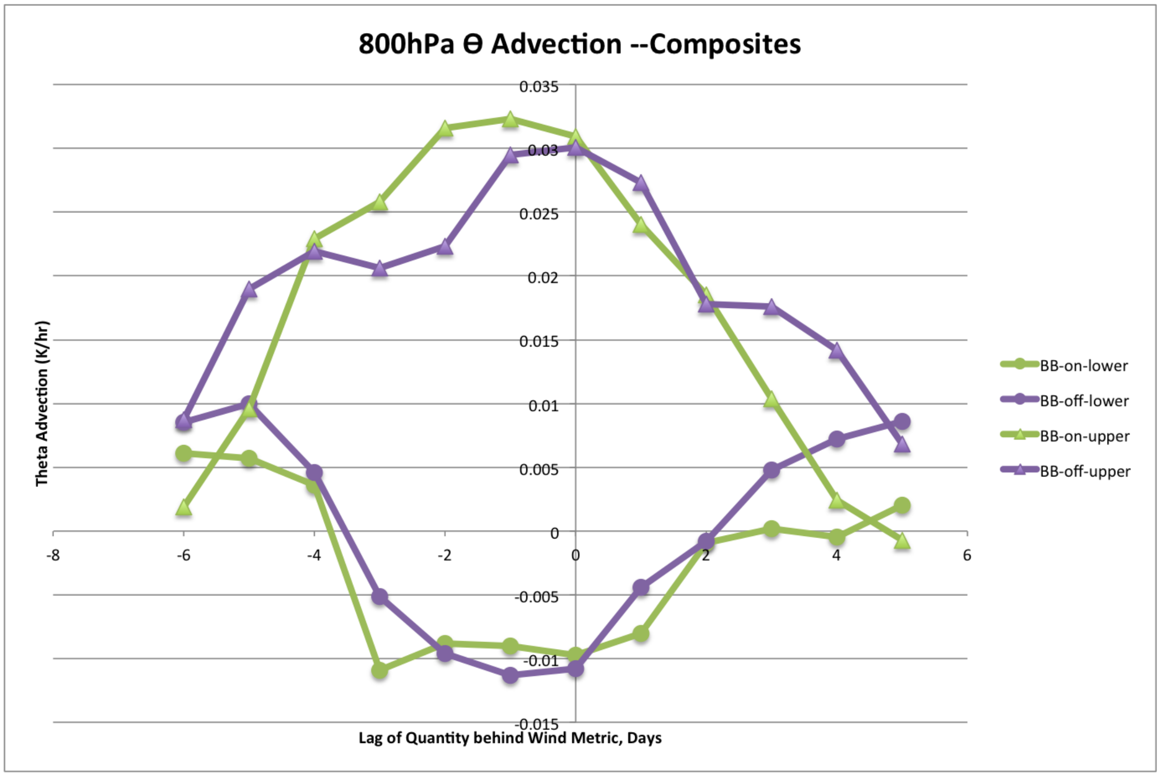

Figure 3.52: Horizontal potential temperature advection at 800 hPa (K) for BBon and BBoff, averaged over subregion 2.5 ° S - 18.5 ° S, 8.5 ° E - 15.5 ° E. Lines represent composite means on the upper 30% of the wind metric and the lower 30% of the wind metric for each simulation. Composites are plotted (left to right) at lag times -6 to +5 days.

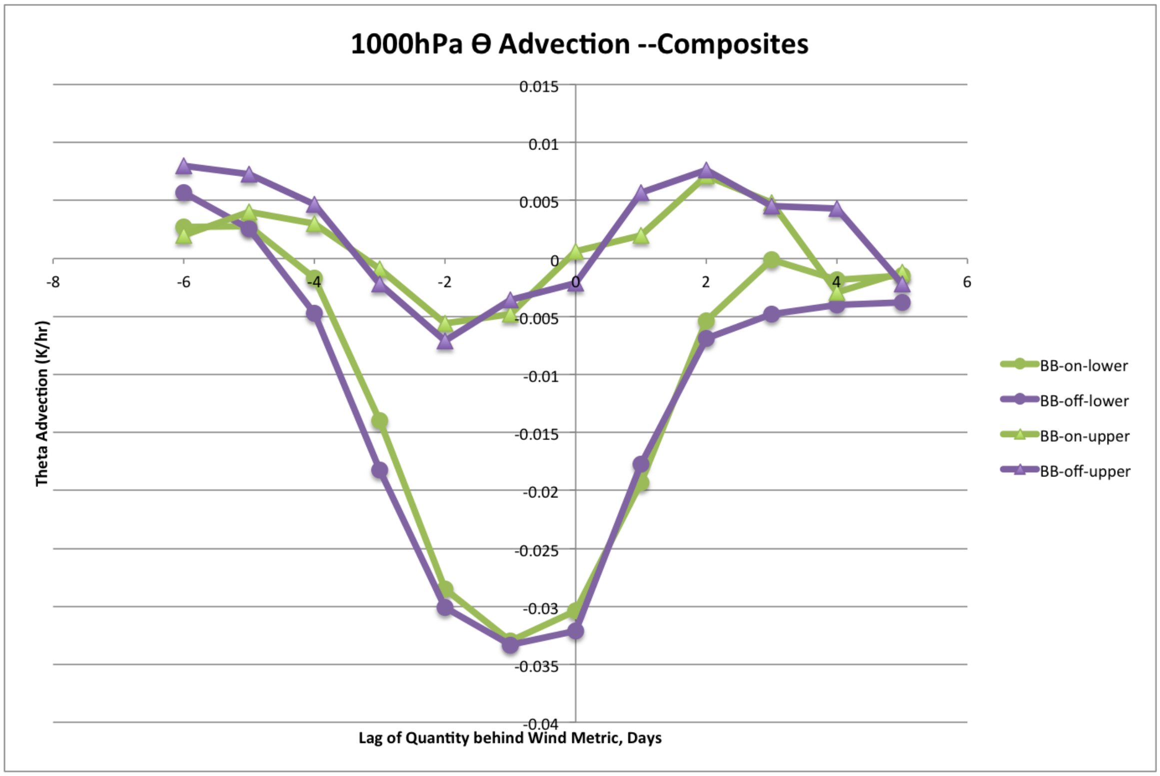

Figure 3.53: Horizontal potential temperature advection at 1000 hPa (K) for BBon and BBoff, averaged over subregion 2.5 ° S - 18.5 ° S, 8.5 ° E - 15.5 ° E. Lines represent composite means on the upper 30% of the wind metric and the lower 30% of the wind metric for each simulation. Composites are plotted (left to right) at lag times -6 to +5 days.

previous figures. Fractional difference is defined as the difference between composites on the upper 30% of flow minus composites on the lower 30% of flow, divided by the composite of the lower 30%. This can be thought of as the fractional increase (or decrease) of a quantity during stronger easterly flow relative to weaker easterly (or westerly) flow. Analogous figures are made for the differences, and for the upper 30% composites, and the lower 30% composites. The quantity is averaged over the subregion 2.5 ° S - 18.5 ° S, 8.5 ° E - 15.5 ° E to reduce noise and focus on the area of coincident clouds and aerosols.

Lower tropospheric stability is very similar between the upper 30% and lower 30% early in the meteorological cycle, but the differences increase approaching lag-time zero where the LTS is 2.0K (1.6K) greater for stronger easterly wind situations for BBon (BBoff) (fig. 3.49). As the aerosol plume moves offshore and the easterlies subside, the differences in LTS decline to 0.2K for BBon but remain elevated at 1.5K for BBoff. The lagged signal in in lower tropospheric stability seems to be driven by changes in the potential temperature advection at 800hPa and 1000hPa, as was shown previously. Composite differences of potential temperature advection in the subregion rises from zero at lag -6 days to a peak of 0.04 K/hr at lag zero and decrease at subsequent lag times; this signal is very similar for both simulations (fig. 3.50). The signal in the 1000hPa theta advection in the subregion slopes upwards as well, to a value of 0.03K/hr at lag 0, before also descending at later lag times (fig. 3.51). Essentially, there is enhanced warm air advection near the surface and above the PBL during off-shore flow events but the advection aloft is stronger. The advection aloft undergoes a sign change from cold advection (-0.01 K/hr) during weak offshore or onshore flow to substantial warm advection (+0.03 K/hr) during offshore flow events, producing a positive signal (fig. 3.52). Cold air advection exists at the surface regardless of the synoptic cycle as northerly currents bring in cooler air from the extratropics, but this advection weakens during strong off-shore flow events, producing a positive signal (fig. 3.53).

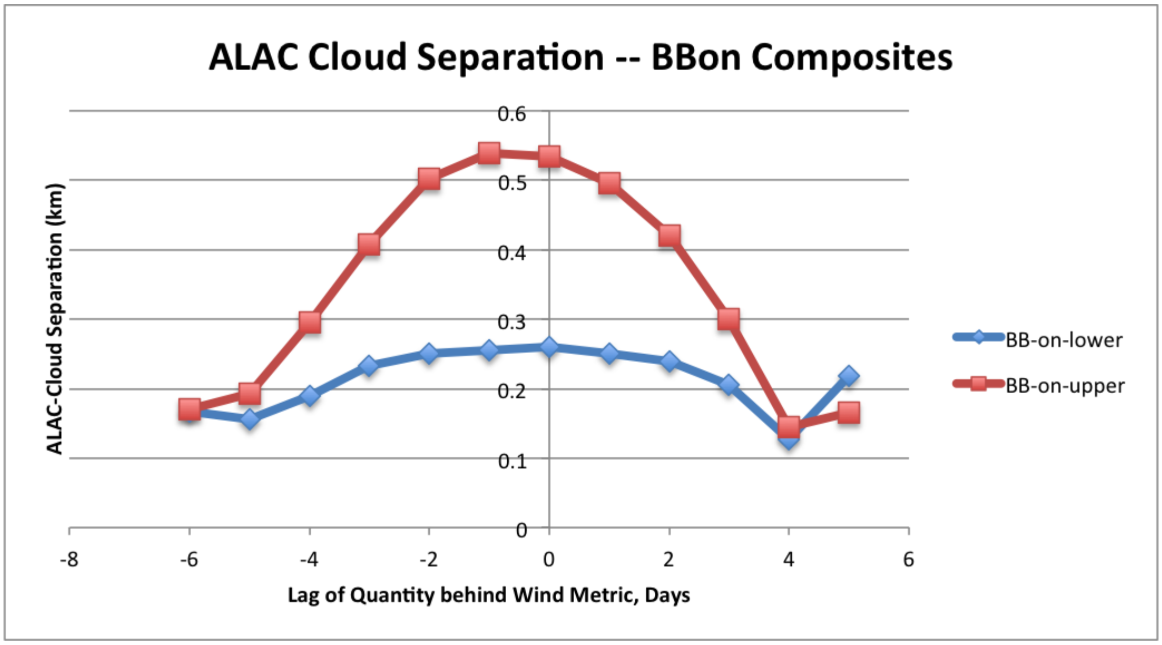

Figure 3.54: Vertical separation between aerosol layer base and cloud top for BBon and BBoff, averaged over subregion 2.5 ° S - 18.5 ° S, 8.5 ° E - 15.5 ° E. Lines represent the percent difference between composites on the upper 30% of the wind metric minus composites on the lower 30% of the wind metric for each simulation, divided by the composites on the lower 30%. Percent composite differences are plotted (left to right) at lag times -6 to +5 days.

Lower tropospheric stability is a strong predictor of low cloud amount ([56]). When LTS is enhanced by 18% during peak easterly flow (fig. 3.48), the low cloud fraction is enhanced 24% for BBon (fig. 3.56). For BBoff, the 16% LTS enhancement (fig. 3.48) gave a 17% boost in the low cloud amount (fig. 3.56). This is a fairly straightforward result, but it is consequential for the reflectance of shortwave radiation and the generation of additional boundary layer turbulence.

Liquid water path in the subregion is significantly smaller during strong offshore flow events. The LWP composite difference decreases during lag times -6 to -2 days, reaching minima of approx. -15 $\frac{g}{m^2}$ before recovering. Marine stratocumulus clouds' liquid water depends on a steady supply of surface moisture ([111]). Sea surface

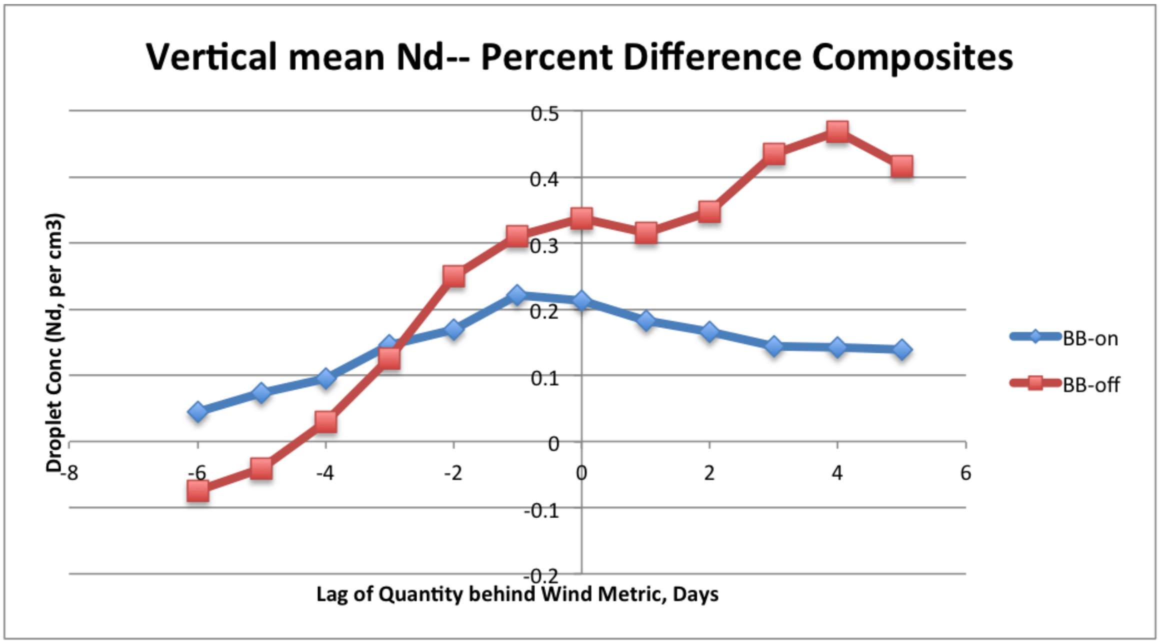

Figure 3.55: Vertically averaged cloud droplet concentration ($cm^{-3}$) for BBon and BBoff, averaged over subregion 2.5 ° S - 18.5 ° S, 8.5 ° E - 15.5 ° E. Lines represent the percent difference between composites on the upper 30% of the wind metric minus composites on the lower 30% of the wind metric for each simulation, divided by the composites on the lower 30%. Percent composite differences are plotted (left to right) at lag times -6 to +5 days.

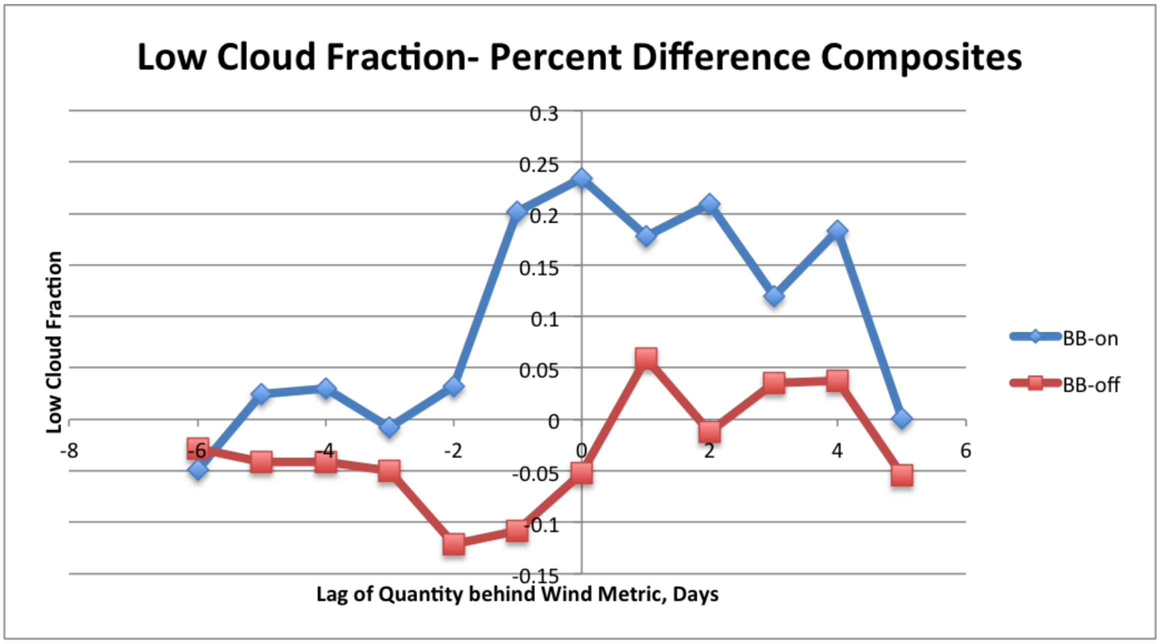

Figure 3.56: Low cloud frequency for BBon and BBoff, averaged over subregion 2.5 ° S - 18.5 ° S, 8.5 ° E - 15.5 ° E. Lines represent the percent difference between composites on the upper 30% of the wind metric minus composites on the lower 30% of the wind metric for each simulation, divided by the composites on the lower 30%. Percent composite differences are plotted (left to right) at lag times -6 to +5 days.

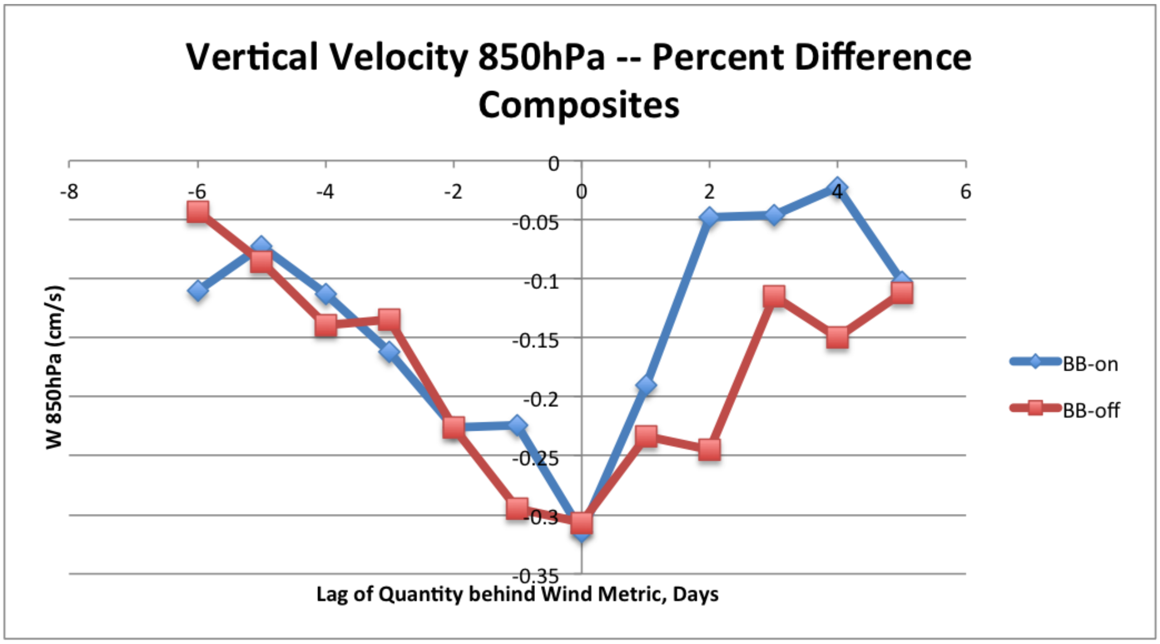

Figure 3.57: Low cloud frequency for BBon and BBoff, averaged over subregion 2.5 ° S - 18.5 ° S, 8.5 ° E - 15.5 ° E. Lines represent the difference between composites on the upper 30% of the wind metric minus composites on the lower 30% of the wind metric for each simulation. Composite differences are plotted (left to right) at lag times -6 to +5 days.

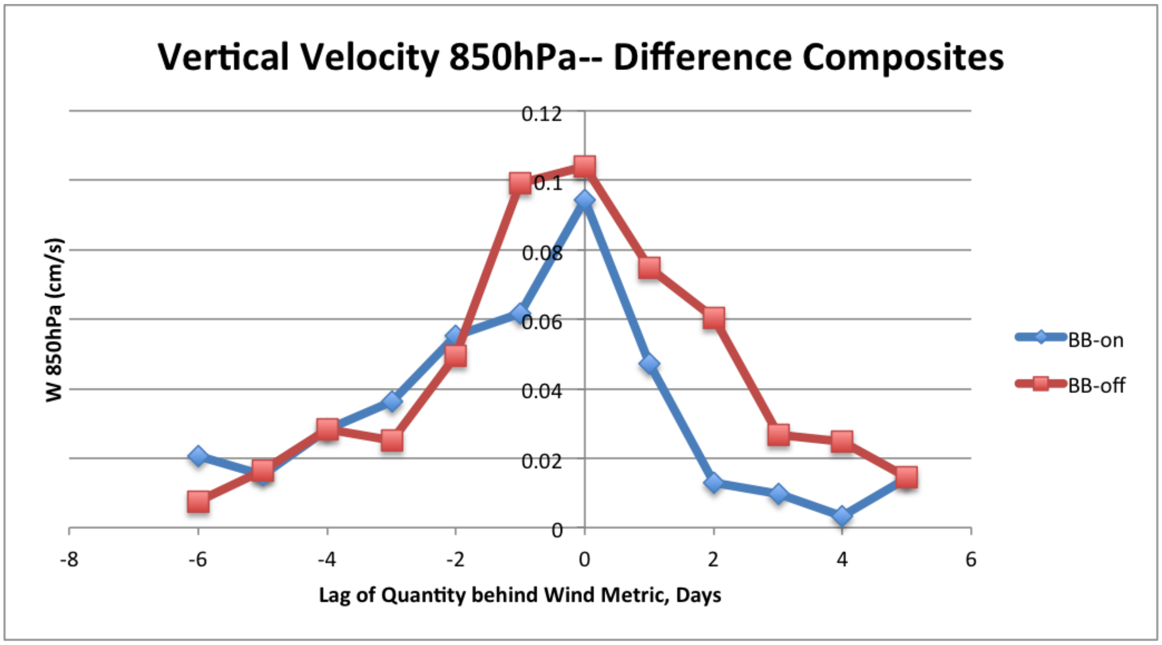

Figure 3.58: Vertical velocity at 850 hPa (cm/s) for BBon and BBoff, averaged over subregion 2.5 ° S - 18.5 ° S, 8.5 ° E - 15.5 ° E. Lines represent the difference between composites on the upper 30% of the wind metric minus composites on the lower 30% of the wind metric for each simulation. Composite differences are plotted (left to right) at lag times -6 to +5 days.

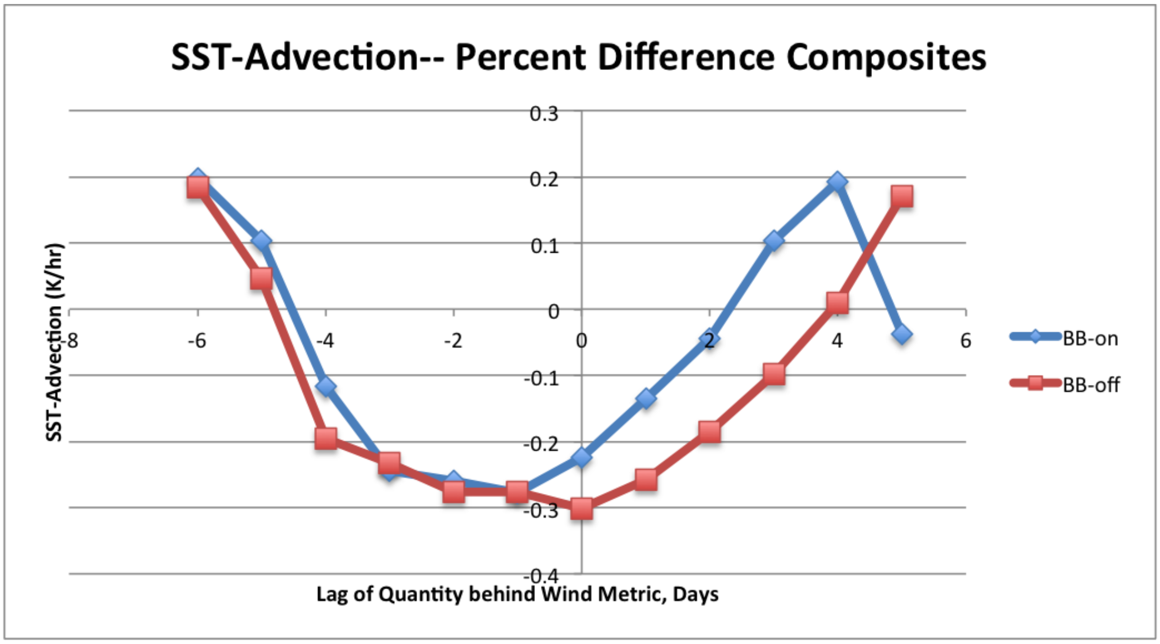

Figure 3.59: Sea-surface temperature advection (K/hr) for BBon and BBoff, averaged over subregion 2.5 ° S - 18.5 ° S, 8.5 ° E - 15.5 ° E. Lines represent the difference between composites on the upper 30% of the wind metric minus composites on the lower 30% of the wind metric for each simulation. Composite differences are plotted (left to right) at lag times -6 to +5 days.

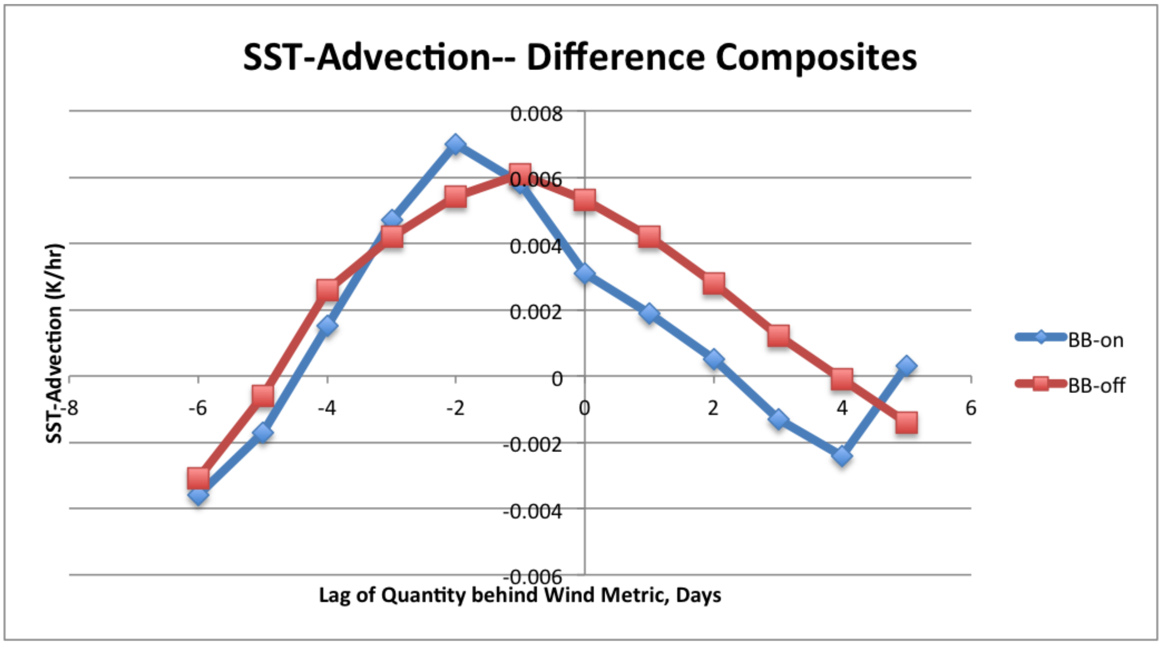

Figure 3.60: Sea-surface temperature advection (K/hr) for BBon and BBoff, averaged over subregion 2.5 ° S - 18.5 ° S, 8.5 ° E - 15.5 ° E. Lines represent the difference between composites on the upper 30% of the wind metric minus composites on the lower 30% of the wind metric for each simulation. Composite differences are plotted (left to right) at lag times -6 to +5 days.

temperature advection reflects the strength of surface moisture fluxes from the ocean to the atmosphere, which in turn supports more clouds. Sea surface temperature advection is negative on average (e.g. cold SST advection) in this subregion which helps stabilize the atmosphere and promotes low cloud formation. This advection is 0.6-0.7 K/hr more positive (e.g. weaker) during peak easterly flow for both BBon and BBoff (fig. 3.60). This is consistent with the signal of reduced wind speed (fig. 3.62) which also reaches minima of -0.6-0.8 m/s minima in the 1-2 days before peak offshore flow. The reduced surface forcing results in a reduced moisture to the boundary layer leading up to peak offshore transport: upward surface moisture flux in the subregion is 0.03-0035 $\frac{kg}{m^2 hr}$ smaller during off-shore flow (fig. 3.61). Weaker winds and upward moisture surface flux result in reduced cloud liquid water path during periods of strong off-shore flow.

The changes in vertical motion above the boundary layer, and turbulence within the boundary layer, help explain the observation that aerosol layers lofted above clouds tend to be higher during transport events, while their underlying clouds tend to be lower. Vertical velocity near the boundary layer top ( 850hPa) is shown in figs. 3.57 (quantities) and 3.58 (percent change). Subsidence is reduced (e.g. more positive values) by 30% during peak transport at lag-zero, and the reduction in subsidence is larger for BBoff in the subsequent days. Weaker subsidence would tend to give a deeper PBLH rather than a shallower one as is observed. It seems that the increase in low cloud cover (3.56) is generating enough turbulence to entirely offset the decrease in PBLH that one might expect from weaker surface stress and reduced subsidence.

Weaker subsidence in the free troposphere allows aerosol layers to remain lofted as the move off-shore, relative to the usual scenario where strong subsidence pushes the aerosol layers downward. At the same time, reduced boundary layer turbulence leads to shallower stratocumulus decks. The net result is that the vertical separation between clouds and aerosols is increased during peak offshore flow. Fig. 3.54 shows the vertical separation for BBon (since BBoff has such infrequent layers); while the

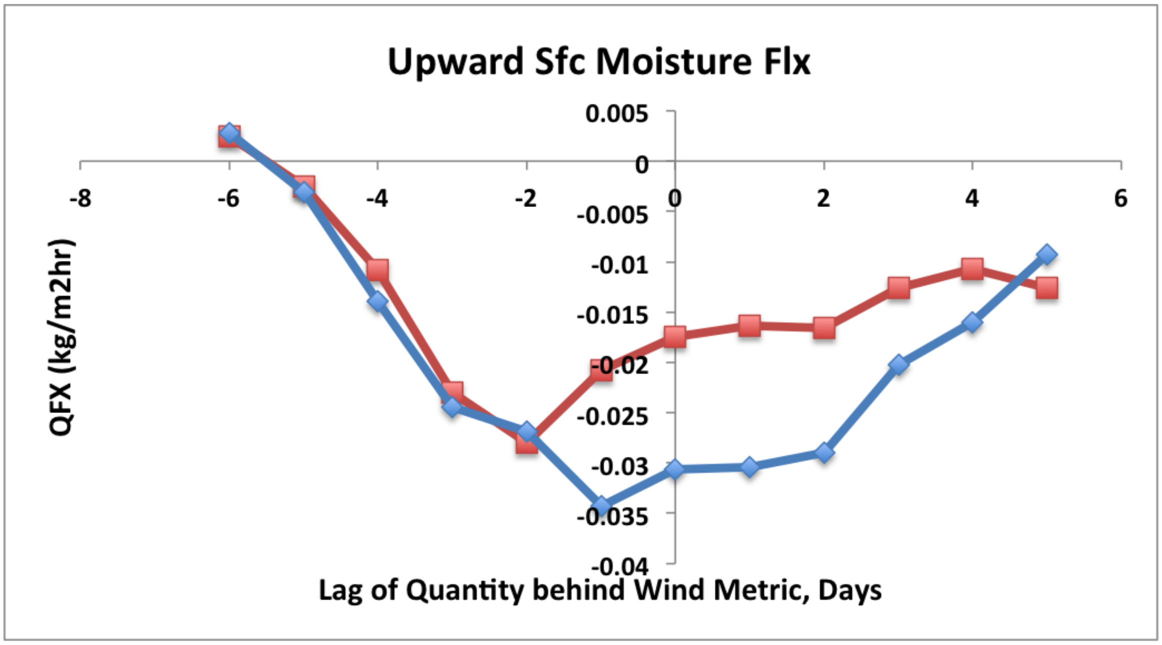

Figure 3.61: Upward surface moisture flux ($\frac{kg}{m^2 hr}$) for BBon and BBoff, averaged over subregion 2.5 ° S - 18.5 ° S, 8.5 ° E - 15.5 ° E. Lines represent the difference between composites on the upper 30% of the wind metric minus composites on the lower 30% of the wind metric for each simulation. Composite differences are plotted (left to right) at lag times -6 to +5 days.

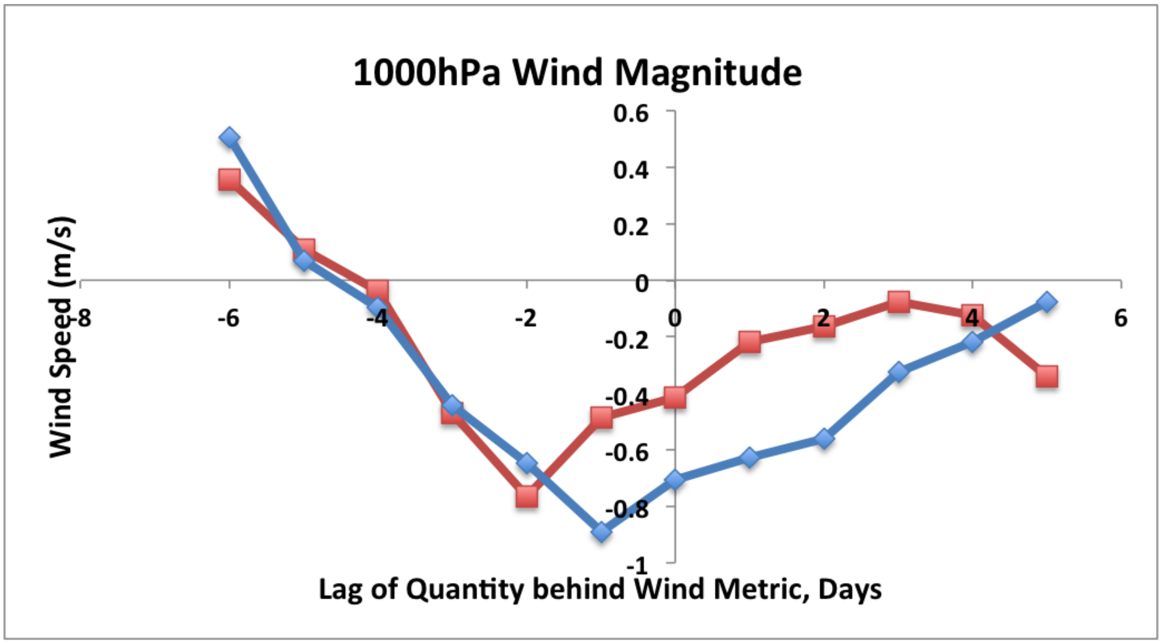

Figure 3.62: Surface wind speed (m/s) for BBon and BBoff, averaged over subregion 2.5 ° S - 18.5 ° S, 8.5 ° E - 15.5 ° E. Lines represent the difference between composites on the upper 30% of the wind metric minus composites on the lower 30% of the wind metric for each simulation. Composite differences are plotted (left to right) at lag times -6 to +5 days.

mean separation is positive for both the upper and lower 30% of the wind metric, it is 250 m greater during peak offshore flow. The result is that droplet concentration (fig. 3.55) is *less* sensitive to the aerosols transported offshore during strong easterly flow regimes for BBon. So while BBon has more aerosols, and higher droplet concentration overall, the influence of the meteorology is to insulate clouds from aerosols during easterly transport events.

# Chapter 4

# CONCLUSION

In this study, we sought to characterize the impact of (1) non-absorbing biomass burning aerosols and (2) meteorological variability on stratocumulus clouds off the Atlantic coast of sub-Saharan Africa. We compared mean values for simulations with and without biomass burning, but with the same meteorology, to quantify the mean impact of these aerosols. These results showed that non-absorbing biomass burning aerosols lead to smaller effective cloud droplet radii, fewer low clouds, reduced lower tropospheric stability, and enhanced liquid water path. The finding of smaller effective radii is consistent with Costantino and Breon ([21])s examination of co-located clouds and aerosols in the study region. The exclusion of absorbing aerosols seems to have flipped the response in low cloud fraction and LTS relative to Sakaeda et al ([85]). However, we were able to simulate the increase in LWP observed by Sakaeda et al ([85]) and Wilcox et al ([107], [108]) which those authors attributed to the presence of absorbing aerosols.

We were able to capture synoptic-scale variability of the subtropical high that dominates the region using a 4 km metric of offshore coastal wind flow. In lag-time space, this metric showed the offshore export of aerosols. By comparing variables lagged on this metric for simulations with and without biomass burning, we were able to quantify how this particular kind of meteorological variability influences clouds and aerosols. The meteorology-driven responses were typically similar with and without biomass burning, indicating that absent absorbing aerosols, the weather related variability is similar for both simulations and likely just as important as the aerosol-driven variability. This is consistent with Mauger and Norris ([72]), George et al. ([34]), and

Su et al. ([92]). The response to this synoptic meteorology cycle was often opposed to the mean aerosol-mediated response: during strong vs weak offshore flow, there were more low clouds, greater LTS, and lower liquid water path. The increase in LTS was related to offshore potential temperature advection and was consistent with the low cloud response. The decrease in LWP appears to be caused by diminished surface moisture flux. We are interested in how cloud properties respond to meteorology when absorbing aerosols are included, as they are in all previous studies. The impact of meteorology was to diminish effective radius, potentially enhancing the effect of aerosol loading.

For the first time, this study characterized aerosol-cloud layer separations in the context of synoptic-scale meteorological variability. During peak offshore flow, a reduction in free tropospheric subsidence enabled aerosol layers to remain lofted as they were exported offshore, so their base heights were typically higher. Meanwhile, stratocumulus clouds were lower, possibly due to reduced turbulent kinetic energy in the marine boundary layer. Together, this lead to increased separation between aerosol and cloud layers during peak offshore flow events, which would serve to insulate the stratocumulus clouds from aerosol microphysical interactions at the times of peak aerosol loading.

In the future, we intend to include absorbing aerosols in the model simulations and repeat the analysis to determine how absorption influences these results. In particular, we are interested in the liquid water path and the height of aerosol layers. Sakaeda et al ([85]) found much larger decreases in free tropospheric subsidence in a model that included absorbing aerosols; if we see the same result, will the aerosols be even further separated from the clouds? Together, the results excluding and including absorbing aerosols will paint a more complete picture of how aerosols, meteorology, and clouds interact in this region.

# BIBLIOGRAPHY

[1] Hayder Abdul-Razzak and Steven J. Ghan. A parameterization of aerosol activation: 2. Multiple aerosol types. *Journal of Geophysical Research*, 105(D5):6837, March 2000.

[2] A. S. Ackerman. Reduction of Tropical Cloudiness by Soot. *Science*, 288(5468):1042–1047, May 2000.

[3] Andrew S Ackerman, Michael P Kirkpatrick, David E Stevens, and Owen B Toon. The impact of humidity above stratiform clouds on indirect aerosol climate forcing. *Nature*, 432(7020):1014–7, December 2004.

[4] Ingmar J. Ackermann, Heinz Hass, M. Memmesheimer, A. Ebel, Francis S. Binkowski, and Uma Shankar. Modal aerosol dynamics model for Europe. *Atmospheric Environment*, 32(17):2981–2999, 1998.

[5] R. Ahmadov, S. A. McKeen, A. L. Robinson, R. Bahreini, A. M. Middlebrook, J. A. de Gouw, J. Meagher, E.-Y. Hsie, E. Edgerton, S. Shaw, and M. Trainer. A volatility basis set model for summertime secondary organic aerosols over the eastern united states in 2006. *Journal of Geophysical Research: Atmospheres*, 117(D6):n/a–n/a, 2012.

[6] S. K. Akagi, R. J. Yokelson, C. Wiedinmyer, M. J. Alvarado, J. S. Reid, T. Karl, J. D. Crounse, and P. O. Wennberg. Emission factors for open and domestic biomass burning for use in atmospheric models. *Atmospheric Chemistry and Physics*, 11(9):4039–4072, May 2011.

[7] B A Albrecht. Aerosols, cloud microphysics, and fractional cloudiness. *Science (New York, N.Y.)*, 245(4923):1227–30, September 1989.

[8] M. O. Andreae and P. Merlet. Emission of trace gases and aerosols from biomass burning. *Global Biogeochemical Cycles*, 15(4):955–966, 2001.

[9] Chi O. Ao, Duane E. Waliser, Steven K. Chan, Jui-Lin Li, Baijun Tian, Feiqin Xie, and Anthony J. Mannucci. Planetary boundary layer heights from GPS radio occultation refractivity and humidity profiles. *Journal of Geophysical Research*, 117(D16):D16117, August 2012.

[10] Craig F. Bohren. Multiple scattering of light and some of its observable consequences. *American Journal of Physics*, 55(6):524, June 1987.

[11] T. C. Bond, S. J. Doherty, D. W. Fahey, P. M. Forster, T. Berntsen, B. J. DeAngelo, M. G. Flanner, S. Ghan, B. Kärcher, D. Koch, S. Kinne, Y. Kondo, P. K. Quinn, M. C. Sarofim, M. G. Schultz, M. Schulz, C. Venkataraman, H. Zhang, S. Zhang, N. Bellouin, S. K. Guttikunda, P. K. Hopke, M. Z. Jacobson, J. W. Kaiser, Z. Klimont, U. Lohmann, J. P. Schwarz, D. Shindell, T. Storelvmo, S. G. Warren, and C. S. Zender. Bounding the role of black carbon in the climate system: A scientific assessment. *Journal of Geophysical Research: Atmospheres*, 118(11):5380–5552, June 2013.

[12] Tami C. Bond. A technology-based global inventory of black and organic carbon emissions from combustion. *Journal of Geophysical Research*, 109(D14):D14203, 2004.

[13] Francois-Marie Bréon, Didier Tanré, and Sylvia Generoso. Aerosol effect on cloud droplet size monitored from satellite. *Science (New York, N.Y.)*, 295(5556):834–8, February 2002.

[14] C. S. Bretherton, P. N. Blossey, and J. Uchida. Cloud droplet sedimentation, entrainment efficiency, and subtropical stratocumulus albedo. *Geophysical Research Letters*, 34(3):L03813, February 2007.

[15] Christopher S. Bretherton and Sungsu Park. A New Moist Turbulence Parameterization in the Community Atmosphere Model. *Journal of Climate*, 22(12):3422–3448, June 2009.

[16] D. Chand, R. Wood, T. L. Anderson, S. K. Satheesh, and R. J. Charlson. Satellite-derived direct radiative effect of aerosols dependent on cloud cover. *Nature Geoscience*, 2(3):181–184, February 2009.

[17] E. G. Chapman, W. I. Gustafson, R. C. Easter, J. C. Barnard, S. J. Ghan, M. S. Pekour, and J. D. Fast. Coupling aerosol-cloud-radiative processes in the WRF-Chem model: Investigating the radiative impact of elevated point sources. *Atmospheric Chemistry and Physics*, 9(3):945–964, February 2009.

[18] H. Chepfer, S. Bony, D. Winker, G. Cesana, J. L. Dufresne, P. Minnis, C. J. Stubenrauch, and S. Zeng. The GCM-Oriented CALIPSO Cloud Product (CALIPSO-GOCCP). *Journal of Geophysical Research*, 115:D00H16, March 2010.

[19] Matthew W. Christensen and Graeme L. Stephens. Microphysical and macrophysical responses of marine stratocumulus polluted by underlying ships: 2. impacts of haze on precipitating clouds. *Journal of Geophysical Research: Atmospheres*, 117(D11):n/a–n/a, 2012.

[20] P Chylek and J A Coakley. Aerosols and climate. *Science (New York, N.Y.)*, 183(4120):75–7, January 1974.

[21] L. Costantino and F.-M. Bréon. Aerosol indirect effect on warm clouds over South-East Atlantic, from co-located MODIS and CALIPSO observations. *Atmospheric Chemistry and Physics Discussions*, 12(6):14197–14246, June 2012.

[22] Lorenzo Costantino and François-Marie Bréon. Analysis of aerosol-cloud interaction from multi-sensor satellite observations. *Geophysical Research Letters*, 37(11):n/a–n/a, June 2010.

[23] M. B. Ek, K. E. Mitchell, Y. Lin, E. Rogers, P. Grunmann, V. Koren, G. Gayno, and J. D. Tarpley. Implementation of noah land surface model advances in the national centers for environmental prediction operational mesoscale eta model. *Journal of Geophysical Research: Atmospheres*, 108(D22):n/a–n/a, 2003.

[24] L. K. Emmons, S. Walters, P. G. Hess, J.-F. Lamarque, G. G. Pfister, D. Fillmore, C. Granier, A. Guenther, D. Kinnison, T. Laepple, J. Orlando, X. Tie, G. Tyndall, C. Wiedinmyer, S. L. Baughcum, and S. Kloster. Description and evaluation of the Model for Ozone and Related chemical Tracers, version 4 (MOZART-4). *Geoscientific Model Development*, 3(1):43–67, January 2010.

[25] Veronika Eyring, Ivar S.A. Isaksen, Terje Berntsen, William J. Collins, James J. Corbett, Oyvind Endresen, Roy G. Grainger, Jana Moldanova, Hans Schlager, and David S. Stevenson. Transport impacts on atmosphere and climate: Shipping. *Atmospheric Environment*, 44(37):4735–4771, 2010.

[26] Jerome D. Fast, William I. Gustafson, Richard C. Easter, Rahul A. Zaveri, James C. Barnard, Elaine G. Chapman, Georg A. Grell, and Steven E. Peckham. Evolution of ozone, particulates, and aerosol direct radiative forcing in the vicinity of Houston using a fully coupled meteorology-chemistry-aerosol model. *Journal of Geophysical Research*, 111(D21):D21305, November 2006.

[27] Graham Feingold. On smoke suppression of clouds in Amazonia. *Geophysical Research Letters*, 32(2):L02804, 2005.

[28] Ronald J Ferek, Timothy Garrett, Peter V Hobbs, Scott Strader, Doug Johnson, Jonathan P Taylor, Kurt Nielsen, Andrew S Ackerman, Yefim Kogan, Qingfu Liu, et al. Drizzle suppression in ship tracks. *Journal of the Atmospheric Sciences*, 57(16):2707–2728, 2000.

[29] P. Formenti, W. Elbert, W. Maenhaut, J. Haywood, S. Osborne, and M. O. Andreae. Inorganic and carbonaceous aerosols during the southern african regional science initiative (safari 2000) experiment: Chemical characteristics, physical properties, and emission data for smoke from african biomass burning. *Journal of Geophysical Research: Atmospheres*, 108(D13):n/a–n/a, 2003.

[30] S. R. Freitas, K. M. Longo, M. F. Alonso, M. Pirre, V. Marecal, G. Grell, R. Stockler, R. F. Mello, and M. Sánchez Gácita. PREP-CHEM-SRC 1.0: a preprocessor of trace gas and aerosol emission fields for regional and global atmospheric chemistry models. *Geoscientific Model Development*, 4(2):419–433, May 2011.

[31] S. R. Freitas, K. M. Longo, M. A. F. Silva Dias, R. Chatfield, P. Silva Dias, P. Artaxo, M. O. Andreae, G. Grell, L. F. Rodrigues, A. Fazenda, and J. Panetta. The Coupled Aerosol and Tracer Transport model to the Brazilian developments on the Regional Atmospheric Modeling System (CATT-BRAMS) Part 1: Model description and evaluation. *Atmospheric Chemistry and Physics*, 9(8):2843–2861, April 2009.

[32] M. Garstang, P. D. Tyson, R. Swap, M. Edwards, P. Kå llberg, and J. A. Lindesay. Horizontal and vertical transport of air over southern Africa. *Journal of Geophysical Research*, 101(D19):23721, October 1996.

[33] R. George. *Aerosol cloud interactions in the southeast Pacific: satellite observations, in situ data and regional modeling.* Doctoral, University of Washington, 2013.

[34] R. C. George and R. Wood. Subseasonal variability of low cloud radiative properties over the southeast Pacific Ocean. *Atmospheric Chemistry and Physics*, 10(8):4047–4063, April 2010.

[35] R. C. George, R. Wood, C. S. Bretherton, and G. Painter. Development and impact of hooks of large droplet concentration on remote southeast Pacific stratocumulus. *Atmospheric Chemistry and Physics Discussions*, 13(1):2493–2547, January 2013.

[36] Steven J. Ghan, Hayder Abdul-Razzak, Athanasios Nenes, Yi Ming, Xiaohong Liu, Mikhail Ovchinnikov, Ben Shipway, Nicholas Meskhidze, Jun Xu, and Xiangjun Shi. Droplet nucleation: Physically-based parameterizations and comparative evaluation. *Journal of Advances in Modeling Earth Systems*, 3(4):n/a–n/a, April 2011.

[37] Louis Giglio, Ivan Csiszar, and Christopher O. Justice. Global distribution and seasonality of active fires as observed with the Terra and Aqua Moderate Resolution Imaging Spectroradiometer (MODIS) sensors. *Journal of Geophysical Research*, 111(G2):G02016, 2006.

[38] S. L. Gong. A parameterization of sea-salt aerosol source function for sub- and super-micron particles. *Global Biogeochemical Cycles*, 17(4):n/a–n/a, December 2003.

[39] G. Grell, S. R. Freitas, M. Stuefer, and J. Fast. Inclusion of biomass burning in WRF-Chem: impact of wildfires on weather forecasts. *Atmospheric Chemistry and Physics Discussions*, 10(12):30613–30650, December 2010.

[40] Georg A. Grell, Steven E. Peckham, Rainer Schmitz, Stuart A. McKeen, Gregory Frost, William C. Skamarock, and Brian Eder. Fully coupled online chemistry within the WRF model. *Atmospheric Environment*, 39(37):6957–6975, 2005.

[41] A. Guenther, T. Karl, P. Harley, C. Wiedinmyer, P. I. Palmer, and C. Geron. Estimates of global terrestrial isoprene emissions using MEGAN (Model of Emissions of Gases and Aerosols from Nature). *Atmospheric Chemistry and Physics*, 6(11):3181–3210, August 2006.

[42] Alex Guenther, Patrick Zimmerman, and Mary Wildermuth. Natural volatile organic compound emission rate estimates for U.S. woodland landscapes. *Atmospheric Environment*, 28(6):1197–1210, 1994.

[43] William I. Gustafson, Elaine G. Chapman, Steven J. Ghan, Richard C. Easter, and Jerome D. Fast. Impact on modeled cloud characteristics due to simplified treatment of uniform cloud condensation nuclei during NEAQS 2004. *Geophysical Research Letters*, 34(19):L19809, October 2007.

[44] J. Hansen, M. Sato, and R. Ruedy. Radiative forcing and climate response. *Journal of Geophysical Research*, 102(D6):6831, March 1997.

[45] James Haywood and Olivier Boucher. Estimates of the direct and indirect radiative forcing due to tropospheric aerosols: A review. *Reviews of Geophysics*, 38(4):513–543, 2000.

[46] J. R. Herman, P. K. Bhartia, O. Torres, C. Hsu, C. Seftor, and E. Celarier. Global distribution of UV-absorbing aerosols from Nimbus 7/TOMS data. *Journal of Geophysical Research*, 102(D14):16911, July 1997.

[47] A. A. Hill and S. Dobbie. The impact of aerosols on non-precipitating marine stratocumulus. II: The semi-direct effect. *Quarterly Journal of the Royal Meteorological Society*, 134(634):1155–1165, July 2008.

[48] IPCC, IPCC 2007, and Terry Barker. Climate Change 2007 : An Assessment of the Intergovernmental Panel on Climate Change. Technical Report November, IPCC, 2007.

[49] Akinori Ito. Global estimates of biomass burning emissions based on satellite imagery for the year 2000. *Journal of Geophysical Research*, 109(D14):D14S05, 2004.

[50] FEI JIANG, QIAN LIU, XIAOXIAN HUANG, TIJIAN WANG, BINGLIANG ZHUANG, and MIN XIE. Regional modeling of secondary organic aerosol over china using wrf/chem. *Journal of aerosol science*, 43(1):57–73, 2012.

[51] Hongli Jiang, Huiwen Xue, Amit Teller, Graham Feingold, and Zev Levin. Aerosol effects on the lifetime of shallow cumulus. *Geophysical Research Letters*, 33(14):L14806, 2006.

[52] B. T. Johnson, K. P. Shine, and P. M. Forster. The semi-direct aerosol effect: Impact of absorbing aerosols on marine stratocumulus. *Quarterly Journal of the Royal Meteorological Society*, 130(599):1407–1422, April 2004.

[53] Christof Jost, Jrg Trentmann, Detlev Sprung, Meinrat O. Andreae, James B. McQuaid, and Hannah Barjat. Trace gas chemistry in a young biomass burning plume over namibia: Observations and model simulations. *Journal of Geophysical Research: Atmospheres*, 108(D13):n/a–n/a, 2003.

[54] C. Junker and C. Liousse. A global emission inventory of carbonaceous aerosol from historic records of fossil fuel and biofuel consumption for the period 18601997. *Atmospheric Chemistry and Physics*, 8(5):1195–1207, March 2008.

[55] Yoram J Kaufman, Ilan Koren, Lorraine A Remer, Daniel Rosenfeld, and Yinon Rudich. The effect of smoke, dust, and pollution aerosol on shallow cloud development over the Atlantic Ocean. *Proceedings of the National Academy of Sciences of the United States of America*, 102(32):11207–12, August 2005.

[56] Stephen A. Klein and Dennis L. Hartmann. The Seasonal Cycle of Low Stratiform Clouds. *Journal of Climate*, 6(8):1587–1606, August 1993.

[57] D. Koch and A. Del Genio. Black carbon absorption effects on cloud cover, review and synthesis. *Atmospheric Chemistry and Physics Discussions*, 10(3):7323–7346, March 2010.

[58] D. Koch and A. D. Del Genio. Black carbon semi-direct effects on cloud cover: review and synthesis. *Atmospheric Chemistry and Physics*, 10(16):7685–7696, August 2010.

[59] Ilan Koren, J Vanderlei Martins, Lorraine A Remer, and Hila Afargan. Smoke invigoration versus inhibition of clouds over the Amazon. *Science (New York, N.Y.)*, 321(5891):946–9, August 2008.

[60] H. Korhonen, K. S. Carslaw, and S. Romakkaniemi. Enhancement of marine cloud albedo via controlled sea spray injections: a global model study of the influence of emission rates, microphysics and transport. *Atmospheric Chemistry and Physics*, 10(9):4133–4143, May 2010.

[61] Markka Kulmala, Ari Laaksonen, and Liisa Pirjola. Parameterizations for sulfuric acid/water nucleation rates. *Journal of Geophysical Research*, 103(D7):8301, April 1998.

[62] J.-F. Lamarque, T. C. Bond, V. Eyring, C. Granier, A. Heil, Z. Klimont, D. Lee, C. Liousse, A. Mieville, B. Owen, M. G. Schultz, D. Shindell, S. J. Smith, E. Stehfest, J. Van Aardenne, O. R. Cooper, M. Kainuma, N. Mahowald, J. R. McConnell, V. Naik, K. Riahi, and D. P. van Vuuren. Historical (18502000) gridded anthropogenic and biomass burning emissions of reactive gases and aerosols: methodology and application. *Atmospheric Chemistry and Physics*, 10(15):7017–7039, August 2010.

[63] D. Latham. PLUMP: A one-dimensional plume predictor and cloud model for fire and smoke managers, General Technical Report INT-GTR-314. Technical report, Intermountain Research Station, USDA Forest Service, 1994.

[64] Lee, D. S., Owen, B., Graham, A., Fichter, C., Lim, L. L., and D. Dimitriu. Allocation of International Aviation Emissions from Scheduled Air Trafc: Present Day and Historical. Technical report, UK Department for Environment, Food and Rural Affairs, London, 2005.

[65] R.-R. Li, KaufmanY. J., W. M. Hao, J. M. Salmon, and B.-C. Gao. A technique for detecting burn scars using MODIS data. *IEEE Transactions on Geoscience and Remote Sensing*, 42(6):1300–1308, June 2004.

[66] Yuh-Lang Lin, Richard D. Farley, and Harold D. Orville. Bulk Parameterization of the Snow Field in a Cloud Model. *Journal of Climate and Applied Meteorology*, 22(6):1065–1092, June 1983.

[67] Yongqiang Liu, John Stanturf, and Scott Goodrick. Trends in global wildfire potential in a changing climate. *Forest Ecology and Management*, 259(4):685–697, 2010.

[68] Norman G. Loeb and Gregory L. Schuster. An observational study of the relationship between cloud, aerosol and meteorology in broken low-level cloud conditions. *Journal of Geophysical Research*, 113(D14):D14214, July 2008.

[69] K. M. Longo, S. R. Freitas, A. Setzer, E. Prins, P. Artaxo, and M. O. Andreae. The Coupled Aerosol and Tracer Transport model to the Brazilian developments on the Regional Atmospheric Modeling System (CATT-BRAMS) Part 2: Model sensitivity to the biomass burning inventories. *Atmospheric Chemistry and Physics Discussions*, 7(3):8571–8595, June 2007.

[70] J. R. Marlon, P. J. Bartlein, C. Carcaillet, D. G. Gavin, S. P. Harrison, P. E. Higuera, F. Joos, M. J. Power, and I. C. Prentice. Climate and human influences on globalbiomass burning over the past twomillennia. *Nature Geoscience*, 1(10):697–702, September 2008.

[71] G. M. Martin, D. W. Johnson, and A. Spice. The Measurement and Parameterization of Effective Radius of Droplets in Warm Stratocumulus Clouds. *Journal of the Atmospheric Sciences*, 51(13):1823–1842, July 1994.

[72] Guillaume S. Mauger and Joel R. Norris. Meteorological bias in satellite estimates of aerosol-cloud relationships. *Geophysical Research Letters*, 34(16):n/a–n/a, August 2007.

[73] Greg M. McFarquhar and Hailong Wang. Effects of aerosols on trade wind cumuli over the Indian Ocean: Model simulations. *Quarterly Journal of the Royal Meteorological Society*, 132(616):821–843, April 2006.

[74] Paulette Middleton, William R. Stockwell, and William P.L. Carter. Aggregation and analysis of volatile organic compound emissions for regional modeling. *Atmospheric Environment. Part A. General Topics*, 24(5):1107–1133, 1990.

[75] Florent Mouillot and Christopher B. Field. Fire history and the global carbon budget: a 1ox 1o fire history reconstruction for the 20th century. *Global Change Biology*, 11(3):398–420, March 2005.

[76] Ali H. Omar, David M. Winker, Mark A. Vaughan, Yongxiang Hu, Charles R. Trepte, Richard A. Ferrare, Kam-Pui Lee, Chris A. Hostetler, Chieko Kittaka, Raymond R. Rogers, Ralph E. Kuehn, and Zhaoyan Liu. The CALIPSO Automated Aerosol Classification and Lidar Ratio Selection Algorithm. *Journal of Atmospheric and Oceanic Technology*, 26(10):1994–2014, October 2009.

[77] O Pechony and D T Shindell. Driving forces of global wildfires over the past millennium and the forthcoming century. *Proceedings of the National Academy of Sciences of the United States of America*, 107(45):19167–70, November 2010.

[78] S. Platnick and S. Twomey. Determining the Susceptibility of Cloud Albedo to Changes in Droplet Concentration with the Advanced Very High Resolution Radiometer. *Journal of Applied Meteorology*, 33(3):334–347, March 1994.

[79] M. J. Power, J. Marlon, N. Ortiz, P. J. Bartlein, S. P. Harrison, F. E. Mayle, A. Ballouche, R. H. W. Bradshaw, C. Carcaillet, C. Cordova, S. Mooney, P. I. Moreno, I. C. Prentice, K. Thonicke, W. Tinner, C. Whitlock, Y. Zhang, Y. Zhao, A. A. Ali, R. S. Anderson, R. Beer, H. Behling, C. Briles, K. J. Brown, A. Brunelle, M. Bush, P. Camill, G. Q. Chu, J. Clark, D. Colombaroli, S. Connor, A.-L. Daniau, M. Daniels, J. Dodson, E. Doughty, M. E. Edwards, W. Finsinger, D. Foster, J. Frechette, M.-J. Gaillard, D. G. Gavin, E. Gobet, S. Haberle, D. J. Hallett, P. Higuera, G. Hope, S. Horn, J. Inoue, P. Kaltenrieder, L. Kennedy, Z. C. Kong, C. Larsen, C. J. Long, J. Lynch, E. A. Lynch, M. McGlone, S. Meeks, S. Mensing, G. Meyer, T. Minckley, J. Mohr, D. M. Nelson, J. New, R. Newnham, R. Noti, W. Oswald, J. Pierce, P. J. H. Richard, C. Rowe, M. F. Sanchez Goñi, B. N. Shuman, H. Takahara, J. Toney, C. Turney, D. H. Urrego-Sanchez, C. Umbanhowar, M. Vandergoes, B. Vanniere, E. Vescovi, M. Walsh, X. Wang, N. Williams, J. Wilmshurst, and J. H. Zhang. Changes in fire regimes since the Last Glacial Maximum: an assessment based on a global synthesis and analysis of charcoal data. *Climate Dynamics*, 30(7-8):887–907, December 2008.

[80] L F Radke, J A Coakley, and M D King. Direct and remote sensing observations

of the effects of ships on clouds. *Science (New York, N.Y.)*, 246(4934):1146–9, December 1989.

[81] D. A. Rahn and R. Garreaud. Marine boundary layer over the subtropical southeast pacific during vocals-rex part 2: Synoptic variability. *Atmospheric Chemistry and Physics*, 10(10):4507–4519, 2010.

[82] R. R. Rogers and M. K Yau. *A short course in cloud physics*. Butterworth-Heinemann, Woburn, MA, 3 edition, 1989.

[83] D.P. Roy, P.E. Lewis, and C.O. Justice. Burned area mapping using multi-temporal moderate spatial resolution dataa bi-directional reflectance model-based expectation approach. *Remote Sensing of Environment*, 83(1):263–286, 2002.

[84] P. E. Saide, S. N. Spak, G. R. Carmichael, M. A. Mena-Carrasco, Q. Yang, S. Howell, D. C. Leon, J. R. Snider, A. R. Bandy, J. L. Collett, K. B. Benedict, S. P. de Szoeke, L. N. Hawkins, G. Allen, I. Crawford, J. Crosier, and S. R. Springston. Evaluating WRF-Chem aerosol indirect effects in Southeast Pacific marine stratocumulus during VOCALS-REx. *Atmospheric Chemistry and Physics*, 12(6):3045–3064, March 2012.

[85] Naoko Sakaeda, Robert Wood, and Philip J. Rasch. Direct and semidirect aerosol effects of southern African biomass burning aerosol. *Journal of Geophysical Research*, 116(D12):D12205, June 2011.

[86] Benedikt Schell, Ingmar J. Ackermann, Heinz Hass, Francis S. Binkowski, and Adolf Ebel. Modeling the formation of secondary organic aerosol within a comprehensive air quality model system. *Journal of Geophysical Research: Atmospheres*, 106(D22):28275–28293, November 2001.

[87] Martin G. Schultz, Angelika Heil, Judith J. Hoelzemann, Allan Spessa, Kirsten Thonicke, Johann G. Goldammer, Alexander C. Held, Jose M. C. Pereira, and Maarten van het Bolscher. Global wildland fire emissions from 1960 to 2000. *Global Biogeochemical Cycles*, 22(2):n/a–n/a, June 2008.

[88] Ronald W. Shea, Barbara W. Shea, J. Boone Kauffman, Darold E. Ward, Craig I. Haskins, and Mary C. Scholes. Fuel biomass and combustion factors associated with fires in savanna ecosystems of South Africa and Zambia. *Journal of Geophysical Research*, 101(D19):23551, October 1996.

[89] M. Simon. Burnt area detection at global scale using ATSR-2: The GLOBSCAR products and their qualification. *Journal of Geophysical Research*, 109(D14):D14S02, 2004.

[90] S. J. Smith, J. van Aardenne, Z. Klimont, R. J. Andres, A. Volke, and S. Delgado Arias. Anthropogenic sulfur dioxide emissions: 18502005. *Atmospheric Chemistry and Physics*, 11(3):1101–1116, February 2011.

[91] William R. Stockwell, Paulette Middleton, Julius S. Chang, and Xiaoyan Tang. The second generation regional acid deposition model chemical mechanism for regional air quality modeling. *Journal of Geophysical Research*, 95(D10):16343, 1990.

[92] Wenying Su, Norman G. Loeb, Kuan-Man Xu, Gregory L. Schuster, and Zachary A. Eitzen. An estimate of aerosol indirect effect from satellite measurements with concurrent meteorological analysis. *Journal of Geophysical Research*, 115(D18):D18219, September 2010.

[93] R. Swap, M. Garstang, S. A. Macko, P. D. Tyson, W. Maenhaut, P. Artaxo, P. Kå llberg, and R. Talbot. The long-range transport of southern African aerosols to the tropical South Atlantic. *Journal of Geophysical Research*, 101(D19):23777, October 1996.

[94] C. R. Terai, R. Wood, D. C. Leon, and P. Zuidema. Does precipitation susceptibility vary with increasing cloud thickness in marine stratocumulus? *Atmospheric Chemistry and Physics*, 12(10):4567–4583, May 2012.

[95] The Mendeley Support Team. Getting Started with Mendeley, 2011.

[96] Anne M. Thompson. Lusaka, Zambia, during SAFARI-2000: Convergence of local and imported ozone pollution. *Geophysical Research Letters*, 29(20):1976, 2002.

[97] O. Torres, P. K. Bhartia, J. R. Herman, Z. Ahmad, and J. Gleason. Derivation of aerosol properties from satellite measurements of backscattered ultraviolet radiation: Theoretical basis. *Journal of Geophysical Research*, 103(D14):17099, July 1998.

[98] Omar Torres, Aapo Tanskanen, Ben Veihelmann, Changwoo Ahn, Remco Braak, Pawan K. Bhartia, Pepijn Veefkind, and Pieternel Levelt. Aerosols and surface UV products from Ozone Monitoring Instrument observations: An overview. *Journal of Geophysical Research*, 112(D24):D24S47, December 2007.

[99] P. D. Tyson, M. Garstang, R. J. Swap, E. V. Browell, R. D. Diab, and A. M Thompson. Transport and vertical structure of ozone and aerosol distributions over southern Africa. In J.S. Levine, editor, *Biomass Burning and Global Change*, pages 403–421. MIT Press, Cambridge, MA, 1996.

[100] P.D Tyson and P.C DAbreton. Transport and recirculation of aerosols off Southern Africamacroscale plume structure. *Atmospheric Environment*, 32(9):1511–1524, 1998.

[101] Minghuai Wang, Steven Ghan, Xiaohong Liu, Tristan S. L'Ecuyer, Kai Zhang, Hugh Morrison, Mikhail Ovchinnikov, Richard Easter, Roger Marchand, Duli Chand, Yun Qian, and Joyce E. Penner. Constraining cloud lifetime effects of aerosols using A-Train satellite observations. *Geophysical Research Letters*, 39(15):n/a–n/a, August 2012.

[102] G. Wen, A. Marshak, and R.F. Cahalan. Impact of 3-D Clouds on Clear-Sky Reflectance and Aerosol Retrieval in a Biomass Burning Region of Brazil. *IEEE Geoscience and Remote Sensing Letters*, 3(1):169–172, January 2006.

[103] Guoyong Wen, Alexander Marshak, Robert F. Cahalan, Lorraine A. Remer, and Richard G. Kleidman. 3-D aerosol-cloud radiative interaction observed in collocated MODIS and ASTER images of cumulus cloud fields. *Journal of Geophysical Research*, 112(D13):D13204, July 2007.

[104] Frank J. Wentz. A well-calibrated ocean algorithm for special sensor microwave / imager. *Journal of Geophysical Research*, 102(C4):8703, 1997.

[105] Frank J. Wentz and Roy W. Spencer. SSM/I Rain Retrievals within a Unified All-Weather Ocean Algorithm. *Journal of the Atmospheric Sciences*, 55(9):1613–1627, May 1998.

[106] C. Wiedinmyer, S. K. Akagi, R. J. Yokelson, L. K. Emmons, J. A. Al-Saadi, J. J. Orlando, and A. J. Soja. The Fire INventory from NCAR (FINN): a high resolution global model to estimate the emissions from open burning. *Geoscientific Model Development*, 4(3):625–641, July 2011.

[107] E. M. Wilcox. Stratocumulus cloud thickening beneath layers of absorbing smoke aerosol. *Atmospheric Chemistry and Physics*, 10(23):11769–11777, December 2010.

[108] E. M. Wilcox. Direct and semi-direct radiative forcing of smoke aerosols over clouds. *Atmospheric Chemistry and Physics*, 12(1):139–149, January 2012.

[109] David M. Winker, Mark A. Vaughan, Ali Omar, Yongxiang Hu, Kathleen A. Powell, Zhaoyan Liu, William H. Hunt, and Stuart A. Young. Overview of the CALIPSO Mission and CALIOP Data Processing Algorithms. *Journal of Atmospheric and Oceanic Technology*, 26(11):2310–2323, November 2009.

[110] Robert Wood. Cancellation of Aerosol Indirect Effects in Marine Stratocumulus through Cloud Thinning. *Journal of the Atmospheric Sciences*, 64(7):2657–2669, July 2007.

[111] Robert Wood. Stratocumulus Clouds. *Monthly Weather Review*, 140(8):2373–2423, August 2012.

[112] M. C. Wyant, R. Wood, C. S. Bretherton, C. R. Mechoso, J. Bacmeister, M. A. Balmaseda, B. Barrett, F. Codron, P. Earnshaw, J. Fast, C. Hannay, J. W. Kaiser, H. Kitagawa, S. A. Klein, M. Köhler, J. Manganello, H.-L. Pan, F. Sun, S. Wang, and Y. Wang. The PreVOCA experiment: modeling the lower troposphere in the Southeast Pacific. *Atmospheric Chemistry and Physics*, 10(10):4757–4774, May 2010.

[113] Paquita Zuidema, David Painemal, Simon de Szoeke, and Chris Fairall. Stratocumulus Cloud-Top Height Estimates and Their Climatic Implications. *Journal of Climate*, 22:4652–4666, February 2010.